Elastic Full-Waveform Inversion in the Presence of Fracture-Induced Anisotropy

Jonas Holm Erstad

Thesis for the degree
Master of Science in Geophysics

Department of Earth Science

University of Bergen

June 7, 2020

Abstract

Seismic imaging of the subsurface is essential in both the exploration and production of hydrocarbon reservoirs. Seismic full-waveform modelling and inversion methods can be used to obtain high-resolution images of the elastic properties. This work aims to develop further methods for non-linear elastic waveform inversion in anisotropic media associated with fractures. Based on previous research, the goal is to investigate which approach is the most reliable at estimating stiffness parameters.

In this context, the rock physics t-matrix method was used to represent the stiffness perturbation due to fractures in a complex porous medium. The elastodynamic wave equation was solved using the full integral-equation solution of the Lippmann-Schwinger type. The frequency-domain scattered wavefield was used as synthetic data, to simulate the particle displacement from a fracture-induced anisotropic medium. Elastic Full-Waveform Inversion (FWI) makes use of all the information in the wavefield and is implemented by using the distorted Born iterative method (DBI). The DBI method is consistent with the Gauss-Newton iterative method and was performed using the self-adaptive regularisation scheme. For each iteration, both the Green's function and the sensitivity matrix were updated for the actual medium. Two models with different geological features, i.e. the syncline and anticline model, were used in the synthetic numerical experiments to simulate a fractured reservoir with transversely isotropic symmetry. Different levels of noise, as well as source-configurations, were investigated.

For the models considered in this work, fracture-based inversion results were shown to match the actual model better than the stiffness-based inversion. When evaluating the results for noisy data of 40 dB SNR, it is evident that the stiffness-inversion is insufficient, particularly for the C_{13} parameter, when compared to fracture-inversion. On this basis, inverting for fracture parameters is recommended when characterising a reservoir associated with fractures. Future research is needed to identify more desirable fracture models and more efficient calculation of the full integral-equation solution.

Acknowledgement

My Master's thesis was conducted at the Department of Earth Science at the University of Bergen. I am pleased with the result after two years of preparation, research, and hard work.

I want to express my sincere gratitude and appreciation to my supervisor Prof. Morten Jakobsen. Without his guidance, this project would not have materialised. Thank you for all the meaningful discussions about scattering theory and integral-equation methods. I have greatly benefited from your Matlab code, allowing me to extend it further. Also, I considerably appreciate the feedback and technical advice from my co-supervisor, Assoc. Prof. Einar Iversen.

I am grateful to the MSc student, Mahmoud ElTayieb, for the many engaging discussions throughout the development of this thesis. I want to thank my fellow students at the faculty for all the great times. Additionally, a big thanks to my friends Mr. Hallvard Vasstveit and Mr. Steinar Halsne, for agreeing to proofread this thesis.

Finally, I am deeply grateful to my parents and to my fiancée for providing me with support and encouragement throughout my years of study. This accomplishment would not have been possible without them.

Bergen, June 2020

Jonas Holm Erstad

Contents

1 Introduction **1**
- 1.1 Background . . . 1
- 1.2 Elastic Full-Waveform Inversion . . . 2
- 1.3 Objectives, Scope of Work, and Outline . . . 4
  - 1.3.1 Thesis Objectives . . . 4
  - 1.3.2 Limitations on Scope of Work . . . 4
  - 1.3.3 Outline of Thesis . . . 5

2 Effective Elastic Properties of Fracture-Induced Anisotropy **7**
- 2.1 Mechanical Behaviour of Rocks . . . 7
- 2.2 Seismic Anisotropy . . . 9
- 2.3 Effective Medium Theory for Fractured Rocks . . . 11
  - 2.3.1 Fractured Porous Media . . . 11
  - 2.3.2 Fracture Models . . . 12
  - 2.3.3 t-matrix for a Single Inclusion . . . 13
  - 2.3.4 Effects of Fluid Saturation . . . 16
  - 2.3.5 Relationship Between Stiffness and Fracture Density . . . 17
- 2.4 Numerical Results and Discussion . . . 19
  - 2.4.1 Syncline Model . . . 21
  - 2.4.2 Anticline Model . . . 24

3 Seismic Waveform Modelling **27**
- 3.1 Introduction . . . 27
- 3.2 Integral Equation Approach . . . 29
- 3.3 Exact Solution . . . 34
  - 3.3.1 Abbreviated Subscript Notation . . . 34
  - 3.3.2 Discretisation and Implementation . . . 34
- 3.4 Numerical Results and Discussion . . . 37
  - 3.4.1 Syncline Model . . . 40

3.4.2 Anticline Model . . . 43

4 Seismic Waveform Inversion 47
4.1 General Inversion Theory . . . 47
4.1.1 Linear Inversion Theory . . . 47
4.1.2 Non-Linear Inversion Theory . . . 49
4.2 Non-linear Inverse Scattering Problem . . . 50
4.2.1 Distorted Born Iterative Inversion Method . . . 50
4.2.2 Inversion Implementation . . . 51
4.2.3 Regularised Least-Squares Solution . . . 55
4.2.4 Regularisation Parameter . . . 57
4.3 Numerical Results and Discussion . . . 60
4.3.1 Syncline Model . . . 61
4.3.2 Anticline Model . . . 67

5 Waveform Inversion for Fracture Parameters 73
5.1 Introduction . . . 73
5.2 DBI Inversion for Fracture Density . . . 74
5.3 Numerical Results and Discussion . . . 76
5.3.1 Syncline Model . . . 77
5.3.2 Anticline Model . . . 83
5.4 Concluding Remarks . . . 89

6 Discussion and Conclusion 91
6.1 Discussion . . . 91
6.2 Conclusion . . . 93
6.3 Future Work . . . 94

Appendices 96
A Rock Physics G-tensor . . . 97
B Reference Green's Function and Derivatives . . . 99
B.1 Leading-term Green's Function . . . 99
B.2 First-Order Spatial Derivatives of Green's Function . . . 100
B.3 Second-Order Spatial Derivatives of Green's Function . . . 102

List of Figures

1.1 First- and second-order scattering illustration. An explosive source (red star) transmits seismic energy in all directions. Two arbitrary scattering points (black rectangles) in the scattering domain (grey box), act as sources and spread the energy towards the receiver (blue triangle). Ray paths (line with arrow) show the straight path of the seismic wavefront. 2

2.1 Illustrations of VTI and HTI media from Ikelle and Amundsen (2005, p. 531 and 535). A VTI medium (left) has a vertical symmetry axis, while a HTI medium has a horizontal symmetry axis. 10
2.2 Fracture-illustrations. Left: inclusion with a major axis a and a minor axis c. Right: physically reasonable horizontal fractures with a low aspect ratio. Inspired by Shahraini et al. (2011). 12
2.3 Effective stiffness values of dry (black), water-filled (blue) and gas-filled (red) fractures. Stiffness values were calculated based on the first-order correction for fractures, and the six coefficients correspond to a 3D VTI medium. 20
2.4 Effective stiffness coefficients of the first-order correction (solid) and second-order correction (dashed), for a 3D VTI medium. 20
2.5 Fracture density in the syncline model. 23
2.6 Effective elastic stiffness parameters of the 2D VTI syncline model. The colour map is the same for all parameters. 23
2.7 Fracture density of the anticline model. 26
2.8 Effective elastic stiffness parameters of the 2D VTI anticline model. The colour map is the same for all parameters. 26

3.1 Illustration of an actual medium with an area of perturbation in dark grey (3.1a) and two different reference media (3.1b, 3.1c). The Green's function of the reference medium can either be calculated for a homogeneous medium (middle), or a heterogeneous medium (right). The symbols at the top are: source (red $\star$) and receiver (blue $\bigtriangledown$). 31

3.2 Ricker wavelet with a central frequency of 7.5 Hz. Amplitude of the wavelet in the time-domain (upper), and magnitude (amplitude-spectrum) of the frequency-domain wavelet (lower). 38

3.3 Configuration of sources (red stars) and receivers (blue triangles) for the syncline model. The distance between both sources and receivers is 24 m. . 41

3.4 Normalised stiffness perturbation in each of the elastic parameters of a 2D VTI medium, for the syncline model. The colour map is the same for all parameters. 41

3.5 Real part of the synthetic (normalised) waveform data, corresponding to the true syncline model. The data vector is separated into the horizontal (upper), d_x, and vertical (lower), d_z, components of the particle displacement. 42

3.6 Imaginary part of the synthetic (normalised) waveform data, corresponding to the true syncline model. The data vector is separated into the horizontal (upper), d_x, and vertical (lower), d_z, components of the particle displacement. 42

3.7 Configuration of sources (red stars) and receivers (blue triangles) for the anticline model. The distance between each receiver is 24 m, while for each source the distance is 96 m. 44

3.8 Normalised stiffness perturbation in each of the elastic parameters of a 2D VTI medium, for the anticline model. The colour map is the same for all parameters. 44

3.9 Real part of the synthetic (normalised) waveform data, corresponding to the true anticline model. The data vector is separated into the horizontal (upper), d_x, and vertical (lower), d_z, components of the particle displacement. 45

3.10 Imaginary part of the synthetic (normalised) waveform data, corresponding to the true anticline model. The data vector is separated into the horizontal (upper), d_x, and vertical (lower), d_z, components of the particle displacement. 45

4.1 DBI inversion results for normalised stiffness perturbation in the syncline model. The data used was noiseless, and the colour map is the same for all parameters. 63

4.2 Absolute error of the inverted normalised stiffness perturbation in the syncline model, for the noiseless data. The colour map for absolute error is the same for all parameters. 63

4.3 Performance of the DBI inversion for stiffness perturbation in the syncline model, for the noiseless data. Model error (ϵ_m) and residual data error (ϵ_d) depend on the iteration number. The equations for data and model error are given in Eqs. (4.35) and (4.36). The data error converges to the noise-level (red dashed line). The last two plots show the regularisation parameter (λ) and the frequency (f), respectively. 64

4.4 Model vector of the DBI inversion result for stiffness perturbation in the syncline model, for the noiseless data. The starting model is shown as a blue line, the true model as a black line, and the inversion results as a red line. 64

4.5 DBI inversion result for the normalised stiffness perturbation in the syncline model, for the noisy data with an SNR of 40 dB. The colour map is the same for all parameters. 65

4.6 Absolute error of the inverted normalised stiffness perturbation in the syncline model, for the noisy data of 40 dB SNR. The colour map for absolute error is the same for all parameters. 65

4.7 Performance of the DBI inversion for stiffness perturbation in the syncline model, for noisy data of 40 dB SNR. Model error (ϵ_m) and residual data error (ϵ_d) depend on the iteration number. The data error converges to the noise-level (red dashed line). The last two plots show the regularisation parameter (λ) and the frequency (f), respectively. 66

4.8 Model vector of the DBI inversion result for the stiffness perturbation in the syncline model, for noisy data of 40 dB SNR. The starting model is shown as a blue line, the true model as a black line, and the inversion results as a red line. 66

4.9 DBI inversion result for the normalised stiffness perturbation in the anticline model, for the noiseless data. The colour map is the same for all parameters. 69

4.10 Absolute error of the inverted normalised stiffness perturbation in the anticline model, for the noiseless data. The colour map for absolute error is the same for all parameters. 69

4.11 Performance of the DBI inversion for stiffness perturbation in the anticline model, for the noiseless data. Model error (ϵ_m) and residual data error (ϵ_d) depend on the iteration number. The equations for data and model error are given in Eqs. (4.35) and (4.36). The data error converges to the noise-level (red dashed line). The last two plots show regularisation parameter (λ) and frequency (f), respectively. 70

4.12 Model parameters of the DBI inversion result for the normalised stiffness perturbation in the anticline model, for the noiseless data. The starting model is shown as a blue line, the true model as a black line, and the inversion results as a red line. 70

4.13 DBI inversion result for the normalised stiffness perturbation in the anticline model, for the noisy data with an SNR of 40 dB. The colour map is the same for all parameters. 71

4.14 Absolute error of the inverted normalised stiffness perturbation in the anticline model, for the noisy data of 40 dB SNR. The colour map for absolute error is the same for all parameters. 71

4.15 Performance of the DBI inversion for stiffness perturbation in the anticline model, for data with noise of 40 dB SNR. Model error (ϵ_m) and residual data error (ϵ_d) depend on the iteration number. The data error converges to the noise-level (red dashed line). The last two plots show regularisation parameter (λ) and frequency (f), respectively. 72

4.16 Model parameters of the DBI inversion result for the stiffness perturbation in the anticline model, for data with noise of 40 dB SNR. The starting model is shown as a blue line, the true model as a black line, and the inversion results as a red line. 72

5.1 DBI inversion result for the syncline model, for the noiseless data. 79

5.2 The corresponding normalised stiffness perturbations of the syncline model, for the noiseless data. The colour map is the same for all parameters. . . . 79

5.3 Performance of the DBI inversion for stiffness perturbation in the syncline model, for the noiseless data. Model error (ϵ_m) and residual data error (ϵ_d) depend on the iteration number. The equations for data and model error are given in Eqs. (4.35) and (4.36). The data error converges to the noise-level (red dashed line). The last two plots show regularisation parameter (λ) and frequency (f), respectively. 80

5.4 Model parameters of the DBI inversion result for the normalised stiffness perturbation in the syncline model, for the noiseless data. The starting model is shown as a blue line, the true model as a black line, and the inversion results as a red line. 80

5.5 DBI inversion result for the syncline model, with inverted fractured density (left) and absolute error (right). The data is noisy with an SNR of 40dB. . 81

5.6 The corresponding normalised stiffness perturbations of the syncline model, for the noisy data with an SNR of 40 dB. The colour map is the same for all parameters. 81

5.7 Performance of the DBI inversion for stiffness perturbation in the syncline model, for the noisy data with an SNR of 40 dB. Model error (ϵ_m) and residual data error (ϵ_d) depend on the iteration number. The data error converges to the noise-level (red dashed line). The last two plots show regularisation parameter (λ) and frequency (f), respectively. 82

5.8 Model parameters of the DBI inversion result for the normalised stiffness perturbation in the syncline model, for the noisy data with an SNR of 40 dB. The starting model is shown as a blue line, the true model as a black line, and the inversion results as a red line. 82

5.9 DBI inversion result for the anticline model, with inverted fractured density (left) and absolute error (right). The data is noiseless. 85

5.10 The corresponding normalised stiffness perturbations of the anticline model, for the noiseless data. The colour map is the same for all parameters. . . . 85

5.11 Performance of the DBI inversion for stiffness perturbation in the anticline model, for the noiseless data. Model error (ϵ_m) and residual data error (ϵ_d) depend on the iteration number. The equations for data and model error are given in Eqs. (4.35) and (4.36). The data error converges to the noise-level (red dashed line). The last two plots show regularisation parameter (λ) and frequency (f), respectively. 86

5.12 Model parameters of the DBI inversion result for the normalised stiffness perturbation in the anticline model, for the noiseless data. The starting model is shown as a blue line, the true model as a black line, and the inversion results as a red line. 86

5.13 DBI inversion result for the anticline model, with inverted fractured density (left) and absolute error (right). The data is noisy with an SNR 40 dB. . . 87

5.14 The corresponding normalised stiffness perturbations of the anticline model, for the noisy data with an SNR of 40 dB. The colour map is the same for all parameters. 87

5.15 Performance of the DBI inversion for stiffness perturbation in the anticline model, for the noisy data of 40 dB SNR. Model error (ϵ_m) and residual data error (ϵ_d) depend on the iteration number. The data error converges to the noise-level (red dashed line). The last two plots show regularisation parameter (λ) and frequency (f), respectively. 88

5.16 Model parameters of the DBI inversion result for the normalised stiffness perturbation in the anticline model, for the noisy data of 40 dB SNR. The starting model is shown as a blue line, the true model as a black line, and the inversion results as a red line. 88

List of Tables

2.1 Abbreviated subscript notation compared to spatial coordinates and general coordinate notation. 8

2.2 Effective stiffness coefficients, C^*_{IJ} [GPa], in the syncline model corresponding to the different fracture densities, ϵ [unit]. 21

2.3 Effective stiffness coefficients, C^*_{IJ} [GPa], in the anticline model corresponding to the different fracture densities, ϵ [unit]. 24

4.1 Comparison of the final model error ϵ_m [unit], and computation time τ_{CPU} [min], for the DBI stiffness-inversion results. For the noiseless results (5000 dB SNR), the tolerance was 10^{-5}, while for the noisy results (40 dB SNR) it was 10^{-2}. 60

5.1 Comparison of the final model error ϵ_m [unit], and computation time τ_{CPU} [min], for the DBI fracture-inversion results. For the noiseless results (5000 dB SNR), the tolerance was 10^{-5}, while for the noisy results (40 dB SNR) it was 10^{-2}. 76

List of Abbreviations

FD	Finite Difference
FWI	Full-Waveform Inversion
AVOA	Amplitude Versus Offset and Azimuth
DBIT	Distorted Born iterative T-matrix
DBI	Distorted Born iterative
2D	Two-dimensional
3D	Three-dimensional
VTI	Vertically Transverse Isotropic
HTI	Horizontally Transverse Isotropic
SNR	Signal-to-Noise Ratio
LS	Lippmann-Schwinger
FFT	Fast Fourier Transform

List of Symbols

$\boldsymbol{\sigma}$	Stress tensor
$\mathbf{C}$	Elasticity stiffness tensor
$\boldsymbol{\varepsilon}$	Strain tensor
$\mathbf{S}$	Compliance tensor
ϕ	Porosity
α_c	Fracture aspect ratio
ϵ	Fracture density
ξ	Number of fractures per unit volume
$\mathbf{t}$	T-matrix for single inclusion
$\mathbf{G}$	Second-rank Green's tensor
α	P-wave velocity
β	S-wave velocity
ρ	Mass density
$\mathbf{u}$	Particle displacement
ω	Angular frequency
$\mathbf{f}$	Source term
Ω	Scattering domain (volume)
δ_{ij}	Kronecker delta
δv	Grid block volume
$\mathbf{M}$	Third-rank Green's tensor
$\mathbf{\Gamma}$	Fourth-rank Green's tensor
$\mathbf{J}$	Sensitivity matrix
$\mathbf{m}$	Model vector
$\mathbf{d}$	Data vector
$\mathbf{H}$	Hessian matrix
$\dagger$	Hermitian transpose
λ	Regularization parameter
$\Re$	Real values

Chapter 1

Introduction

1.1 Background

The ultimate goal of modern petroleum seismology is to help discover new petroleum reservoirs and to enhance production from existing ones, through imaging of these reservoirs (Ikelle and Amundsen, 2005). Typically, reservoirs are assumed to be isotropic, but more realistically, these media tend to be anisotropic or transverse isotropic (Lee et al., 2010). Seismic anisotropy is an attractive topic and should ideally be accounted for in heterogeneous media (Jakobsen et al., 2020b). Azimuthal anisotropy in the subsurface may be a result of oriented fractures or stress fields (Ikelle and Amundsen, 2005).

A substantial proportion of the World's remaining hydrocarbon reserves are associated with naturally fractured rocks in carbonate and tight-sandstone reservoirs (Ali and Jakobsen, 2011a). Inversion for fracture parameters has emerged as a hot topic in recent years, as fractures have a significant impact on seismic waves (Jakobsen et al., 2003a; Pilskog et al., 2015) and fluid flow (Sævik et al., 2013). Fractures can lead to optimised production and are also relevant for CO2 sequestration and geothermal energy (Batzle and Simmons, 1976; Ali and Jakobsen, 2011b).

Estimation of physical properties of fractures at reservoir scale, from surface data, is useful in reservoir characterisation (Zhang et al., 2017). Conventionally, P-wave Amplitude Versus Offset and Azimuth (AVOA) has been used to characterise the subsurface fractures (Pilskog et al., 2015). The central assumption of AVOA analysis is that the reflector is laterally invariant (Bansal and Sen, 2010). Performing Full-Waveform Inversion (FWI) may solve this problem, as it makes use of all the information in the wavefield.

1.2 Elastic Full-Waveform Inversion

Elastic waves are mechanical vibrations that can propagate in both solid and fluid media (Royer and Dieulesaint, 1999). Changes in the elastic properties of the Earth lead to scattering of seismic energy (Gibson and Ben-Menahem, 1991). A scattered wavefield is the difference between the total and reference wavefield. Elastodynamic wave scattering is based on the general principles of scattering theory and continuum mechanics of elastic media (Snieder, 2002). The fundamental solution of the elastodynamic equation is the Green's function for a point source (Madariaga, 2007). Using the elastodynamic wave equation to account for shear waves is critical to characterise reservoirs (Jakobsen et al., 2020b).

The non-linear inverse scattering problem can be expressed as both the non-linear relationship between the physical properties, and the inclusion of multiples and reflections that multiply reflected events (Weglein et al., 2003). The seismic FWI can be viewed as a seismic inverse scattering problem (Huang et al., 2020b). Similar problems have been examined in other fields, such as electromagnetics, acoustics, and quantum mechanics (Jakobsen and Wu, 2018). An illustration of scattering is presented in Fig. 1.1, showing first- and second-order scattering between a source and receiver.

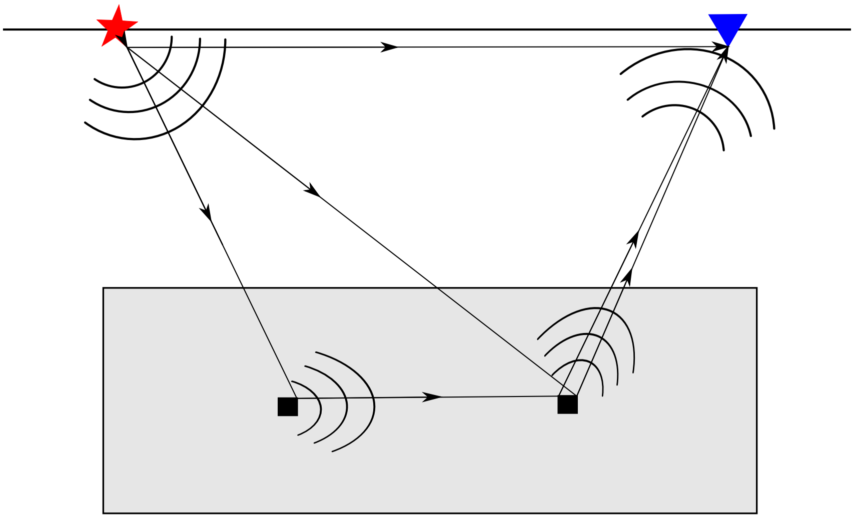

Figure 1.1: First- and second-order scattering illustration. An explosive source (red star) transmits seismic energy in all directions. Two arbitrary scattering points (black rectangles) in the scattering domain (grey box), act as sources and spread the energy towards the receiver (blue triangle). Ray paths (line with arrow) show the straight path of the seismic wavefront.

Seismic FWI promises sharp and high-resolution images compared to those in conventional migration velocity analysis and travel time tomography (Jakobsen et al., 2020b). The two main methods for the inversion process are gradient-based methods (e.g. steepest descent) and Newton-based methods (Abubakar et al., 2011). In the Gauss-Newton approach, a Newton-based method, the data-misfit, and sensitivity matrix are computed for each iteration (Jakobsen and Wu, 2018).

The main challenge in FWI is the high computational cost. The sensitivity of the results to the starting model is also a problem, but can be reduced by the use of multi-scale regularisation methods (Virieux and Operto, 2009; Jakobsen et al., 2020b). Waveform inversion is also not suitable for real data as it requires low frequencies (Alkhalifah and Choi, 2012). Additional concerns include having a suitable background medium and achieving adequate subsurface illumination (Zhang et al., 2017). Using more sources in the experiments, can combat the latter issue.

There are many methods for seismic FWI, which can be implemented both in the time-domain and frequency-domain. The Finite-element or the Finite Difference (FD) method for the full wave-equation can be used (Pratt, 1999; Virieux and Operto, 2009). Using the Born approximation and asymptotic ray theory to compute Green's function, is another method, called ray-Born inversion (Bansal and Sen, 2010). An FWI scheme based on the ray-Born approximation has been employed for fractures in geologically complex areas (Pilskog et al., 2015). The distorted Born iterative T-matrix (DBIT) method reduces the problem to a series of linear inverse problems, using an iterative T-matrix method for the dynamic background medium (Jakobsen and Ursin, 2015; Jakobsen and Wu, 2018; Jakobsen et al., 2020b). The problem can also be solved without the T-matrix, using only the distorted Born iterative method (DBI), which is employed in this work. Ideally, the goal is to use the method that gives the sharpest image with the highest resolution.

The numerical frequency-domain implementation of these methods have significant advantages compared to the time-domain implementation (Pratt, 1999). Accurate inversion results can often be obtained using a relatively low number of frequency components, decreasing the computational cost (Jakobsen and Ursin, 2015).

Ultimately, the purpose of FWI in fracture-induced anisotropic media, is to reconstruct the multiple parameters from the computed wavefield (Jakobsen et al., 2020b). There are a couple of concerns related to multi-parameter FWI, as the inversion is non-unique (Kamath and Tsvankin, 2014) and there are cross-talk effects (Jakobsen et al., 2017). Inverting for fracture densities simplifies this problem, as the inversion is for only one parameter (Pilskog et al., 2015). Fracture-based inversion is, however, very reliant on a good representation for the fracture model and rock physics parameters.

1.3 Objectives, Scope of Work, and Outline

1.3.1 Thesis Objectives

The main objective in this work is to develop methods for non-linear elastic waveform inversion in the presence of fracture-induced anisotropy. This objective involves solving the elastodynamic wave equation by using the integral-equation approach, and also to employ the DBI method to both stiffness perturbation and fracture density inversion.

A set of secondary goals include:

- Comparing results of elastic stiffness inversion with fracture density inversion, using the same DBI inversion method.
- Calculating frequency-domain data by using the full integral-equation solution.
- Investigating how the DBI inversion, for both stiffness perturbation and fracture density, are affected by random noise and complex features.
- Reviewing the theoretical background of elastic waveform inversion and inversion for fracture parameters.
- Estimating the effects of fluid-filled fractures on the elastic stiffness parameters.

1.3.2 Limitations on Scope of Work

To be able to achieve the main goals of this thesis within the permitted time, the following restraints on the scope of work are made:

- Fractures are assumed not to affect mass density, as flat fractures have a tiny volume (Jakobsen and Pilskog, 2016; Jakobsen et al., 2017). Therefore, mass density is fixed, and there is no perturbation in mass density.
- 3D Green's function has been used, although the medium is 2D. There exists a 2D Green's function based on the Hankel function (Červený, 2005), but it was regarded as outside the scope of this thesis.
- For the calculation of the rock physics t-matrix for a single inclusion, only the first-order correction is considered in modelling and inversion. The reason for this is not to further complicate the inversion, as it is already non-linear (Pilskog et al., 2015).
- Only one phase (type) and orientation of fractures are modelled, to reduce the non-linearity. It is assumed that the orientation of fractures is known, which is consistent with Bansal and Sen (2010).

1.3.3 Outline of Thesis

The following work contains six chapters, where each chapter follows a similar structure of theory, methods and numerical results. This chapter, Chapter 1, presents the reader with prior research on the topics of fractured reservoirs and seismic FWI. Objectives and goals of the thesis are explained, while limitations on the scope of work are presented.

The next three chapters follow the general scientific procedure for studying the Earth (Tarantola, 2005):

(i) *Parametrisation of the model*: finding model parameters whose values characterise the system. Elastic stiffness parameters are closely related to fracture parameters and form the basis for the models used in this thesis. This relationship is further discussed in Chapter 2, where two different models for numerical experiments are defined.

(ii) *Forward modelling*: discovery of the physical laws allowing for predicting the results of measurements on some observable parameters. The computation of data for the models, defined from rock physics, is discussed in Chapter 3.

(iii) *Inverse modelling*: use of the actual results of some measurements of the observable parameters to gather the actual values of the model parameters. Elastic FWI is applied in the frequency-domain to the scattering problem associated with fractures. Inversion for the elastic stiffness perturbations are discussed in Chapter 4.

Chapter 5 presents the theory and equations from the previous chapters, and non-linear inversion for fractures are performed based on the DBI method. The results from Chapters 4 and 5 will be discussed together with a summary of the work in Chapter 6. Finally, concluding remarks and suggestions for future work.

Appendix A describes the rock physics G-tensor for ellipsoidal inclusions. In Appendix B, the reference Green's function and its derivatives are given. The leading-term Green's function is derived in Appendix B.1. The first-order derivative is given Appendix B.2, while the second-order derivative is given in Appendix B.3.

Chapter 2

Effective Elastic Properties of Fracture-Induced Anisotropy

Rock physics is an essential topic in the parametrisation of a model, and this chapter introduces the theory behind elastic properties and fractured porous media. First, the general concepts of rock physics and elastic behaviour are established. Then, the effective medium theory for fractured rocks are explained, and different fracture models are presented. The important t-matrix for a single inclusion is defined for fractures, and the corresponding stiffness matrix is derived. A discussion on how fluid saturation affect elastic stiffness is presented. Lastly, numerical experiments and results are presented for the two models introduced in this chapter.

2.1 Mechanical Behaviour of Rocks

For short time scales (less than 10^5 seconds), the mechanical behaviour of rocks is described by the theory of elasticity (Guéguen and Palciauskas, 1994). Hooke's law is the linearised relation between stress, σ, and strain, ε, by the elastic stiffness constants C. Generally, the response (strain) is proportional to the applied force (stress) (Guéguen and Palciauskas, 1994). This relationship is quantified by the physical properties (elastic moduli), depending on the strength of the applied stress. Hooke's law is given by (Auld, 1990; Snieder, 2002)

$$\sigma_{ij} = C_{ijkl}\varepsilon_{kl}, \tag{2.1}$$

where $i, j, k, l \in \{1, 2, 3\}$.

The stress tensor, σ, is composed of the traction forces acting on any surface area of the medium and the normal vector of this surface (Auld, 1990; Snieder, 2002).

Strain, ε, is a measure of material deformation. The linearised strain-displacement relation is given as (Auld, 1990; Guéguen and Palciauskas, 1994):

$$\varepsilon_{kl} = \frac{1}{2}\left(u_{k,l} + u_{l,k}\right), \tag{2.2}$$

where the displacement gradients are defined by $u_{k,l}$ and $u_{l,k}$. Comma-notation is used and can be expressed by $u_{k,l} \equiv \frac{\partial u_k}{\partial x_l}$ and $u_{l,k} \equiv \frac{\partial u_l}{\partial x_k}$.

Elastic stiffness constants, C_{ijkl}, have low values for easily compressed material and vice-versa (Auld, 1990). The elasticity tensor, $\mathbf{C}$, has 81 components, generally, and is a $3 \times 3 \times 3 \times 3$ tensor (Dellinger et al., 1998). However, by symmetry relations, it can be reduced to a symmetric 6x6 matrix with 21 independent elastic parameters (Auld, 1990; Snieder, 2002). Thus, Eq. (2.1) is more commonly written as the generalised (Voigt) Hooke's law:

$$\sigma_I = C_{IJ}\varepsilon_J, \tag{2.3}$$

where $I, J \in \{1, \ldots, 6\}$.

The stiffness parameters, C_{IJ}, can be referred to as Voigt stiffness parameters (Auld, 1990; Jakobsen et al., 2020b). Certain problems require a specific notation, and throughout this work, the various Voigt stiffness notations used are organised in Table 2.1.

Table 2.1: Abbreviated subscript notation compared to spatial coordinates and general coordinate notation.

Abbreviated	Spatial	General
1	xx	x_1x_1
2	yy	x_2x_2
3	zz	x_3x_3
4	yz	x_2x_3
5	xz	x_1x_3
6	xy	x_1x_2

In this work, the elastic stiffness tensor C_{IJ} is given by the *Kelvin* notation. The Kelvin notation adds a weight to stiffness parameters, based on how many elements they represent (Dellinger et al., 1998). This only affects the diagonal elements in the case of a transversely isotropic medium. For example, the C_{44} parameter corresponds to $2C_{2323}$ in Voigt notation, and consequently, a weight of 2 is added in the Kelvin notation. For more details, see Section 2.2.

Compliance, **S**, is the inverse of stiffness and is the measure of how soft a medium is. Hooke's law in terms of compliance (e.g. Schoenberg and Sayers, 1995) is given by the inverse of Eq. (2.1) as

$$\varepsilon_{ij} = S_{ijkl}\sigma_{kl}, \tag{2.4}$$

Interested readers may note that Brown and Korringa (1975) use the compliance tensor, **S**, to extend Gassmann's equations (Gassmann, 1951).

2.2 Seismic Anisotropy

The elastic medium is assumed to be isotropic in most applications of elasticity theory to geophysical problems (Thomsen, 1986). An isotropic medium is characterised by only two independent Voigt stiffness parameters, C_{11} and C_{44}. Isotropic matrices are often used for inclusion models, as one can assume that the inclusions are embedded in the solid isotropic matrix (Jakobsen et al., 2003a). A reservoir without fractures can then be regarded as an isotropic medium (Sayers, 2009). In isotropic media, the elastic wave velocities are independent of the propagation direction (Sayers, 1994).

Rocks often exhibit some anisotropic behaviour from minerals and other constituents (Guéguen and Palciauskas, 1994). A simple example of anisotropy is hexagonal symmetry or transverse isotropy (Thomsen, 1986; Guéguen and Palciauskas, 1994; Ikelle and Amundsen, 2005). Shale formations surrounding sedimentary reservoirs have a transverse isotropy due to clay minerals (Jakobsen and Johansen, 2000; Jakobsen et al., 2003a). A Vertically Transverse Isotropic (VTI) medium has a symmetric axis perpendicular to the vertical axis, x_3, while a Horizontally Transverse Isotropic (HTI) medium has a symmetry axis perpendicular to the horizontal axis, x_1. An example of VTI symmetry is thin horizontal layering, where the alternating layers have different elastic properties. Similarly, an example of HTI symmetry is vertical fractures, where fractures have distinct elastic properties (Ikelle and Amundsen, 2005). Examples of VTI and HTI media are shown in Figs. 2.1a and 2.1b, respectively. The light and dark grey colours in Fig. 2.1 represent the elastic properties of the media.

Transverse isotropic media will have 5 independent Voigt stiffness parameters in 3D (Guéguen and Palciauskas, 1994). Most commonly, a transversely isotropic stiffness tensor with a vertical symmetry axis is used for fractured reservoirs (Zhang et al., 2017). The symmetric VTI stiffness tensor that is used throughout this work, is given with the

Kelvin notation as (Auld, 1990; Guéguen and Palciauskas, 1994)

$$C_{\mathrm{VTI}} = \begin{bmatrix} C_{11} & C_{12} & C_{13} & 0 & 0 & 0 \\ & C_{11} & C_{13} & 0 & 0 & 0 \\ & & C_{33} & 0 & 0 & 0 \\ & & & 2C_{55} & 0 & 0 \\ & & & & 2C_{55} & 0 \\ & & & & & 2C_{66} \end{bmatrix}, \tag{2.5}$$

where $C_{12} = C_{11} - 2C_{66}$. It should be noted that the Kelvin notation adds a weight of 2, to the lower right corner (Dellinger et al., 1998).

In 2D, however, the x_2-component is regarded as zero. This simplification results in only four non-zero independent stiffness parameters, where C_{12} and C_{66} are zero (Lee et al., 2010; Kamath and Tsvankin, 2016).

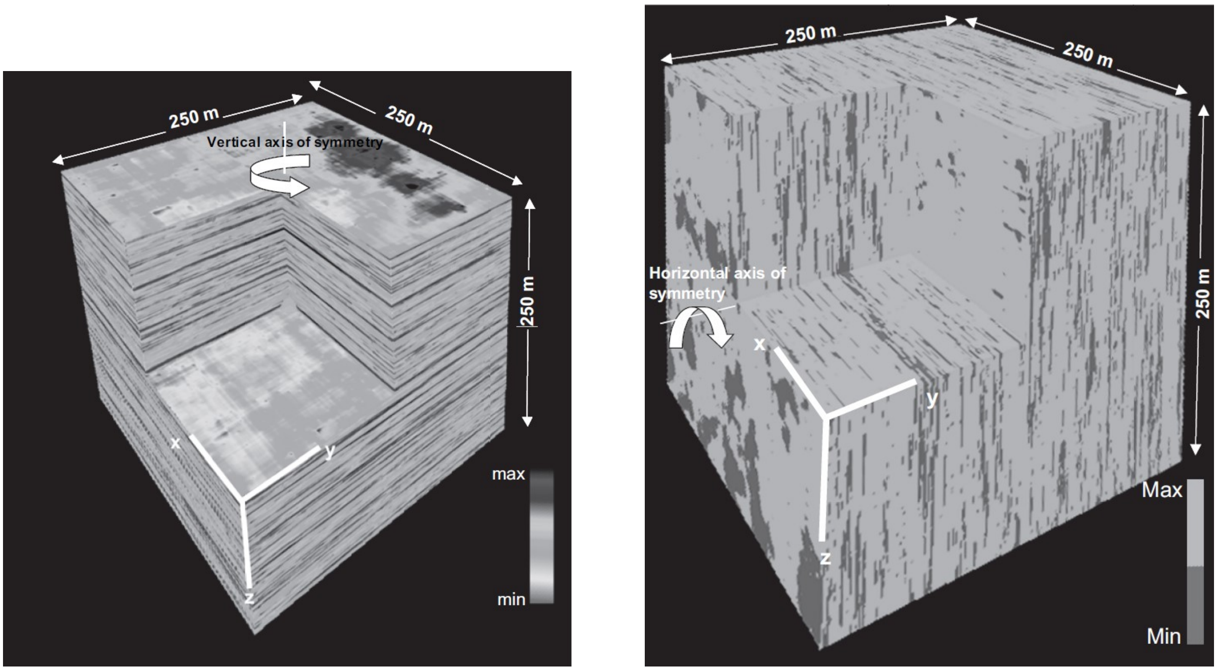

(a) VTI model example: thin horizontal layering.

(b) HTI model example: parallel vertical fractures.

Figure 2.1: Illustrations of VTI and HTI media from Ikelle and Amundsen (2005, p. 531 and 535). A VTI medium (left) has a vertical symmetry axis, while a HTI medium has a horizontal symmetry axis.

The parametrisation of seismic anisotropy is an important topic. In the case of anisotropic elastic media, perturbations in elastic stiffness parameters are used as model parameters (Jakobsen et al., 2020b). One issue of multi-parametrisation is cross-talk which occurs when parameters influence each other. Using the Hessian information (Section 4.2.3) in the inversion can reduce the effects of cross-talk (Jakobsen et al., 2020b). Not all parameters can be recovered when using anisotropic FWI, and elastic FWI suffers from extra parameters (Zhang and Alkhalifah, 2019; Huang et al., 2020a). Due to the considerable number of parameters needed to represent an elastic medium, other parameters have been used to quantify the information. Jakobsen et al. (2017) found that using the weak anisotropy parametrisation in waveform inversion, reduces the cross-talk effects.

In the case of weak anisotropy, three anisotropic parameters can be used instead of the stiffness tensor (Thomsen, 1986). These simplified parameters (ε^*, γ^*, δ^*) indicate the transverse isotropy of the medium, and is calculated from the independent stiffness parameters (Thomsen, 1986; Ali and Jakobsen, 2011a). Mensch and Rasolofosaon (1997) have extended these dimensionless anisotropy parameters to be valid for media of arbitrary symmetry. These coefficients depend on the exact wave modulus, and are closely related to the different polarisations of the P- and S-wave velocities.

In this work, stiffness perturbations are normalised to ensure that the model parameters are of the same size (Jakobsen et al., 2020b).

2.3 Effective Medium Theory for Fractured Rocks

2.3.1 Fractured Porous Media

All macroscopic physical properties of rocks are influenced by the pore microstructure (Guéguen and Palciauskas, 1994). Porosity, ϕ, is the ratio between the pore volume and the total volume of a rock. Rocks are generally composed of many solid constituents and cavities, with a wide range of sizes, shapes, and orientations (Jakobsen et al., 2003b). Cavities like cracks or fractures can be seen as thin needle-shaped pores with low volumes. When dealing with an elastic fractured media, it is crucial to look at the effective properties of the medium (e.g. Hornby et al., 1994; Jakobsen et al., 2003a). Fractured reservoirs often contain sets of fractures with different orientations (Sayers, 2009).

The terminology *fracture* is used in this thesis, as opposed to cracks, which can be referred to as microcracks. Kranz (1983) argues that a microcrack and a microfracture is the same, although in this work fractures have a slightly higher aspect ratio than microcracks. A fracture can also be defined as a planar feature of permeability discontinuity (Sævik et al., 2013). Faulted reservoirs can be represented by fractures or deformation bands (Ali et al., 2011). However, in this thesis, the fractures in faults are not investigated, as they can be regarded as bigger than “normal” fractures.

Typically, seismic wavelengths are significantly longer than the length of fractures (Hudson, 1981; Bakulin et al., 2000). Hence, an average response of many fractures is observed in measurements. Seismic waves propagate through two-phase media, where one phase is the matrix, and the other phase is embedded inclusions (Kuster and Toksöz, 1974; Guéguen and Palciauskas, 1994). In practice, a fractured medium can be replaced by an effective medium. The effective medium acts like an anisotropic medium, if the fractures are closely spaced and parallel (Bansal and Sen, 2010).

Two essential quantities that describe fractures are the unit-less variables; aspect ratio, α_c, and fracture density, ϵ. Aspect ratio is defined as $\alpha_c \equiv \frac{c}{a}$ and is the ratio between the semi-minor axis, c, and the semi-major axis, a, of a spheroid. Fracture density is given as $\epsilon = \xi a^3$ and represents the number of fractures, ξ, per unit volume (Hudson, 1980; Schoenberg and Douma, 1988; Bakulin et al., 2000). A low aspect ratio, e.g. $\alpha_c \leq 1/20$, will result in a needle-shaped fracture, as described above. An illustration of fractures is shown in Fig. 2.2. On the left, the characteristic inclusion is given, while more realistic fractures are presented on the right.

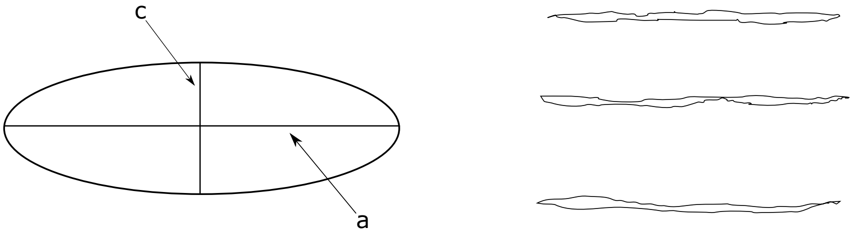

Figure 2.2: Fracture-illustrations. Left: inclusion with a major axis a and a minor axis c. Right: physically reasonable horizontal fractures with a low aspect ratio. Inspired by Shahraini et al. (2011).

When a rock is subjected to applied stress, fractures close, and the effective elastic moduli increase (Mavko et al., 2009). The effective elastic stiffness tensor, $\mathbf{C}$, can be viewed as a function of fracture density (Ali and Jakobsen, 2011a). See Fig. 2.3 in Section 2.4 for an example of this relationship.

2.3.2 Fracture Models

The main effective media theories for fractured rocks are parallel linear-slip interfaces (e.g. Schoenberg and Douma, 1988; Bakulin et al., 2000; Bansal and Sen, 2010), and penny-shaped fractures (e.g. Hudson, 1980; Bakulin et al., 2000; Jakobsen et al., 2003a; Grechka, 2005). Bakulin et al. (2000) performed a comparison of the two models, and found that they are quite similar.

One way to obtain effective parameters is treating fractures, regardless of their shape and microstructure, either as (1) infinitely thin and highly compliant (soft) layers, or (2) planes of weakness with linear-slip boundary conditions (Bakulin et al., 2000).

In the case of parallel thin, soft layers (1) one looks at the effective compliance matrix. Parameters for linear-slip models are normal and tangential weakness (Bansal and Sen, 2010). If the weaknesses (normal and tangential) are zero, the medium is unfractured, but if the weaknesses approach one, it is extremely fractured (Sayers, 2009). These parameters confirm the azimuthal anisotropy, even when the normal weakness is very low (Schoenberg and Douma, 1988).

Hudson's model for a fractured media is based on fractures being viewed as elliptic penny-shaped fractures (Hudson, 1980; Hudson, 1981). An underlying assumption is that the fractures are flat and that they can be modelled with aspect ratio $\alpha_c \ll 1$ (Schoenberg and Douma, 1988). However, one can model non-flat ellipsoidal inclusions by using an iterative method for incrementally increasing fracture density ϵ (see Nishizawa, 1982; Schoenberg and Douma, 1988). In the case of isolated penny-shaped fractures, Bakulin et al. (2000) found expressions for weak anisotropic coefficients in dry (or gas-filled) fractures and fluid-filled fractures. Note that weaknesses can also be used to parametrise penny-shaped fractures. In that case, the tangential weakness is twice the fracture density, while the normal weakness is sensitive to fluid saturation (Bakulin et al., 2000).

One requirement for the Hudson fracture model is that both small aspect ratios and fracture densities are assumed, for an ideal fracture shape (Hudson, 1981; Mavko et al., 2009). Another limitation is that this fracture model is mainly appropriate for waves of high frequency (Brown and Korringa, 1975).

The fracture model used in this thesis is based on Hudson's model, as it is consistent with the t-matrix representation for fractures by Jakobsen et al. (2003a). The reason for this is that this thesis is a continuation of Pilskog et al. (2015), where this fracture representation was used.

2.3.3 t-matrix for a Single Inclusion

In heterogeneous material, Hooke's law of Eq. (2.3) can be written as (Guéguen and Palciauskas, 1994; Jakobsen et al., 2003a)

$$\bar{\boldsymbol{\sigma}} = \mathbf{C} : \bar{\boldsymbol{\varepsilon}}, \tag{2.6}$$

where $\bar{\boldsymbol{\sigma}}$ is the average stress tensor, $\bar{\boldsymbol{\varepsilon}}$ is the average strain tensor, and $\mathbf{C}$ is the effective elastic stiffness tensor.

For a material that is homogeneous on macroscopic scale (statistically), the effective elastic tensor (Jakobsen et al., 2003a) is shown in Eq. (2.7) as

$$\mathbf{C} = \mathbf{C}^{(0)} + \Delta\mathbf{C}. \tag{2.7}$$

Reservoirs contain several sets of fractures with variable orientation within a given fracture set, denoted by p, r (Sayers, 2009). Effects of ellipsoidal inclusions (fractures) on the stiffness perturbation, can be approximated by the t-matrix for an inclusion, $\mathbf{t}$. Perturbation in the elastic tensor is given for an arbitrary inclusion type p, r (Jakobsen et al., 2003a,b; Ali and Jakobsen, 2011b; Shahraini et al., 2011) as

$$\Delta\mathbf{C} = \mathbf{C}_1 : \left[\mathbf{I}_2 + \mathbf{C}_1^{-1} : \mathbf{C}_2\right]^{-1}, \tag{2.8}$$

where the first-order correction (approximation for isolated fractures) is given by

$$\mathbf{C}_1 = \sum_{p=1}^{N} \phi_c^{(p)} \mathbf{t}^{(p)}, \tag{2.9}$$

and the second-order correction (fracture-fracture interaction) is given as

$$\mathbf{C}_2 = \sum_{p=1}^{N}\sum_{r=1}^{N} \phi_c^{(p)} \mathbf{t}^{(p)} : \mathbf{G}_d^{(pr)} : \mathbf{t}^{(r)} \phi_c^{(r)}. \tag{2.10}$$

Here, $\mathbf{G}_d$ is the strain Green's tensor integrated over a characteristic spheroid (see Jakobsen et al., 2003a; Shahraini et al., 2011), $\mathbf{I}$ is the identity matrix, ϕ_c is the fracture porosity, and $\mathbf{t}$ is the t-matrix of a single inclusion for a fracture set p, r. For isolated fractures of type r, the t-matrix is given by (Jakobsen et al., 2003a; Pilskog et al., 2015)

$$\boldsymbol{t}^{(r)} = \Delta\mathbf{C}^{(r)} \left(\mathbf{I} - \mathbf{G}^{(r)} \Delta\mathbf{C}^{(r)}\right)^{-1}, \tag{2.11}$$

where $\Delta\mathbf{C}^{(r)} = \mathbf{C}^{(r)} - \mathbf{C}^{(0)}$ based on Eq. (2.7).

Following Jakobsen et al. (2003a), an expression for the effective stiffness can be rewritten by combining Eqs. (2.7) and (2.8), to yield

$$\mathbf{C} = \mathbf{C}^{(0)} + \mathbf{C}_1 : \left[\mathbf{I}_2 + \mathbf{C}_1^{-1}\mathbf{C}_2\right]^{-1}, \tag{2.12}$$

where $\mathbf{I}_2$ denotes the second-rank identity matrix of dimensions 6 × 6.

The higher-order approximation, in Eq. (2.10), does not converge and dominates the first-order approximation, in Eq. (2.9), resulting in an increased effective moduli for increasing fracture density (Cheng, 1993; Jakobsen et al., 2003a). Ignoring the higher-order corrections, in Eq. (2.10), and considering only one fracture set $p = 1$, yields

$$\mathbf{C} = \mathbf{C}^{(0)} + \mathbf{C}_1, \tag{2.13}$$

where $\mathbf{C}_1$ was given in Eq. (2.9).

If the porosities and permeabilities of the medium are sufficiently low, fractures can be considered to be isolated (Pilskog et al., 2015). Thus, the t-matrix for a single inclusion in Eq. (2.11) can be rewritten as (Jakobsen et al., 2003a; Jakobsen, 2004; Pilskog et al., 2015)

$$\mathbf{t} = \left(\mathbf{C} - \mathbf{C}^{(0)}\right) : \left[\mathbf{I}_2 - \mathbf{G} : (\mathbf{C} - \mathbf{C}^{(0)})\right]^{-1}, \tag{2.14}$$

where $\mathbf{G}$ represents the constant, negative strain Green's tensor integrated over an ellipsoid (Eshelby, 1957; Jakobsen et al., 2003a; Jakobsen and Johansen, 2005), given by $\mathbf{G}(\mathbf{C}^{(0)}, \alpha_c)$. See Appendix A for details on how this tensor is calculated.

The effective stiffness, $\mathbf{C}$, can be set to $\mathbf{0}$, in the case of dry (empty) cavities (Ponte Castañeda and Willis, 1995; Jakobsen, 2004). In this case, the t-matrix is simplified to

$$\mathbf{t} = -\mathbf{C}^{(0)} : \left[\mathbf{I}_2 + \mathbf{G} : \mathbf{C}^{(0)}\right]^{-1}. \tag{2.15}$$

The volume (porosity) of a thin, penny-shaped ellipsoidal fracture is defined as (Hudson, 1981; Cheng, 1993; Jakobsen et al., 2003a)

$$\phi_c = \frac{4\pi\alpha_c}{3}\epsilon, \tag{2.16}$$

where ϵ is the fracture density and α_c is the aspect ratio of fractures.

From Eq. (2.13) and (2.16), the elastic stiffness perturbation tensor is given by

$$\Delta\mathbf{C} = \frac{4\pi\alpha_c}{3}\mathbf{t}\epsilon, \tag{2.17}$$

where $\mathbf{t}$ is a constant matrix depending on α_c. Both the stiffness perturbation and fracture density are dependent on the position, $\mathbf{x}$, by $\Delta\mathbf{C} = \Delta\mathbf{C}(\mathbf{x})$, and $\epsilon = \epsilon(\mathbf{x})$. To retain a symbolic (vector) notation, this position $\mathbf{x}$ is ignored for now.

This means that the effective stiffness, $\mathbf{C}$, in Eq. (2.7) can be redefined, as shown in Eq. (2.18):

$$\mathbf{C} = \mathbf{C}^{(0)} + \frac{4\pi\alpha_c}{3}\mathbf{t}\epsilon. \tag{2.18}$$

Subsequently, the result of the above discussion is that a linear relationship between the stiffness perturbation and the fracture density has been established. The expression in Eq. (2.18) is key in the calculation of the stiffness perturbations, in Section 2.3.5. Ultimately, the relations in Eqs. (2.17) and (2.18), are used to invert for fractures in Chapter 5.

2.3.4 Effects of Fluid Saturation

Rocks are generally saturated or partly saturated with fluids. If the fractures are filled with fluid, the effective stiffness is equal to the fluid stiffness tensor $\mathbf{C}_f$. Eq. (2.14) can then be written as (Pilskog et al., 2015)

$$\mathbf{t} = \left(\mathbf{C}_f - \mathbf{C}^{(0)}\right) : \left[\mathbf{I}_2 - \mathbf{G} : (\mathbf{C}_f - \mathbf{C}^{(0)})\right]^{-1}, \tag{2.19}$$

where $\mathbf{C}_f$ is given below, in Eq. (2.22).

Jakobsen et al. (2003b) extended the t-matrix expression in Eq. (2.19) to fully saturated media, with communicating pores. Saturated fractures usually communicate and are not isolated (Jakobsen and Hudson, 2003), but in the context of this work, it is assumed that fractures are isolated. This t-matrix could ideally be used to calculate the effect of fluid-saturation on effective properties of a fractured porous medium, as it is Gassmann-consistent (see Jakobsen and Pilskog, 2016). However, as the expression introduces more parameters (e.g. viscosity and relaxation time) and thus complicates the inversion process in Chapter 5, the well-known Gassmann equation is used instead (Gassmann, 1951; Guéguen and Palciauskas, 1994; Bredesen et al., 2015). Gassmann's relation is given in Eq. (2.20) as:

$$K_u = K_d + \frac{\left(1 - \frac{K_d}{K_s}\right)^2}{\frac{\phi}{K_f} + \frac{1-\phi}{K_s} - \frac{K_d}{K_s^2}}, \tag{2.20}$$

where K_u is the undrained (saturated) bulk modulus, K_d is the dry bulk modulus, K_s is the solid (mineral) bulk modulus, and ϕ is the porosity. The saturated (undrained) shear modulus, μ_u, is the same as the dry shear modulus, μ_d, and therefore unaffected by fluid saturation. The fluid bulk modulus, K_f, depends on fluid content and is given in Eq. (2.21).

It should be noted that Brown and Korringa (1975) updated Eq. (2.20) to be valid for generalised (anisotropic) media. Shahraini et al. (2011) used the generalised Gassmann expressions to characterise fractured (saturated) reservoirs. Similarly to above, the anisotropic Gassmann was regarded as outside the scope of this thesis.

Gassmann's equations assume that the moduli are unaffected by chemical reactions between porous rocks and fluid. In addition, the medium is undrained rather than dry and valid for waves of low frequency (Brown and Korringa, 1975; Berryman, 1999).

If the medium is partially saturated, K_f must be regarded as an effective fluid bulk modulus. The original Wood's formula (Wood, 1955) is given by

$$\frac{1}{K_f} = \frac{S_w}{K_w} + \frac{(1 - S_w)}{K_g}, \tag{2.21}$$

where S_w is the water saturation, K_w is the bulk modulus of water, and K_g is the bulk modulus for gas. Interested readers should note that Jin et al. (2018) gives an updated formula for K_f.

The symmetric stiffness tensor for a fluid-filled medium is given by

$$\mathbf{C}_f = \begin{bmatrix} K_f & K_f & K_f & 0 & 0 & 0 \\ & K_f & K_f & 0 & 0 & 0 \\ & & K_f & 0 & 0 & 0 \\ & & & 0 & 0 & 0 \\ & & & & 0 & 0 \\ & & & & & 0 \end{bmatrix}. \tag{2.22}$$

The fluid bulk modulus can be calculated by $K_f = c_f^2 \rho_f$ (Mavko et al., 2009), where c_f and ρ_f is the velocity and density of the fluid, respectively. An example: gas has a fluid-velocity of $c_f \approx 620$ m/s, and fluid density of $\rho_f \approx 65$ kg/m^3, resulting in a fluid bulk modulus of $K_f \approx 2.5 \cdot 10^7$ Pa (Mavko et al., 2009; Jin et al., 2018).

2.3.5 Relationship Between Stiffness and Fracture Density

The effective stiffness, as in Eq. (2.18), depend on both fracture density and position $\mathbf{x}$. Rewriting the effective stiffness with abbreviated notation, yields

$$C_{IJ}(\mathbf{x}) = C_{IJ}^{(0)}(\mathbf{x}) + \frac{4\pi}{3}\alpha_c t_{IJ} \epsilon(\mathbf{x}), \tag{2.23}$$

where in the case of an isotropic reference medium, $C_{IJ}^{(0)}(\mathbf{x})$ simplifies to $C_{IJ}^{(0)}$.

In the context of this thesis, the most relevant way to view the relationship between elastic stiffness and fracture density, is by the stiffness perturbation defined in Eq. (2.17). Redefining Eq. (2.17) with positions $\mathbf{x}$ and abbreviated notation, yields the following expression

$$\Delta C_{IJ}(\mathbf{x}) = \frac{4\pi}{3}\alpha_c t_{IJ}\epsilon(\mathbf{x}), \tag{2.24}$$

where t_{IJ} is dependent on the Green's tensor G_{IJ}, given in Appendix A. Both t_{IJ} and G_{IJ} are constant for all positions $\mathbf{x}$. The arbitrary position $\mathbf{x}$ could be any in the scattering domain Ω.

For example, the stiffness perturbation ΔC_{11} for a given position $\mathbf{x}$ is given by Eq. (2.25).

$$\Delta C_{11}(\mathbf{x}) = \frac{4\pi}{3}\alpha_c t_{11}\epsilon(\mathbf{x}). \tag{2.25}$$

In Algorithm 1, the procedure used in this thesis to calculate stiffness for a fractured medium is presented.

Algorithm 1: Procedure for calculating the stiffness perturbation and effective stiffness of the given fracture densities, ϵ, of the (geologic) model. This algorithm follows a procedure that was introduced in Avseth et al. (2010).

```
Define values for velocities $\alpha$ and $\beta$, and density $\rho$ in the initial background medium.
Saturate the dry medium with a fluid, $K_f$, by Gassmann's relations in Eq. (2.20).
Update the effective density by $\rho^* = (1-\phi)\rho + \phi\rho_f$, where $\phi$ is porosity (of pores).
Use these values ($K_u$, $\mu_u$, $\rho^*$) to calculate the isotropic reference medium $\mathbf{C}^{(0)}$.
Set aspect ratio $\alpha_c$, and define fracture density, $\epsilon$, for each grid block in the model.
if dry then
    Set $\mathbf{C} = \mathbf{0}$.
else
    Set $\mathbf{C} = \mathbf{C}_f$ based on the $K_f$ of the fluid. $\mathbf{C}_f$ is given in Eq. (2.22).
end
Calculate the rock physics G-tensor $\mathbf{G}(\mathbf{C}^{(0)}, \alpha_c)$, given in Appendix A.
Determine the t-matrix $\mathbf{t}$ in Eq. (2.19), by $\mathbf{C}$, $\mathbf{C}^{(0)}$, and $\mathbf{G}$.
Estimate the normalised stiffness perturbation tensor, $\Delta\mathbf{C}$, in Eq. (2.24).
Estimate effective stiffness, $\mathbf{C}$, in Eq. (2.23).
```

The procedure above, Algorithm 1, is important for calculating stiffness in the numerical experiments in Section 2.4. Each fracture density model has four corresponding effective stiffness tensors calculated by Eq. (2.23). For the forward and inverse modelling, in Chapters 3 and 4 respectively, the stiffness perturbation is used as the model parameter. The computation of these stiffness perturbations are based on Eq. (2.24).

2.4 Numerical Results and Discussion

In the first numerical experiment, effective stiffness is calculated based on changing fracture density. The procedure for calculating this is given in Algorithm 1. More importantly, the fracture density models for the *syncline model* (Section 2.4.1) and the *anticline model* (Section 2.4.2) are explained and displayed. When considering both models in Sections 2.4.1 and 2.4.2, one observation is that fractures make the medium softer (decreasing stiffness). This implies that C_{33} will decrease with increasing fracture density, whereas C_{11} will barely change. The effective stiffness, as shown in Tables 2.2 and 2.3, are similar to the stiffness perturbation models defined in Chapter 3. The main differences between the models are further discussed in Chapters 4 and 5.

The properties of the reference medium are based on (dry) tight-gas sandstone from Mavko et al. (2009). Velocities are $\alpha = 4670$ m/s and $\beta = 3060$ m/s. The mass density is $\rho = 2510$ kg/m^3, and porosity is $\phi = 0.05$. These values were used to calculate the background stiffness tensor $\mathbf{C}^{(0)}$. It should be noted that these velocities are somewhat higher than the typical values, considering the (physical) depth of these experiments. Lower velocities are expected for media close to the surface. However, these values have been used to best approximate a real reservoir rock independent of depth.

In these results, fractures are *gas-filled*, *horizontally aligned* and consistent with Hudson (1980) and Jakobsen et al. (2003a). The aspect ratio of fractures to be used is $\alpha_c = 0.001$, and one type and orientation of fractures is assumed. Assuming that the saturated porous medium is filled with fractures containing saturations of gas, the effective stiffness for increasing fracture density can be estimated. A 3D VTI medium are characterised by five independent elastic stiffness parameters C_{11}, C_{33}, C_{55}, C_{66}, and C_{13}, where C_{12} depend on C_{11} and C_{66}. See Eq. (2.5) for the stiffness tensor.

The comparison in effective stiffness for increasing fracture density with dry, water-filled (100% water), and gas-filled (100% gas) fractures are presented in Fig. 2.3. It can be observed that the effective stiffness of water-filled fractures is higher than that of gas-filled fractures. Fluid-filled fractures have a higher stiffness, as the density is increased with the introduction of a fluid instead of a dry fracture. When the dry fractures are saturated with a fluid, the stiffness does not change for C_{55} and C_{66}. These stiffness coefficients depend on the shear modulus, which is zero for fluids. Horizontal fractures do not (significantly) influence parameters without the vertical component x_3, i.e. C_{11} and C_{66} (Guéguen and Palciauskas, 1994).

The difference between the first- and higher-order correction for fractures is mainly that the first-order is linear, while the higher-order is non-linear. See Fig. 2.4 for an example of how stiffness changes for the corrections, depending on increasing fracture density. The first-order correction gives a negative stiffness in C_{33} and C_{13} for a fracture density close to 0.2, which is physically impossible. The cause for this is likely that the Hudson model breaks down for fracture densities over 0.1, when only accounting for the first-order correction (see Cheng, 1993; Jakobsen et al., 2003a). In the later chapters, only the first-order correction is accounted for to avoid non-linearity when calculating the sensitivity matrix.

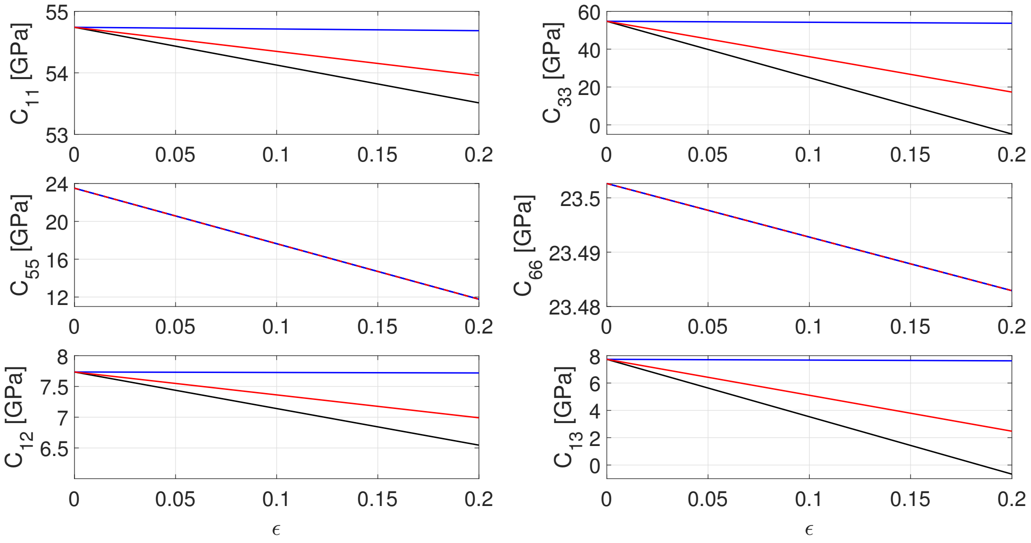

Figure 2.3: Effective stiffness values of dry (black), water-filled (blue) and gas-filled (red) fractures. Stiffness values were calculated based on the first-order correction for fractures, and the six coefficients correspond to a 3D VTI medium.

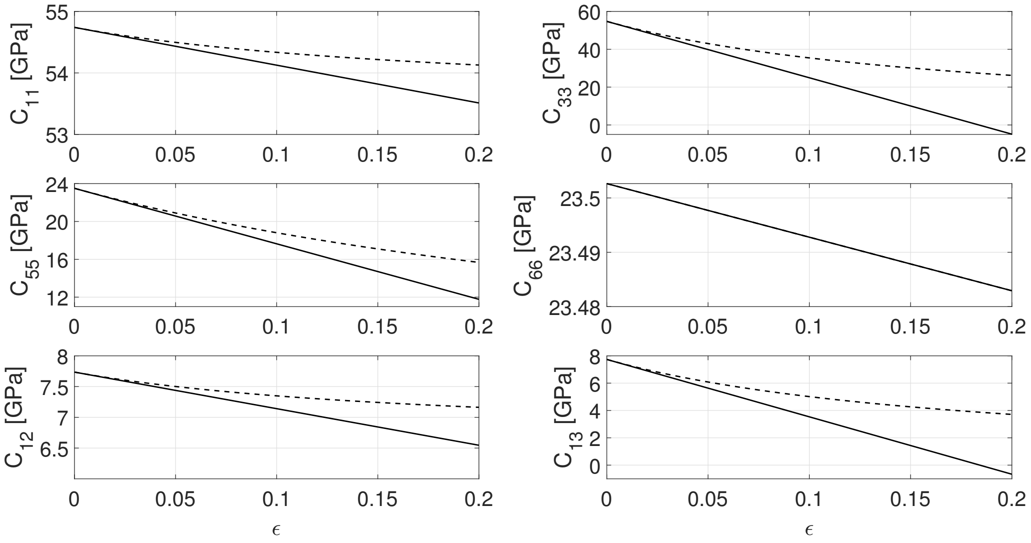

Figure 2.4: Effective stiffness coefficients of the first-order correction (solid) and second-order correction (dashed), for a 3D VTI medium.

2.4.1 Syncline Model

The first fracture density model is a 2D syncline model, which is mainly based on Bansal and Sen (2010) and Jakobsen and Pilskog (2016). The syncline can be described as a trough of stratified rock. There are three layers with different fracture density in the model. In the case of amplitude versus offset and azimuth (AVOA), this syncline makes it fail (Bansal and Sen, 2010).

The top layer has no fracture density ($\epsilon = 0$), the middle layer has a higher fracture density ($\epsilon = 0.045$), and the bottom layer has the highest fracture density ($\epsilon = 0.09$). These values are similar to those used in Bansal and Sen (2010), and give a low to moderate fracture density according to Ali and Jakobsen (2011a). Fracture density corresponds to the amount of fractures within an area, as described in previous sections. In Table 2.2 are the respective effective stiffness values shown for 2D VTI medium corresponding to the model depending on the fracture densities mentioned above. In a 2D VTI model, x_2 does not exist, so that the only non-zero stiffness coefficients are C_{11}, C_{33}, C_{55}, and C_{13}.

Following the procedure in Algorithm 1, Gassmann's equations was used to saturate the medium with gas, where a quartz and clay solid matrix of $K_s = 39$ GPa was assumed. In consequence, the velocities in the gas-saturated reference medium are $\alpha = 4780$ m/s and $\beta = 3132$ m/s. Mass density was set to $\rho = 2395$ kg/m^3, and the porosity is 0.05 (5%).

There are a total of 1025 grid blocks in the syncline model, and the number of grid block is 41 and 25 in the x- and z-directions, respectively. The maximum offset in these simulations, is set to 984 m, while the maximum depth is set to 600 m. A grid block of dimension 24 m x 24 m represents each scatter point. The grid block size was chosen to be small compared to the dominant wavelength of the S-wave, which is 313 m for waves with a maximum frequency of 10 Hz.

Table 2.2: Effective stiffness coefficients, C^*_{IJ} [GPa], in the syncline model corresponding to the different fracture densities, ϵ [unit].

Layer	ϵ	C^*_{11}	C^*_{33}	C^*_{55}	C^*_{13}
Reference / Layer 1	0.000	54.74	54.74	47.01	7.74
Layer 2	0.045	54.46	41.33	44.37	5.85
Layer 3	0.090	54.19	27.92	41.73	3.96

The true fracture density of the syncline model is shown in Fig. 2.5, with offset on the x-axis, L_x, and depth on the y-axis, L_z. The fracture density of this model is of fairly low contrast, even though the changes are notable. Note that the colour map limit values have been increased by 25%, as values above the maximum fracture density of 0.09 are expected in the inversion results in Section 5.3.

In Figs. 2.6, the corresponding effective stiffness values are displayed for the fracture density model with the same colour bar range. For the effective stiffness values, the most considerable change is in the C_{33} coefficient of Fig. 2.6b. This substantial change is expected, as the vertical component is the most susceptible to changes due to horizontal fractures. In the case of the C_{55} and C_{13} coefficients, of Figs. 2.6c and 2.6d, the stiffness change due to fractures is less noticeable. Even though the change in C_{11} is minimal, as per Table 2.2, it is still shown for completeness. These figures show the relative difference between the effective elastic coefficients and the fracture density, corresponding to the values in Table 2.2. A good example is the C_{33} coefficient, as the stiffness decreases in Fig. 2.6b for an increase in fracture density of Fig. 2.5. Finally, the fracture model in Fig. 2.5 will be used as a reference point for the fracture density inversion results in Chapter 5, more specifically Section 5.3.1.

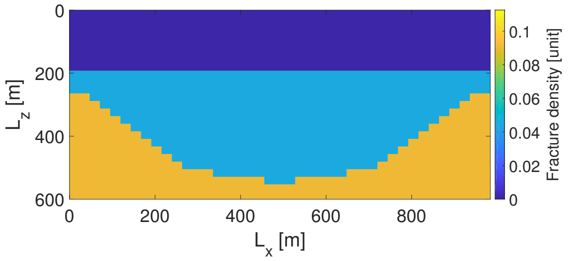

Figure 2.5: Fracture density in the syncline model.

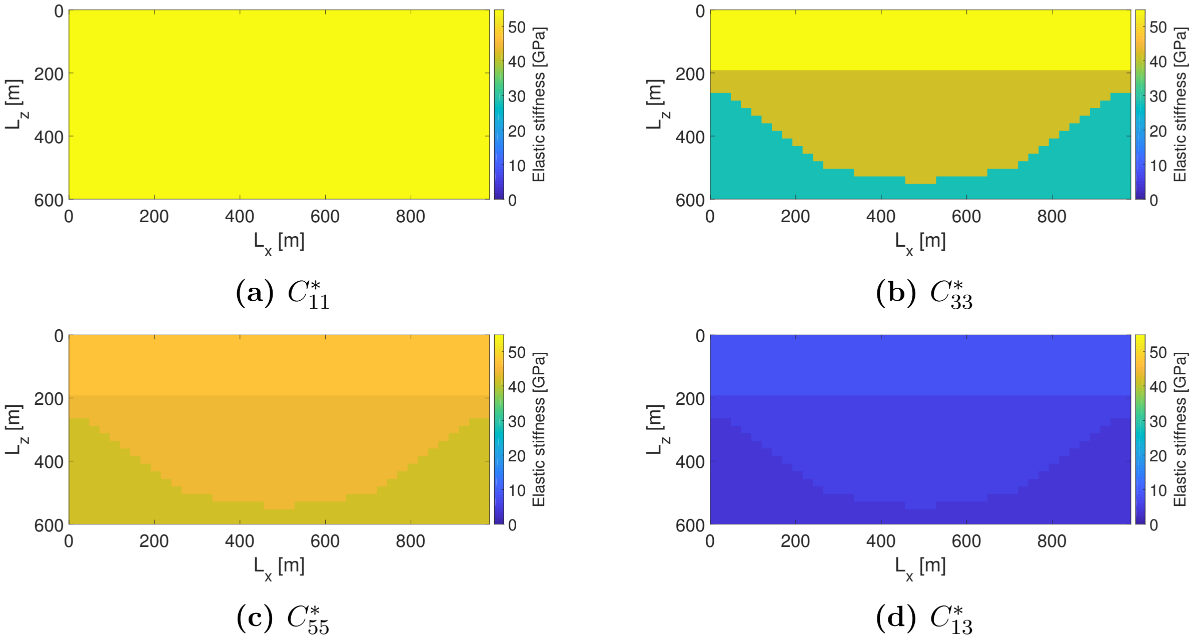

(a) C_{11}^*

(b) C_{33}^*

(c) C_{55}^*

(d) C_{13}^*

Figure 2.6: Effective elastic stiffness parameters of the 2D VTI syncline model. The colour map is the same for all parameters.

2.4.2 Anticline Model

The second model used in this thesis is a more complex, asymmetric 2D model based on Pilskog et al. (2015) and Jakobsen and Ursin (2015). The reason for this model, specifically, is to test the accuracy of inversion for different parameters in the case of a more asymmetric and complex model.

Geologically, the anticline model has tilted layers (upper and lower) with an anticline in the middle layer. An arch-like shape is often called an anticline, and is a well-known structural trap (Ikelle and Amundsen, 2005). The anticline in this model has a steeper slope than the tilted layers. The top layer in the anticline model contains hardly any fractures ($\epsilon = 0.01$), while the third and largest layer contains the most fractures ($\epsilon = 0.08$). Values for fracture density used in this model, are comparable to those used in Pilskog et al. (2015). The respective effective stiffness values for a 2D VTI medium, corresponding to the anticline model depending on fracture density, is given in Table 2.3. The reference-layer is the isotropic (unfractured) reference medium.

The reference medium is different in this anticline model compared to the syncline model in Section 2.4.1, as values from Pilskog et al. (2015) were used. Initially, the values for the velocities were $\alpha = 3700$ m/s and $\beta = 2500$ m/s, while the mass density was $\rho = 2500$ kg/m^3. Then, Gassmann was again used to saturate the medium with gas, where a quartz and clay solid matrix was assumed. Consequently, the properties of the gas-saturated reference medium are $\alpha = 3882$ m/s, $\beta = 2623$ m/s and $\rho = 2271$ kg/m^3.

The total number of grid blocks in the anticline model is 1107, which is similar to the syncline model. Consequently, the total grid dimensions of this model are 41 and 27 in the x- and z-directions, respectively. The maximum offset is 984 m, and the maximum depth is 648 m. Grid block size is 24 m x 24 m, based on the dominant wavelength of the S-wave, which is 262 m. Note that the number of sources is significantly lower than for the syncline model.

Table 2.3: Effective stiffness coefficients, C^*_{IJ} [GPa], in the anticline model corresponding to the different fracture densities, ϵ [unit].

Layer	ϵ	C^*_{11}	C^*_{33}	C^*_{55}	C^*_{13}
Reference	0.00	34.23	34.23	31.25	2.98
Layer 1	0.01	34.21	32.39	30.85	2.82
Layer 2	0.03	34.18	28.71	30.05	2.50
Layer 3	0.08	34.10	19.51	28.05	1.70
Layer 4	0.05	34.15	25.03	29.25	2.18

The fracture density of this model is displayed in Fig. 2.7. Note that the colour map limit values have been modified by 25%, as values outside the fracture density range of $[0.01, 0.08]$ are expected in the inversion results.

Effective stiffness coefficients corresponding to the fracture density model, are displayed for this in Fig. 2.8. All these figures have the same colour bar, depending on the elastic stiffness in GPa, and will be discussed below. For the effective stiffness values, the most considerable change is again in the C_{33} coefficient of Fig. 2.8b. In the case of the C_{55} and C_{13} coefficients, of Figs. 2.8c and 2.8d, the stiffness change due to fractures is less noticeable. As in the previous (syncline) model, the C_{11} change is shown for completeness. Ultimately, this fracture density model will be used in the comparison between the final inversion results and the true model presented in this section. This is further discussed in Chapter 5, or more specifically Section 5.3.2.

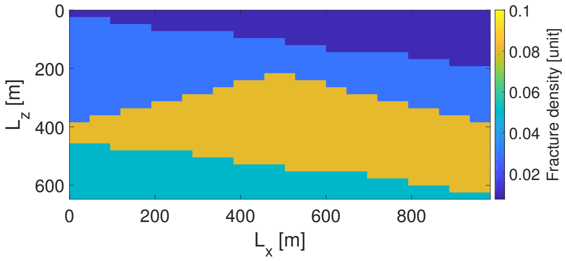

Figure 2.7: Fracture density of the anticline model.

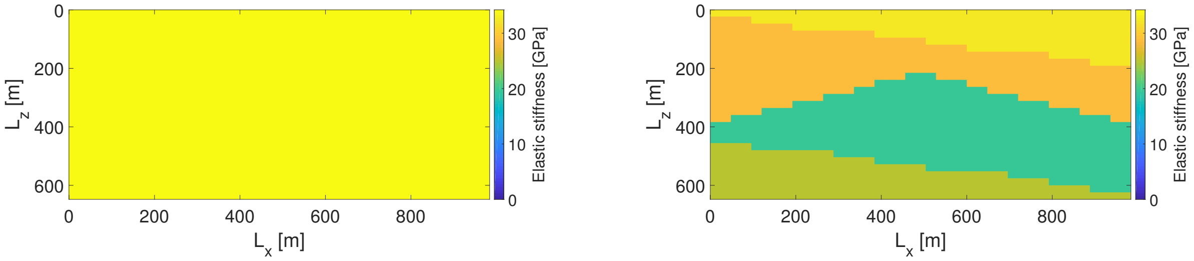

(a) C^*_{11}

(b) C^*_{33}

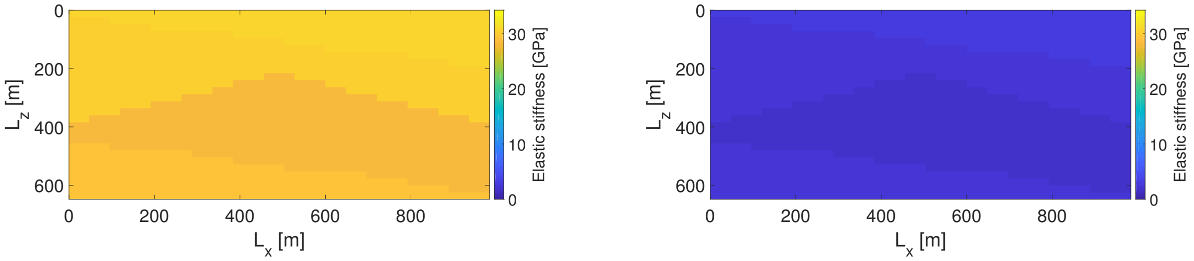

(c) C^*_{55}

(d) C^*_{13}

Figure 2.8: Effective elastic stiffness parameters of the 2D VTI anticline model. The colour map is the same for all parameters.

Chapter 3

Seismic Waveform Modelling

The forward or direct problem is one of the main topics of seismic modelling, and the key features will be elaborated in this chapter. Calculation of observed (synthetic) data is essential in seismic modelling. First, the main details behind the modelling theory are explained. Then, the elastodynamic wave equation is introduced for an anisotropic media, and the well-known Lippmann-Schwinger equation is derived. The final equation is solved exactly, resulting in the data. Finally, numerical results are presented for the two models referenced in the previous chapter.

3.1 Introduction

The principal aim of forward modelling is to predict the results of measurements, based on a model (Ikelle and Amundsen, 2005; Menke, 2012). In seismic modelling of an elastic media, this is done by solving the elastodynamic wave equation for a geologic model. Elastodynamic refer to vector waves, with three different polarisations, and are modelled by the use of an elastodynamic wave equation (Snieder, 2002).

A seismogram is the registration of particle displacement components at receiver positions, for a given source-receiver configuration. Synthetic seismograms simulate the response of a geologic model (Kelly et al., 1976). These synthetic seismograms can be compared to real seismic data to verify the predicted model (Krebes, 2004). Carcione et al. (2002) classifies the main methods of modelling as: direct methods, ray-tracing methods, and integral-methods.

In direct methods, the wave equation is solved for a model which is discretised in a finite number of closely-spaced points (Carcione et al., 2002; Ikelle and Amundsen, 2005). The best example of a direct method is the finite difference method (FD). For a sufficient discretisation in space and time, FD is the most accurate method for simulating elastic-wave propagation through complex models (Ikelle and Amundsen, 2005). The main disadvantage is the high cost of computational resources (Carcione et al., 2002; Krebes, 2004).

Ray-tracing (asymptotic) methods uses a high-frequency approximation to find a solution to the wave equation (Carcione et al., 2002; Červený, 2005). The travel times and amplitudes of seismic waves are calculated along ray paths in a heterogeneous medium (Krebes, 2004). The seismic ray method can be divided into kinematic and dynamic ray-tracing (Červený, 2005). Ray-Born modelling has been a popular method for modelling, as it combines asymptotic ray theory and the Born approximation for scattering problems (Červený and Coppoli, 1992; Červený, 2005; Bansal and Sen, 2010). The main drawback of the ray-method is the lack of accuracy near-critical offsets in addition to not accounting for multiple scattering (Krebes, 2004; Červený, 2005).

Integral-equation methods follow Huygens' principle, where the wavefield is a superposition of waves due to point sources (Carcione et al., 2002). Generally, these methods are combined with the scattering theory for elastodynamic waves (Snieder, 2002). Carcione et al. (2002) specifies two types: domain (volume) integral-equations and boundary integral-equations. Interested readers should note that Ursin and Tygel (1997) compared the volume-based (domain) and surface-based (boundary) integral-methods, and found they are related by the divergence theorem. Similar to FD, the computational complexity poses a problem due to storing large matrices (Carcione et al., 2002). The direct scattering solution, employed in this work, is a volume-based integral-equation approach where the inversion is for small pixels.

Jakobsen et al. (2020a) describes several advantages of the integral-equation methods compared to the direct methods (e.g. FD). First of all, the approach is target-oriented as the target of interest in inversion can be specified (Jakobsen and Wu, 2018; Huang et al., 2020b). Only the area of the anomaly needs to be discretised, and the grid blocks can be larger than in the FD approach (Chew et al., 2008; Malovichko et al., 2017). Both the starting model sensitivity and the computational cost can be reduced by renormalisation and domain-decomposition methods in inversion (Jakobsen and Wu, 2018; Jakobsen et al., 2020c). The integral-equation of Lippmann-Schwinger type can be used in FWI for both single- and multi-parameter problems (Jakobsen et al., 2020c).

Various approaches exist for solving the integral-equation, such as the Born approximation (Hudson and Heritage, 1981; Bleistein et al., 2001; Snieder, 2002), the Born series method (Osnabrugge et al., 2016; Jakobsen et al., 2020c), T-matrix approach (Jakobsen, 2012; Jakobsen and Ursin, 2015; Jakobsen et al., 2020b), and the full-integral equation solution (Jakobsen, 2012; Jakobsen and Ursin, 2015; Jakobsen et al., 2020b). The Born approximation has been the most widely used, as it is quite fast, where only single scattering is accounted for (Snieder, 2002). The Born series is an extension of the Born approximation, as it represents the first term of the series. The Born-Neumann series method has issues of convergence, although this can be negated by preconditioning (see Osnabrugge et al., 2016; Jakobsen et al., 2020c) or using the T-matrix (see Jakobsen, 2012). In this work, frequency-domain seismic modelling is done by computing the exact solution to the Lippmann-Schwinger integral-equation method (see Jakobsen et al., 2020b). Calculating the full integral-equation solution by Gaussian elimination give very accurate results, although at the cost of memory-dependency and computational complexity (Jakobsen and Wu, 2018; Jakobsen et al., 2020a).

3.2 Integral Equation Approach

The general elastodynamic wave equation for an arbitrary anisotropic media in the frequency domain is given as (Schleicher et al., 2001; Snieder, 2002; Červený, 2005; Jakobsen et al., 2020b):

$$[C_{ijkl}(\mathbf{x})u_{k,l}(\mathbf{x})]_{,j} + \rho(\mathbf{x})\omega^2 u_i(\mathbf{x}) = -f_i(\mathbf{x}), \tag{3.1}$$

where the position is given by $\mathbf{x} = x_i = (x_1, x_2, x_3)$, the displacement gradient is given by $u_{k,l}(\mathbf{x}) = \frac{\partial u_k}{\partial x_l}(\mathbf{x})$, the stiffness tensor is denoted by $C_{ijkl}(\mathbf{x})$, the mass density is denoted by $\rho(\mathbf{x})$, the angular frequency is denoted by ω, the source term is denoted by $f_i(\mathbf{x})$ and the components are given as $i, j, k, l \in \{1, 2, 3\}$. The elastic parameters C_{ijkl} satisfy the symmetry relations $C_{ijkl} = C_{jikl} = C_{ijlk} = C_{klij}$ (Schleicher et al., 2001).

It is assumed that $u_i(\mathbf{x})$ is proportional to $e^{i\omega t}$ and that the medium is unbounded and the wavefield approaches zero at infinity (Jakobsen et al., 2020b). The wavefield is only calculated inside the scattering domain denoted Ω, where the scattering potential is nonzero (Jakobsen and Ursin, 2015). As many of the variables depend on ω, e.g. $u_i(\mathbf{x}, \omega)$ and $f_i(\mathbf{x}, \omega)$, the angular frequency ω will be omitted in symbols in future equations for simplicity.

The solution to Eq. (3.1), shown in Eq. (3.2), is a point-source Green's function (Gubernatis et al., 1977; Červený, 2005; Madariaga, 2007).

$$u_i(\mathbf{x}) = \int d\mathbf{x}' g_{ij}(\mathbf{x}, \mathbf{x}') f_j(\mathbf{x}), \tag{3.2}$$

where the Green's function $g_{ij}(\mathbf{x}, \mathbf{x}')$ is defined by (Schleicher et al., 2001; Červený, 2005;

Jakobsen et al., 2020b)

$$[C_{ijkl}g_{kn,l}]_{,j} + \rho(\mathbf{x})\omega^2 g_{in} = -\delta_{in}\delta(\mathbf{x}-\mathbf{x}'). \tag{3.3}$$

Here, δ_{in} is the Kronecker delta and $\delta(\mathbf{x}-\mathbf{x}')$ is the Dirac delta function (Červený, 2005). The position $\mathbf{x}'$ represents a point in the scattering domain Ω. The Green's function, $\mathbf{g}$, is useful for inversion and can be calculated by analytical formulae (Jakobsen et al., 2020b), which is discussed later in this section.

In order to describe scattering of elastic waves, it is necessary to define a reference medium and a perturbation of the medium. Illustrations of different media are presented in Fig. 3.1, where the reference media are shown in Figs. 3.1b and 3.1c, and actual medium is shown in Fig. 3.1a. The unperturbed wave propagates through the background medium, while the perturbation acts as a secondary source that generates scattered waves (Snieder, 2002). Scattering integrals contain both scattering from perturbation in the medium and scattering from erroneousness (Červený, 2005).

Both stiffness and mass density can be decomposed to a sum of the reference, $\mathbf{C}^{(0)}$ and $\rho^{(0)}$, and perturbation fields, $\Delta\mathbf{C}$ and $\Delta\rho$. Thus,

$$C_{ijkl}(\mathbf{x}) = C^{(0)}_{ijkl}(\mathbf{x}) + \Delta C_{ijkl}(\mathbf{x}), \tag{3.4}$$

and

$$\rho(\mathbf{x}) = \rho^{(0)}(\mathbf{x}) + \Delta\rho(\mathbf{x}). \tag{3.5}$$

The extended theory for perturbation in both stiffness and mass density is given in Jakobsen et al. (2020b). In this thesis, the mass density is fixed, $\Delta\rho(\mathbf{x}) = 0$, as fracture-induced anisotropy is considered. This is reasonable, as the effective mass density is to a very small extent affected by fractures (see Jakobsen and Pilskog, 2016). Consequently, $\mathbf{C}(\mathbf{x}) = \mathbf{C}^{(0)}(\mathbf{x}) + \Delta\mathbf{C}(\mathbf{x})$, and $\rho(\mathbf{x}) = \rho^{(0)}(\mathbf{x})$.

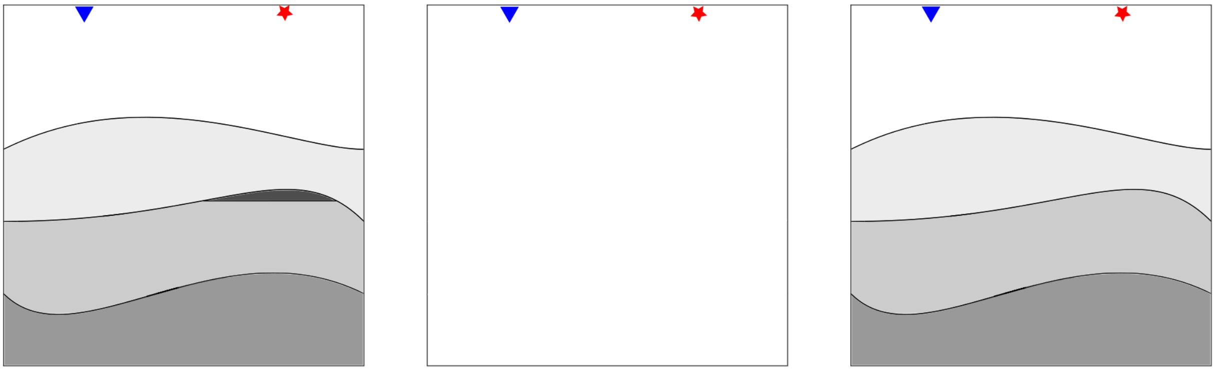
(a) Actual medium **(b)** Reference medium 1 **(c)** Reference medium 2

Figure 3.1: Illustration of an actual medium with an area of perturbation in dark grey (3.1a) and two different reference media (3.1b, 3.1c). The Green's function of the reference medium can either be calculated for a homogeneous medium (middle), or a heterogeneous medium (right). The symbols at the top are: source (red $\star$) and receiver (blue $\bigtriangledown$).

Following the well-known derivation (see Snieder, 2002; Červený, 2005; Jakobsen et al., 2020b), by using Eqs. (3.4) and (3.5), in Eq. (3.1), yields

$$\left[\left(C^{(0)}_{ijkl}(\mathbf{x}) + \Delta C_{ijkl}(\mathbf{x})\right) u_{k,l}(\mathbf{x})\right]_{,j} + \rho^{(0)}(\mathbf{x})\omega^2 u_i(\mathbf{x}) = -f_i(\mathbf{x}). \tag{3.6}$$

Moving the perturbed stiffness tensor $\Delta C_{ijkl}(\mathbf{x})$ to the right side in Eq. (3.6) and treating it as a source term leads to the expression in Eq. (3.7).

$$\left[C^{(0)}_{ijkl}(\mathbf{x}) u_{k,l}(\mathbf{x})\right]_{,j} + \rho^{(0)}(\mathbf{x})\omega^2 u_i(\mathbf{x}) = -f_i(\mathbf{x}) - \left[\Delta C_{ijkl}(\mathbf{x}) u_{k,l}(\mathbf{x})\right]_{,j}. \tag{3.7}$$

It can be shown that the total wavefield, $u_i(\mathbf{x})$, can be represented by the Green's function, by using the representation theorem (see Snieder, 2002; Červený, 2005). Both terms on the right hand side in Eq. (3.7) can be treated as source terms. By introducing a Green's function as defined in Eq. (3.3), a solution to Eq. (3.7) can be written similarly to Eq. (3.2). Thus,

$$u_i(\mathbf{x}) = \int d\mathbf{x}' g^{(0)}_{ij}(\mathbf{x}, \mathbf{x}') f_j(\mathbf{x}') + \int d\mathbf{x}' g^{(0)}_{ij}(\mathbf{x}, \mathbf{x}') \left[\Delta C_{ijkl}(\mathbf{x}') u_{k,l}(\mathbf{x}')\right]_{,j'}. \tag{3.8}$$

It should be noted that the integrals are evaluated over the area where stiffness perturbations are non-zero. Changing the arbitrary components (subscripts) by $i \to j, j \to k, k \to l, l \to m$ in the rightmost term in Eq. (3.8), and writing the reference wavefield, $u^{(0)}_i$, separately, yields

$$u_i(\mathbf{x}) = u_i^{(0)}(\mathbf{x}) + \int d\mathbf{x}' g_{ij}^{(0)}(\mathbf{x}, \mathbf{x}') \left[\Delta C_{jklm}(\mathbf{x}') u_{l,m}(\mathbf{x}')\right]_{,k'} , \tag{3.9}$$

where the reference wavefield is given by

$$u_i^{(0)}(\mathbf{x}) = \int d\mathbf{x}' g_{ij}^{(0)}(\mathbf{x}, \mathbf{x}') f_j(\mathbf{x}'). \tag{3.10}$$

Applying the product rule for derivation on the integral in Eq. (3.9), letting $a = g_{ij}^{(0)}(\mathbf{x}, \mathbf{x}')$ and $b' = \left[\Delta C_{jklm}(\mathbf{x}') u_{l,m}(\mathbf{x}')\right]_{,k'}$, yields

$$\int (a'b + ab') = \int (ab)' \ , \ \lim_{x \to \infty} \int_{-x}^{+x} (ab)' = 0 \tag{3.11}$$

$$\int (a'b + ab') = 0 \Rightarrow \int ab' = -\int a'b \ , \tag{3.12}$$

assuming that the wavefield approaches zero at infinity.

By the radiation condition (Madariaga, 2007) the wavefield (integral) in Eqs. (3.9) and (3.11), converges to zero at infinity. Consequently, the derivative can be moved from the stiffness perturbation, ΔC_{jklm}, to the Green's function, $g_{ij}^{(0)}$. Eq. (3.12) can then be written explicitly with a, b inserted, as

$$\int g_{ij}^{(0)}(\mathbf{x}, \mathbf{x}') \left[\Delta C_{jklm}(\mathbf{x}') u_{l,m}(\mathbf{x}')\right]_{,k'} = -\int g_{ij,k'}^{(0)}(\mathbf{x}, \mathbf{x}') \Delta C_{jklm}(\mathbf{x}') u_{l,m}(\mathbf{x}'). \tag{3.13}$$

Using the symmetry of the strain tensor, $\varepsilon_{lm} = \frac{1}{2}(u_{l,m} + u_{m,l})$, and replacing $u_{l,m}$ with ε_{lm} in Eq. (3.9), yields:

$$u_i(\mathbf{x}) = u_i^{(0)}(\mathbf{x}) - \int d\mathbf{x}' g_{ij,k'}^{(0)}(\mathbf{x}, \mathbf{x}') \Delta C_{jklm}(\mathbf{x}') \varepsilon_{lm}(\mathbf{x}'), \tag{3.14}$$

Due to the symmetric tensors, abbreviated subscripts are preferred. To express the Green's function, $g_{ij,k'}$, accordingly a third-rank Green's tensor, $M_{ijk}^{(0)}$, is introduced. It is defined by (Jakobsen et al., 2003a; Jakobsen and Hudson, 2003; Jakobsen et al., 2020b):

$$M_{ijk}^{(0)}(\mathbf{x}, \mathbf{x}') = -\frac{1}{2}\left[g_{ij,k'}^{(0)}(\mathbf{x}, \mathbf{x}') + g_{ik,j'}^{(0)}(\mathbf{x}, \mathbf{x}')\right] . \tag{3.15}$$

Replacing $g_{ij,k'}^{(0)}(\mathbf{x}, \mathbf{x}')$ in Eq. (3.14) with $M_{ijk}^{(0)}(\mathbf{x}, \mathbf{x}')$ in Eq. (3.15), yields the final expression of the integral equation for the wavefield:

$$u_i(\mathbf{x}) = u_i^{(0)}(\mathbf{x}) + \int d\mathbf{x}' M_{ijk}^{(0)}(\mathbf{x}, \mathbf{x}') \Delta C_{jklm}(\mathbf{x}') \varepsilon_{lm}(\mathbf{x}'). \tag{3.16}$$

The explanation behind the result in Eq. (3.16) is that all tensors can be decomposed into a symmetric and an anti-symmetric part (Auld, 1990; Pujol, 2003). $M_{ijk}^{(0)}$ in Eq. (3.15) corresponds to the symmetric part of $g_{ij,k'}^{(0)}$. The anti-symmetric part of $g_{ij,k'}^{(0)}$ has no contribution, as it is contracted by multiplication with ΔC_{jklm}, which is symmetric in j and k.

The equation above, Eq. (3.16), is the Lippmann-Schwinger (LS) equation for elastic wave scattering (Snieder, 2002). Spatial differentiation of Eq. (3.16) leads to the LS-equation for the strain field (Jakobsen et al., 2020b). The strain tensor, ε, will satisfy Eq. (3.17).

$$\varepsilon_{ij}(\mathbf{x}) = \varepsilon_{ij}^{(0)}(\mathbf{x}) + \int d\mathbf{x}' \Gamma_{ijkl}^{(0)}(\mathbf{x}, \mathbf{x}') \Delta C_{klmn}(\mathbf{x}') \varepsilon_{mn}(\mathbf{x}'). \tag{3.17}$$

The fourth-rank Green's tensor, $\Gamma_{ijkl}^{(0)}$, is defined by (Jakobsen et al., 2003a, 2020b):

$$\Gamma_{ijkl}^{(0)}(\mathbf{x}, \mathbf{x}') = \frac{1}{4}\left[g_{ij,kl'}^{(0)}(\mathbf{x}, \mathbf{x}') + g_{kj,il'}^{(0)}(\mathbf{x}, \mathbf{x}') + g_{il,kj'}^{(0)}(\mathbf{x}, \mathbf{x}') + g_{kl,ij'}^{(0)}(\mathbf{x}, \mathbf{x}')\right], \tag{3.18}$$

where $\Gamma_{ijkl}^{(0)}(\mathbf{x}, \mathbf{x}')$ represents the ij component of strain at $\mathbf{x}$ to the kl component of stress at $\mathbf{x}'$.

In dynamic effective medium theory, the $M^{(0)}$ and $\Gamma^{(0)}$ tensors can be referred to as modified Green's functions (Jakobsen et al., 2003a, 2020b). Both these tensors depend on the reference Green's function $g_{ij}^{(0)}(\mathbf{x}, \mathbf{x}')$. For an isotropic, homogeneous medium this Green's function is the displacement in the i direction at $\mathbf{x}$ due to a point force in the j direction at $\mathbf{x}'$ (Jakobsen et al., 2003a).

Expressions for the reference Green's tensors are given in Appendix B, where the leading-term Green's function is given in Appendix B.1. The modified Green's tensors, $M^{(0)}$ and $\Gamma^{(0)}$, are given in Appendices B.2 and B.3, respectively.

Reference Green's functions can be calculated either with ray theory (Červený, 2005; Jakobsen et al., 2020b) or numerically (Kirchner and Shapiro, 2001). Green's functions are crucial in complicated heterogeneous media and required for direct iterative non-linear inversion (Jakobsen et al., 2020b). The computation of these Green's functions play a critical role in both the exact solution in Section 3.3, and the non-linear inverse scattering problem in Section 4.2.

The Green's functions have a singularity when the radial distance between two discretised points is very low, $r \leq 1$. This topic was discussed in Lee (2009) and found to be (generally) not integrable. Therefore, this singularity must be approximated. In this work, the singularity of both the strain and M-tensor is set to $\mathbf{0}$ for simplicity. This approximation does not have any impact on the results, as the grid is defined in such a way that the radial distance condition, $r \leq 1$, is never met. For the Γ-tensor, corresponding to the second derivative of the Green's function, Jakobsen et al. (2020b) approximated the singularity by using Eshelby's tensor (Eshelby, 1957). This tensor is described in Appendix A.

3.3 Exact Solution

3.3.1 Abbreviated Subscript Notation

For the symmetric tensors in Eqs. (3.16) and (3.17), the abbreviated subscript notation in Auld (1990) can be used. This notation is simply that the repeated upper case indices run from 1 to 6 (Jakobsen et al., 2020b). Rewriting Eq. (3.16) with abbreviated subscript notation, $jk \to K$ and $lm \to L$, yields

$$u_i(\mathbf{x}) = u_i^{(0)}(\mathbf{x}) + \int d\mathbf{x}' M_{iK}^{(0)}(\mathbf{x}, \mathbf{x}') \Delta C_{KL}(\mathbf{x}') \varepsilon_L(\mathbf{x}'). \tag{3.19}$$

The strain tensor, ε, in Eq. (3.17), can be rewritten with abbreviated subscript notation, by setting the indices $ij \to I$, $kl \to J$ and $mn \to K$. Setting the arbitrary position $\mathbf{x}$ to $\mathbf{x}'$ for consistency, yields the following expression for strain in the scattering point $\mathbf{x}'$:

$$\varepsilon_I(\mathbf{x}') = \varepsilon_I^{(0)}(\mathbf{x}') + \int d\mathbf{x}'' \Gamma_{IJ}^{(0)}(\mathbf{x}', \mathbf{x}'') \Delta C_{JK}(\mathbf{x}'') \varepsilon_K(\mathbf{x}''). \tag{3.20}$$

where $\mathbf{x}''$ is a neighbouring scattering point and $I, J, K, L \in \{1, \ldots, 6\}$.

3.3.2 Discretisation and Implementation

There is a need for a discrete form of the displacement in Eq. (3.19), to fully represent the scattering domain Ω as a grid. Subsequently, the integral can be changed to summation over N grid blocks, in Eq. (3.19), while substituting the positions $\mathbf{x}$ and $\mathbf{x}'$ with r and n, respectively (Jakobsen and Ursin, 2015). To reduce the amount of superscripts and achieve a more compact form; $\tilde{u}_i \equiv u_i^{(0)}$ and $\tilde{M}_{iK} \equiv M_{iK}^{(0)}$ are defined. Thus,

$$u_i^r = \tilde{u}_i^r + \sum_{n=1}^{N} \tilde{M}_{iK}^{rn} \delta C_{KL}^n \varepsilon_L^n \delta v^n, \tag{3.21}$$

where δv^n denotes the volume of the grid block in the position $\mathbf{x_n}$. The receiver index is set to $r \in \{1, \ldots, N_r\}$, where N_r is the total number of receivers.

It should be noted that the upper indices (superscripts) refers to positional indices, instead of power as in mathematics. For example, u_i^r refers to the wavefield in the receiver of index r, rather than the wavefield of power r.

The direct wavefield, $u_i^{(0)}$, in Eq. (3.10) can be written in discrete form as:

$$\tilde{u}_i^r = \sum_{n=1}^{N} \tilde{G}_{ij}^{rn} f_j^n, \tag{3.22}$$

where $\tilde{u}_i \equiv u_i^{(0)}$ and $\tilde{G}_{ij} \equiv G_{ij}^{(0)}$, to reduce the number of superscripts.

The source term, $\mathbf{f}$, is dependent on the source pulse s_ω with angular frequency ω and the source polarisation vector $\mathbf{s}$. This vector can represent either a vertical source, $\mathbf{s} = [0, 0, 1]$, or an explosive source, $\mathbf{s} = [1, 1, 1]$. A general source term is then given by $\mathbf{f} = s_\omega \mathbf{s}$.

The integral in Eq. (3.20) can be rewritten as a sum, where the arbitrary positions are replaced by $\mathbf{x}' \to m$ and $\mathbf{x}'' \to n$. Similarly as above, $\tilde{\Gamma}_{IJ} \equiv \Gamma_{IJ}^{(0)}$ and $\tilde{\varepsilon}_I \equiv \varepsilon_I^{(0)}$ are introduced, to get a more compact form of the expression. Then, a discrete form of Eq. (3.20) is given by Eq. (3.23) as

$$\varepsilon_I^m = \tilde{\varepsilon}_I^m + \sum_{n=1}^{N} \tilde{\Gamma}_{IJ}^{mn} \Delta C_{JK}^n \varepsilon_K^n \delta v^n, \tag{3.23}$$

where $m \in \{1, \ldots, N\}$.

It should be noted that each grid block has a centroid defined by: $r = \mathbf{x_r}$ $n = \mathbf{x_n}$, and $m = \mathbf{x_m}$. Each centroid $\mathbf{x_n}$ has a volume δv^n and should be chosen to be small compared to the dominant wavelength (Jakobsen and Ursin, 2015). This grid block volume is assumed to be constant for all grid blocks, leading to $\delta v \equiv \delta v^n$.

Defining a scattering potential, $\mathbf{V}$, by using the Kronecker delta. The Kronecker delta is given in Eq. (A.13) and only gives a contribution when the indices are equal. Thus, the scattering potential is given in Eq. (3.24) as

$$V_{JK}^{mn} \equiv \Delta C_{JK}^n \frac{\delta_{mn}}{\delta v}, \tag{3.24}$$

which will only give a contribution when $m = n$, and cancel the grid volume in Eq. (3.23).

Inserting Eq. (3.24) into Eq. (3.23) and introducing another arbitrary point so that $m \rightarrow n$ and $n \rightarrow p$ in the summation, leads to

$$\varepsilon_I^m = \tilde{\varepsilon}_I^m + \tilde{\Gamma}_{IJ}^{mn} V_{JK}^{np} \varepsilon_K^p, \tag{3.25}$$

where Einstein's summation convention (Einstein, 1916) was used to remove the summation.

Introducing the super-indices (combination counters) β, γ, δ, by letting ${}_I^m \rightarrow \beta$, ${}_J^n \rightarrow \gamma$ and ${}_K^p \rightarrow \delta$. These indices have values equal to $\beta, \gamma, \delta \in \{1, \ldots, 6N\}$. Because there are only lower indices, the reference (background) field can again be denoted by ${}^{(0)}$. The new expression of Eq. (3.25), with super-indices is

$$\varepsilon_\beta = \varepsilon_\beta^{(0)} + \Gamma_{\beta\gamma}^{(0)} V_{\gamma\delta} \varepsilon_\delta. \tag{3.26}$$

Writing Eqs. (3.19) and (3.26) in matrix representation form, where Eq. (3.24) was inserted for ΔC, yields

$$u = u^{(0)} + M^{(0)} V \varepsilon, \tag{3.27}$$

and

$$\varepsilon = \varepsilon^{(0)} + \Gamma^{(0)} V \varepsilon. \tag{3.28}$$

Eq. (3.28) is an integral-equation of the LS-type for the strain, ε. Interested readers should note that in mathematics, this integral corresponds to a Fredholm integral-equation of type II. Both $M^{(0)}$ and $\Gamma^{(0)}$ can be viewed as modified Green's function by the same terminology as in dynamic effective medium theory (Jakobsen et al., 2020b).

Eq. (3.27) can be solved by simply knowing the strain, ε. To find the strain from the source to the scatterers, in Eq. (3.28), the strain within the scattering domain Ω needs to be known. Solving Eq. (3.28) for $\varepsilon^{(0)}$ yields the following matrix equation

$$\varepsilon^{(0)} = \varepsilon - \Gamma^{(0)} V \varepsilon \Leftrightarrow \varepsilon^{(0)} = \left[I - \Gamma^{(0)} V\right] \varepsilon, \tag{3.29}$$

where I is the identity matrix of dimension $6N \times 6N$.

Solving Eq. (3.29) for ε, leads to the final expression for the strain tensor:

$$\varepsilon = \left[I - \Gamma^{(0)} V\right]^{-1} \varepsilon^{(0)}, \tag{3.30}$$

which is independent of the source-receiver configuration.

Eq. (3.30) is a well-posed problem of computational complexity $O(N^3)$ (Jakobsen, 2012). Commonly, this problem is solved with Gaussian elimination by matrix inversion (Jakobsen et al., 2020b). This method has been known for quite a while to be inefficient and not optimal (Strassen, 1969). Calculating the exact solution of Eq. (3.30) by Gaussian elimination, is demanding in terms of computational time. A more efficient way to solve this problem, is to solve it iteratively. Recent years has seen improvement in iterative methods like the Krylov subspace methods (see Saad and Schultz, 1986; Van der Vorst, 1992; Saad, 2003; Ozmen, 2014; Ozmen et al., 2015). These methods were regarded as outside the scope of this work, although they are important to consider for the purpose of decreasing the computational cost.

3.4 Numerical Results and Discussion

The exact solutions of the LS equations are used to calculate the data of the true models, defined in Sections 3.4.1 and 3.4.2. Eqs. (3.27) and (3.28), are solved for particle displacement and strain, respectively. The data is synonymous to the scattered (perturbed) wavefield on the right-hand side in Eq. (3.27), and is calculated sequentially with respect to frequency. First, the data for the first frequency (3 Hz) is calculated, then for the next frequency (5 Hz), and so forth. The frequencies that are used in this work are 3 Hz, 5 Hz, 7.5 Hz, and 10 Hz, which is the same for all models. Since the data is in the frequency-domain, it consists of complex numbers, and can be difficult to visualise. One approach to view this data, is to look at the real and imaginary parts of the wavefield. Also, these data vectors can be split up into their spatial parts (x, z) to view the horizontal and vertical perturbation at the receivers.

The second derivative of a Gaussian function is called a Ricker wavelet, and is used in synthetic experiments to approximate the seismic source wavelet (Wang, 2015). A source wavelet is a shape or signature of the source used in synthetic experiments, that simulates how the signal would look in a seismic trace (Ikelle and Amundsen, 2005). The central frequency, f_0, is the most energetic frequency, corresponding to the maximum amplitude. Expressions for the time-domain and frequency-domain Ricker wavelets (Ricker, 1953; Wang, 2015) are given in Eq. (3.31) and (3.32).

$$r(\tau) = \left(1 - \frac{1}{2}\omega_p^2\tau^2\right) \exp\left(-\frac{1}{4}\omega_p^2\tau^2\right) \ , \tag{3.31}$$

and

$$R(\omega) = \frac{2\omega^2}{\sqrt{\pi}\omega_p^3} \exp\left(-\frac{\omega^2}{\omega_p^2}\right) \ , \tag{3.32}$$

where τ is the time and ω is the angular frequency. The central angular frequency can be defined as $\omega_p = 2\pi f_0$.

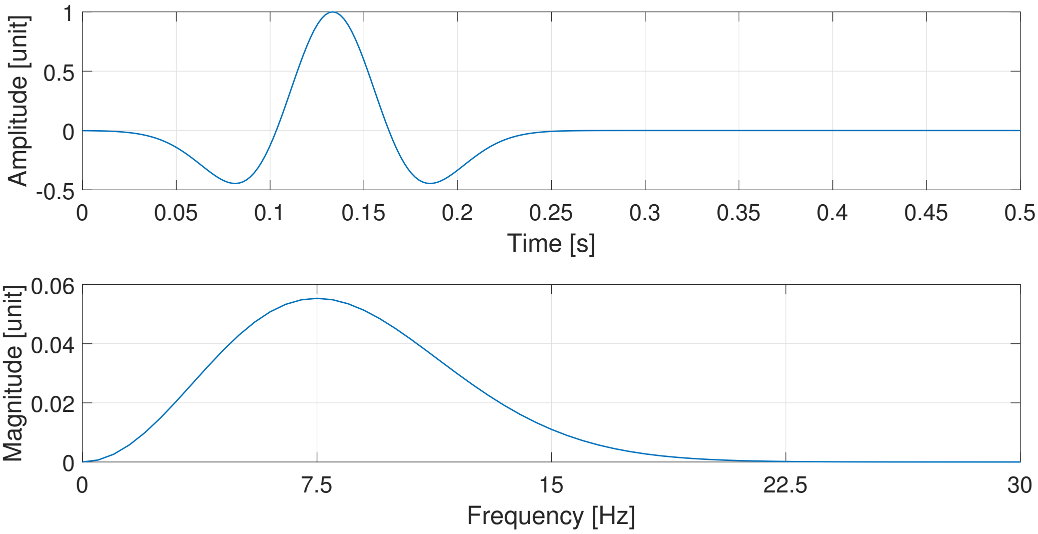

Figure 3.2: Ricker wavelet with a central frequency of 7.5 Hz. Amplitude of the wavelet in the time-domain (upper), and magnitude (amplitude-spectrum) of the frequency-domain wavelet (lower).

In this work, the frequency-domain Ricker wavelet of central (peak) frequency $f_0 = 7.5$ Hz is used. The sampling interval is set to 0.004 s, and the total (recording) time is set to 2 s. The specific central frequency was chosen to be significantly lower than the Nyquist frequency of 125 Hz. Additionally, it is prevalent to use this exact frequency for the Ricker wavelet (e.g. Jakobsen and Ursin, 2015; Jakobsen et al., 2020b; Huang et al., 2020a). The Ricker wavelets, in both the time- and frequency-domain, are presented in Fig. 3.2. In the upper figure, the time-domain wavelet is shown as the typical zero-phase pulse with a maximum amplitude at 0.133 s. The lower figure displays the frequency-domain wavelet, consisting of non-zero energy between 0 Hz and 22.5 Hz, with a maximum amplitude at the central frequency, 7.5 Hz. The source vector, $\mathbf{s}$, is explosive and can be written as [1,0,1] as the medium is 2D. This source vector is important when calculating the background strain.

A data vector shows the particle displacement of the spatial coordinates x_i, at each of the receivers $r = 1, ..., N_r$, for each of the sources $s = 1, ..., N_s$. The total number of points in the data vector is then $3N_rN_s$, as there are three spatial components. However, since the model is in 2D, $x_2 = 0$, and the only contribution is in the x_1 and x_3 directions, respectively. This is ultimately the data that will be used in Chapter 4 and 5, by comparing the computed data with the true (observed) data vector.

To ensure that the numerical experiments are more realistic, it is common to add random (Gaussian) white noise to the data (Jakobsen et al., 2020b). Signal-to-noise ratio (SNR) is a measurement of the impact of noise on the data. Noise in dB is proportional to percentage error, which is given by this formula:

$$\eta_0 = 10^{-\frac{\eta_{\mathrm{dB}}}{20}}, \tag{3.33}$$

where η_0 is called the noise-level, corresponding to the stopping criteria (tolerance) of the inversion for noisy data (Jakobsen and Ursin, 2015). The stopping criteria is only relevant for the inversion, and is introduced in Section 4.2.3.

It is possible to add noise to the frequency components of the data vector (Jakobsen and Ursin, 2015) by:

$$\mathbf{d}^{\mathrm{obs}} = \mathbf{d}^{\mathrm{true}} + \frac{\|\mathbf{d}^{\mathrm{true}}\|}{\sqrt{\mathrm{SNR}}} \cdot \frac{\boldsymbol{\eta}}{\|\boldsymbol{\eta}\|}, \tag{3.34}$$

where $\boldsymbol{\eta}$ is the noise vector of dimension $N_d \times 1$ and $\mathbf{d}^{\mathrm{obs}} \equiv \delta\mathbf{u}^{\mathrm{obs}}$.

Eq. (3.34) corresponds to an equation in Section 4.2.3, allowing for inversion in the more realistic case of noisy data. Note that the η_0 in Eq. (3.33) will be used for the stopping criteria (tolerance) of inversion for noisy data, in Chapters 4 and 5.

The two noise-level cases considered in the models of this work are:

(i) Practically noiseless data, with an SNR of 5000 dB. The noise-level for this experiment is zero, but a tolerance of 10^{-5} is used for the inversion in Chapters 4 and 5.

(ii) Noisy data, with an SNR of 40 dB. The data for this experiment has a noise-level of 0.1% (10^{-2}).

Ultimately, frequency-domain data for the two cases of noise, (i) and (ii), are calculated for the two models referenced in Chapter 2. Data for the syncline model, defined in Section 2.4.1, is different than for the data for the anticline model, defined in 2.4.2. Then, in Chapters 4 and 5, these data vectors are used in the inversion for stiffness perturbation and fracture density, respectively. Only the noiseless data are shown in the following section, as it represents the true (observed) data for each of the models.

3.4.1 Syncline Model

The true, syncline model for the normalised stiffness perturbations given here, as defined in Section 2.4.1 and calculated based on the fracture density model given in Table 2.2. There are four independent (non-zero) stiffness parameters, as the model is 2D VTI. There are 41 receivers and 41 sources located at the top of the model ($z = 0$ m), between 12 m and 972 m on the x-axis. The source and receiver configuration for the syncline model is presented in Fig. 3.3. For this model, the sources and receivers are placed in the same points. The large number of sources is used to get a better illumination for the accuracy of FWI (Zhang et al., 2017).

The true syncline models in Fig. 3.4 are based on the fracture density in the original model, in Fig. 2.5. Therefore, the normalised perturbation, δC_{KL}, in each of the elastic stiffness elements C_{11}, C_{33}, C_{55}, and C_{13} will reflect that. A clear difference between the layers in each of these parameters can be noticed. Although the change in C_{11} is extremely small. Finally, the vector that comprises all these values, from the four independent stiffness perturbation parameters, is called the model vector. This model vector is inverted for in Chapter 4, and the stiffness perturbation figures shown in this section will be compared to the final result of inversion in Section 4.3.1.

Frequency-domain synthetic waveform data for the syncline model are shown in Figs. 3.5 and 3.6, for the real and imaginary components, respectively. Each point corresponds to the particle displacement registered at each of the receivers from each of the sources. The total number of data-points are 5043, and each component contains 1681 values. The data vectors are calculated from the maximum frequency used in modelling, 10 Hz. The real data has a physical relevance, contrary to the imaginary data, as it is quite similar to the amplitude of the wavefield. Both figures show spikes in the wavefield corresponding to the different sources.

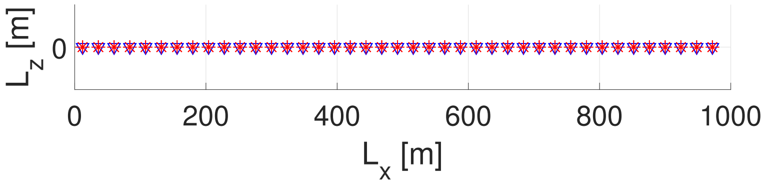

Figure 3.3: Configuration of sources (red stars) and receivers (blue triangles) for the syncline model. The distance between both sources and receivers is 24 m.

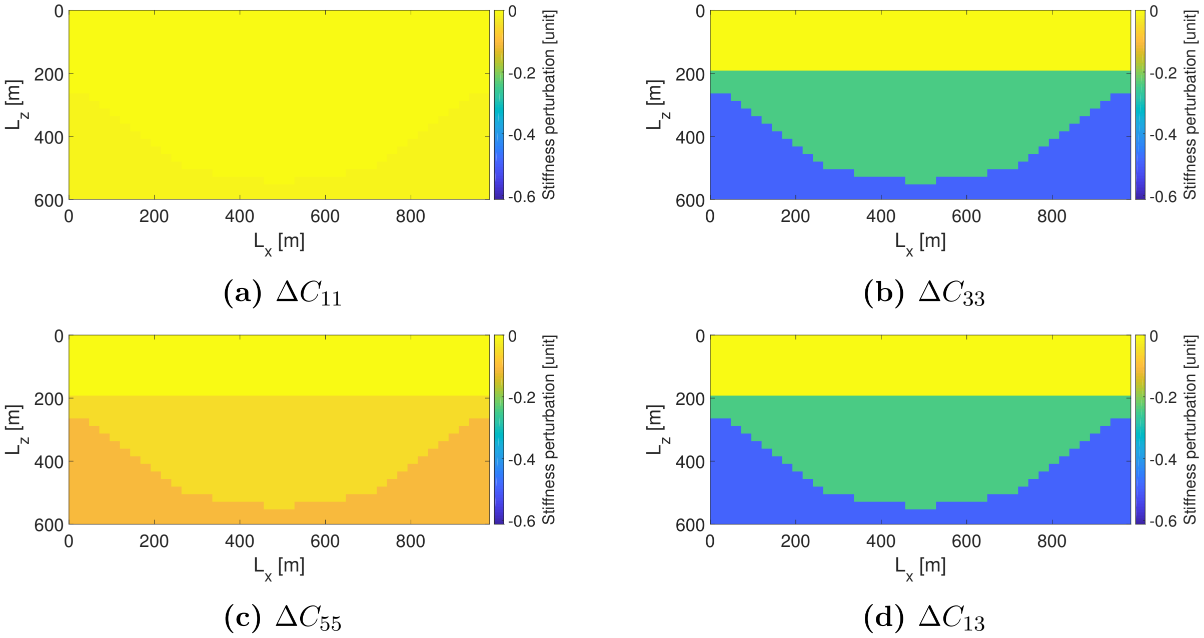

(a) ΔC_{11} **(b)** ΔC_{33}

(c) ΔC_{55} **(d)** ΔC_{13}

Figure 3.4: Normalised stiffness perturbation in each of the elastic parameters of a 2D VTI medium, for the syncline model. The colour map is the same for all parameters.

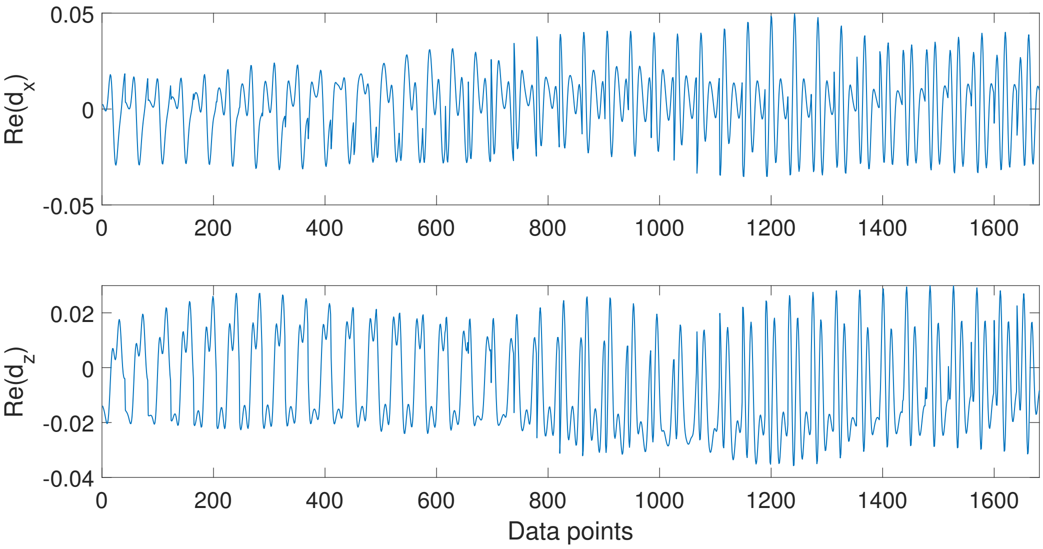

Figure 3.5: Real part of the synthetic (normalised) waveform data, corresponding to the true syncline model. The data vector is separated into the horizontal (upper), d_x, and vertical (lower), d_z, components of the particle displacement.

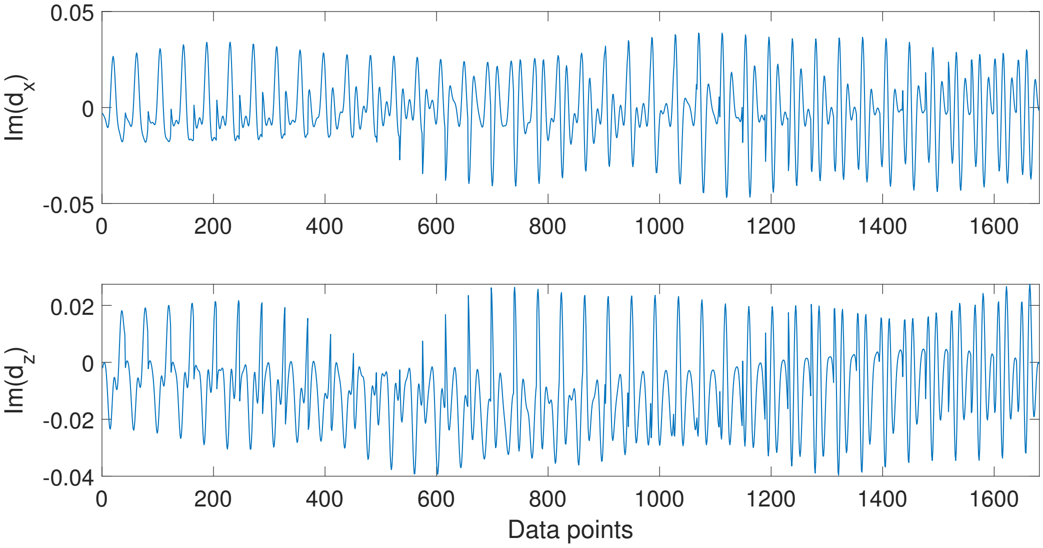

Figure 3.6: Imaginary part of the synthetic (normalised) waveform data, corresponding to the true syncline model. The data vector is separated into the horizontal (upper), d_x, and vertical (lower), d_z, components of the particle displacement.

3.4.2 Anticline Model

Similarly to above, the anticline model for normalised stiffness perturbations was defined in Section 2.4.2. Values used in the computation of these models, are from Table 2.3, and depend on the true fracture density model of Fig. 2.7.

A total number of 41 receivers and 11 sources are evenly distributed at the surface ($z = 0$ m), between 12 m and 972 m on the x-axis. Using one source per four receivers is more realistic, although it gives a worse illumination. In Fig. 3.7, the source and receiver configuration for the syncline model is presented, where one source is used per receiver.

The four independent stiffness parameters, for the 2D anticline model, are shown in Fig. 3.8. Fig. 3.8a, for C_{11}, show no change in stiffness perturbation due to fractures. There is a slight difference between each layer in Fig. 3.8c, for C_{55}. Figs. 3.8b and 3.8d, for C_{33} and C_{13}, show a similarity which is expected according to the discussion in Section 2.4.2. It is evident that there is a moderate contrast between the layers.

Synthetic frequency-domain waveform data are displayed in Figs. 3.9 and 3.10. The data were calculated using sources with a frequency of 10 Hz. Each component (x, z) contain 451 data points due to the number of sources and receivers. Most notably, both the real and imaginary vector differ compared to the other model, as expected. This difference is due to the model parameters being set up differently, in addition to the less symmetric model. These vectors are set up the same as in the previous section, although the number of points is lower due to fewer sources.

Ultimately, the data vectors presented in this chapter, Chapter 3, are compared to the computed models in Chapter 4.

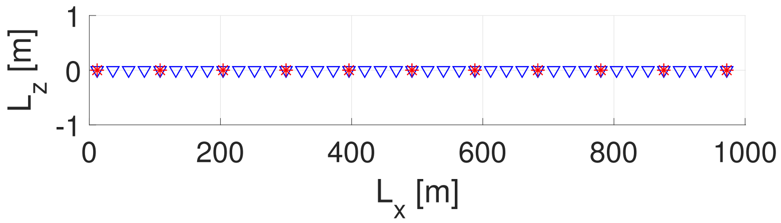

Figure 3.7: Configuration of sources (red stars) and receivers (blue triangles) for the anticline model. The distance between each receiver is 24 m, while for each source the distance is 96 m.

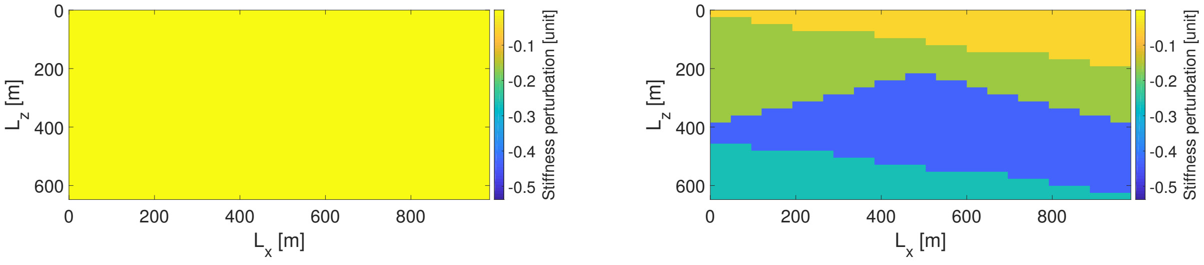

(a) ΔC_{11}

(b) ΔC_{33}

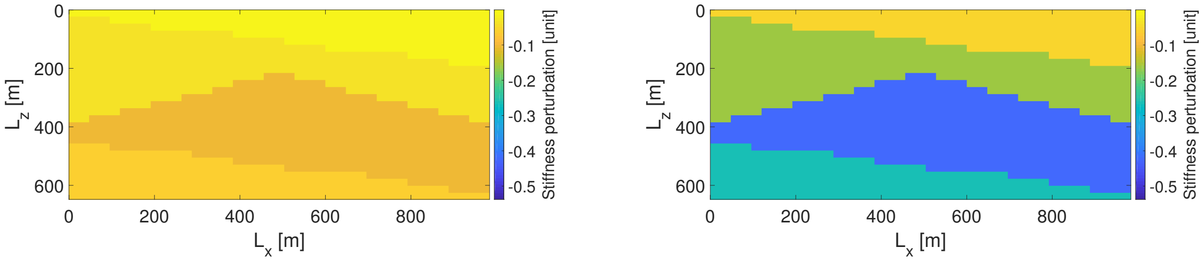

(c) ΔC_{55}

(d) ΔC_{13}

Figure 3.8: Normalised stiffness perturbation in each of the elastic parameters of a 2D VTI medium, for the anticline model. The colour map is the same for all parameters.

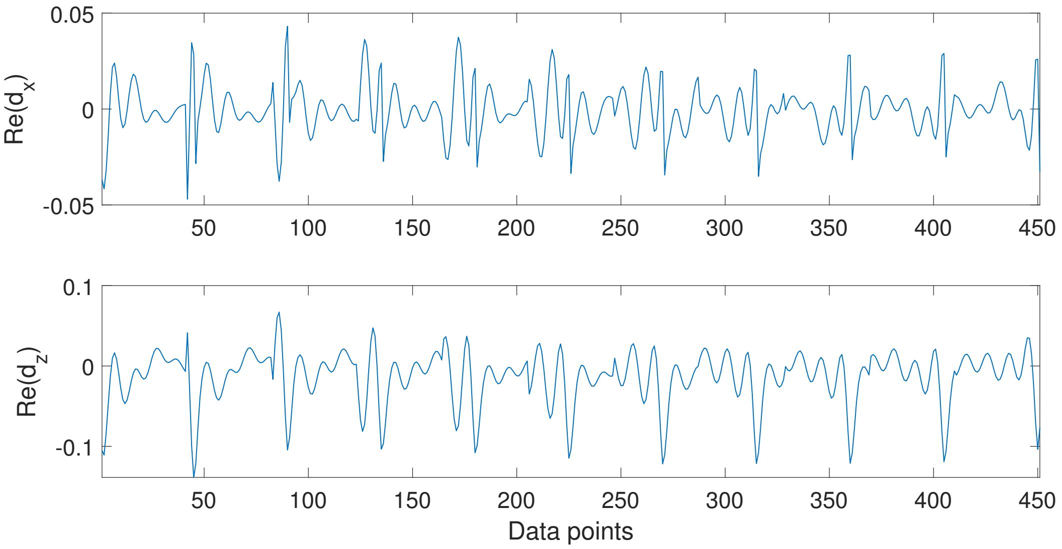

Figure 3.9: Real part of the synthetic (normalised) waveform data, corresponding to the true anticline model. The data vector is separated into the horizontal (upper), d_x, and vertical (lower), d_z, components of the particle displacement.

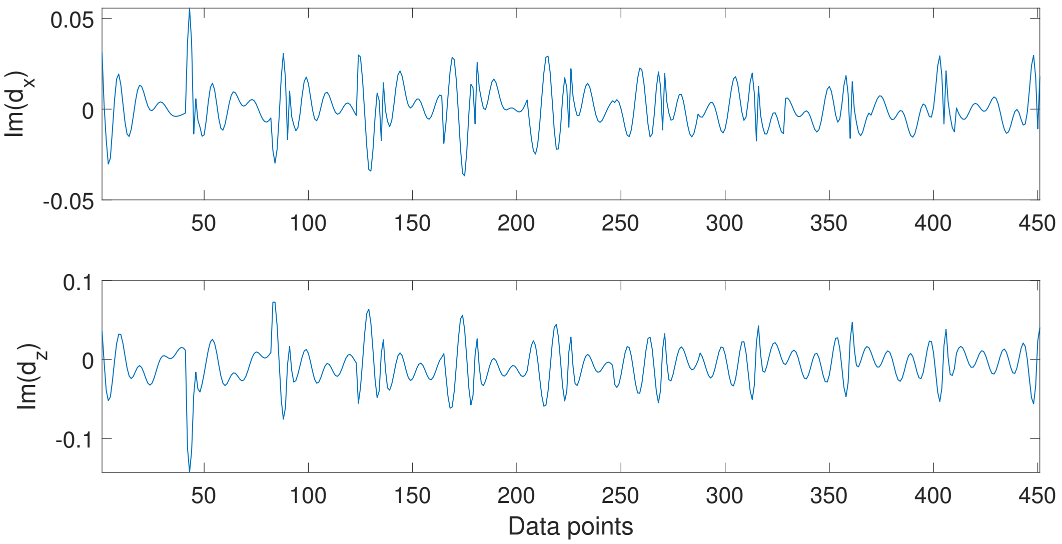

Figure 3.10: Imaginary part of the synthetic (normalised) waveform data, corresponding to the true anticline model. The data vector is separated into the horizontal (upper), d_x, and vertical (lower), d_z, components of the particle displacement.

Chapter 4

Seismic Waveform Inversion

The non-linear inverse scattering problem, based on the already established forward modelling theory, is presented and solved in this chapter. First, the general concepts of inversion are briefly explained. Then, the distorted Born iterative (DBI) inversion method is presented, and its implementation details are provided. The least-squares solution is given with a regularisation term, as well as useful equations for the inversion scheme. Some notes on the regularisation parameter are presented, and an algorithm for implementing the inversion scheme. Finally, numerical results are presented for the two models referenced in previous chapters.

4.1 General Inversion Theory

4.1.1 Linear Inversion Theory

In forward modelling, an exact solution exists if the modelling parameters are known. The forward modelling problem for a linear system of equations can be written as (Constable et al., 1987; Zhdanov, 2015; Aster et al., 2018)

$$\mathbf{d} = \mathbf{A}\mathbf{m}, \tag{4.1}$$

with the inverse problem being

$$\mathbf{m} = \mathbf{A}^{-1}\mathbf{d}. \tag{4.2}$$

Here, $\mathbf{d}$ is the data, $\mathbf{m}$ is the model, and $\mathbf{A}$ is the (linear) forward operator. However, the matrix $\mathbf{A}$ is generally not invertible. The inverse problem is to estimate a set of model parameters, $\mathbf{m}$, from the recorded data, $\mathbf{d}$ (Pratt, 1999). There are several reasons why inverse problems are complicated. Aster et al. (2018) describes three main issues: the existence of a solution, the uniqueness of a solution, and the solution process instability. Inverse problems are inherently ill-posed rather than well-posed (Hadamard, 1952; Zhdanov, 2015), when the solution is non-unique or the inversion process becomes unstable (Aster et al., 2018). An ill-posed problem can also be described as an under-determined problem, where there are more unknowns than equations (Menke, 2012; Zhdanov, 2015). Furthermore, predicted values cannot be equal to observed values due to measurement uncertainties (noise) and modelisation imperfections (Tarantola, 2005).

As the forward problem is under-determined and ill-posed, Eq. (4.2) cannot solve Eq. (4.1). The least-squares method can be employed, as the least-squares solution minimises the sum of the errors squared (Gubbins, 2004). Eq. (4.1) can be represented for an under-determined problem as (Zhdanov, 2015)

$$\mathbf{A}^T\mathbf{A}\mathbf{m} = \mathbf{A}^T\mathbf{d}, \tag{4.3}$$

where $\mathbf{A}^T$ denotes the transpose of $\mathbf{A}$.

The least-squares solution of Eqs. (4.1) and (4.3) is (Gubbins, 2004)

$$\mathbf{m} = \left(\mathbf{A}^T\mathbf{A}\right)^{-1}\mathbf{A}^T\mathbf{d}. \tag{4.4}$$

The least-squares methods are popular for solving inverse problems because they lead to the easiest computations (Menke, 2012). The linear least-squares problem is a discrete ill-posed problem if the singular values of $\mathbf{A}$ go to zero, and the ratio between the maximum and minimum non-zero singular values is large (Hansen, 1994). The robustness is a drawback, as the methods have a keen sensitivity to a small number of outliers in a data set (Tarantola, 2005). A widely used solution to this problem is the Tikhonov regularisation.

In Tikhonov regularisation, the goal is to minimise the norm of the model, $\min \|\mathbf{m}\|_2$, to find a good solution to the ill-posed problem (Aster et al., 2018). One option is to express this problem as a regularised least-squares problem. An objective function for the least-squares problem is given by (Menke, 2012; Jakobsen and Ursin, 2015; Aster et al., 2018)

$$E(\delta\mathbf{m}) = \|\mathbf{d} - \mathbf{A}\delta\mathbf{m}\|^2 + \lambda^2\|\delta\mathbf{m}\|^2, \tag{4.5}$$

where $\delta\mathbf{m} = \mathbf{m} - \mathbf{m}_0$, and λ is the regularisation parameter described in Section 4.2.4.

Subsequently, the solution to the objective function in Eq. (4.5) is (Jakobsen and Ursin, 2015; Aster et al., 2018):

$$\mathbf{m} = \mathbf{m}_0 + \left[\mathbf{A}^T\mathbf{A} + \lambda^2\mathbf{I}\right]^{-1}\mathbf{A}^T\delta\mathbf{d}, \tag{4.6}$$

where $\mathbf{I}$ is the identity matrix, and the data residuals, $\delta\mathbf{d}$, is given as (Jakobsen and Ursin, 2015)

$$\delta\mathbf{d} = \mathbf{d} - \mathbf{A}\mathbf{m}_0. \tag{4.7}$$

The data residuals, $\delta\mathbf{d}$, in Eq. 4.7 will converge to zero when the model converges to the true model, for an initial model that is close enough to the true model (Jakobsen and Ursin, 2015). The model, $\mathbf{m}$, in Eq. (4.6) can be computed for a given operator, $\mathbf{A}$, and data, $\mathbf{d}$. This is further discussed and shown in Section 4.2.3.

4.1.2 Non-Linear Inversion Theory

The non-linear forward modelling problem can be written as (Tarantola, 2005; Zhdanov, 2015; Aster et al., 2018)

$$\mathbf{d} = \mathbf{A}(\mathbf{m}), \tag{4.8}$$

where $\mathbf{A}$ is a non-linear operator that can be found iteratively.

Non-linear inversion indicates that the forward modelling problem in Eq. (4.8) is a non-linear system of equations (Aster et al., 2018). The need for non-linear inversion is due to the computed seismic data, in Eq. (4.8), being non-linear functions of the model parameters (Tarantola, 2005). Additionally, the introduction of more model parameters lead to an increased non-linearity (Jakobsen et al., 2020b).

The most-used method for inverting non-linear problems is linearisation, which approximates the non-linear problem with linear equations and methods (Gubbins, 2004). To solve the linearised non-linear problem; a starting model is chosen, then the residuals of the data are computed, and the minimal change in the model reducing the residuals are found (Gubbins, 2004). One example of solving the non-linear least-squares problem, is the Gauss-Newton method (see Pratt et al., 1998; Richter, 2016; Aster et al., 2018; Jakobsen et al., 2020b). More details on the inversion method implementation is given in the next section, Section 4.2.

4.2 Non-linear Inverse Scattering Problem

4.2.1 Distorted Born Iterative Inversion Method

The non-linear, inverse scattering problem is the problem of determining the material properties of the Earth, e.g. elastic stiffness, from seismic reflection data (Weglein et al., 2003). It can be reduced to a series of linear inverse problems by using the distorted Born iterative (DBI) method, which is Gauss-Newton consistent (Jakobsen et al., 2020b). It has been shown that the DBI method converges faster than the Born Iterative (BI) method (Chew and Wang, 1990). The DBI inversion is done by first inverting for the variation in the updated scattering potential $\delta\mathbf{V}^{(i)}$ of iteration i, due to a variation, $\delta\mathbf{m}^{(i+1)}$, in the model parameter, $\mathbf{m}^{(i+1)}$ (Huang et al., 2020a). Then, the strain field, $\boldsymbol{\varepsilon}^{(i)}$, is updated the using the Green's tensor $\boldsymbol{\Gamma}^{(0)}$ (Jakobsen et al., 2020b). The distorted Born approximation is defined by (Chew and Wang, 1990; Hesford and Chew, 2010; Jakobsen and Ursin, 2015; Jakobsen and Wu, 2018; Huang et al., 2020a; Jakobsen et al., 2020b) as

$$\delta\mathbf{u}^{(i)} = \mathbf{M}^{(i)}\delta\mathbf{V}^{(i)}\boldsymbol{\varepsilon}^{(i)}, \tag{4.9}$$

where the displacement vector is

$$\delta\mathbf{u}^{(i)} = \mathbf{u} - \mathbf{u}^{(i)}, \tag{4.10}$$

and the updated scattering potential is

$$\delta\mathbf{V}^{(i)} = \mathbf{V}^{(i)} - \mathbf{V}^{(i-1)}. \tag{4.11}$$

The scattering potential in the previous iteration, $\mathbf{V}^{(i-1)}$, is assumed to be known and approximately equivalent to the stiffness perturbation, $\Delta\mathbf{C}^{(i-1)}$, by Eq. (3.24). The updated strain field in Eq. (3.28), is then given by

$$\boldsymbol{\varepsilon}^{(i)} = \boldsymbol{\varepsilon}^{(0)} + \boldsymbol{\Gamma}^{(0)}\mathbf{V}^{(i)}\boldsymbol{\varepsilon}^{(i)}, \tag{4.12}$$

with the exact solution given in Eq. (3.30). The fourth-rank Green's tensor, $\boldsymbol{\Gamma}^{(0)}$, can be calculated with Eq. (3.18) and formulas in Appendix B.3.

In an inhomogeneous medium, the modified Green's tensor, $\mathbf{M}^{(i)}$, is updated using the homogeneous background, $\mathbf{M}^{(0)}$. Expressions for calculating the reference third-rank Green's tensor, $\mathbf{M}^{(0)}$, is given in Appendix B.2. The formula for updating $\mathbf{M}^{(i)}$ each iteration, is given as (Huang et al., 2020a)

$$\mathbf{M}^{(i)} = \mathbf{M}^{(0)} + \mathbf{M}^{(i)}\mathbf{V}^{(i)}\boldsymbol{\Gamma}^{(0)}, \tag{4.13}$$

with the exact solution

$$\mathbf{M}^{(i)} = \mathbf{M}^{(0)}\left(\mathbf{I} - \mathbf{V}^{(i)}\boldsymbol{\Gamma}^{(0)}\right)^{-1}. \tag{4.14}$$

Both the modified Green's functions, $\mathbf{M}^{(0)}$ and $\boldsymbol{\Gamma}^{(0)}$, were defined in Section 3.2. Updating the tensors $\boldsymbol{\varepsilon}^{(i)}$ and $\mathbf{M}^{(i)}$ in Eqs. (4.12) and (4.13), respectively, allows for estimating the displacement vector, $\delta\mathbf{u}^{(i)}$, in Eq. (4.9).

4.2.2 Inversion Implementation

In this section, the inversion scheme, in terms of deterministic inversion, based on the Gauss-Newton method, is implemented (Jakobsen et al., 2020b). The Fréchet derivative is continuous (functional) theory and gives the change in the data due to an infinitesimally small change in the model. In this context, the sensitivity matrix can be referred to as the discretised theory of the Fréchet derivative.

Following Jakobsen et al. (2020b), the goal is to calculate the perturbed elastic wavefield with components, j ,at each receiver position, r. The scattered wavefield from Eq. (3.21) is given by

$$\delta u_j^r = \sum_{n=1}^{N} M_{jK}^{rn}\Delta C_{KL}^{n}\varepsilon_L^n\delta v, \tag{4.15}$$

where the index $i \to j$ was changed, to avoid confusion with iteration number i. The expression is evaluated for each grid block's midpoint n, and the total number of grid blocks is N.

As mentioned in Section 3.3.2, it should be noted that the upper indices (superscripts) refers to positional indices, instead of power as in mathematics. For example, δu_j^r refers to the scattered wavefield in the receiver of index r, rather than the scattered wavefield of power r.

The elastic stiffness perturbation tensor, $\Delta\mathbf{C}$, must be decomposed to include the model vector, $\mathbf{m}$. One way to do this is with the B-matrix tensor field (Jakobsen et al., 2017, 2020b) given in Eq. (4.16). A general, anisotropic medium has 21 independent elastic constants and each must be accounted for in the parameter index p of the model, $\mathbf{m}$. Thus,

$$\Delta C_{KL}^{n} = \sum_{p=1}^{21} B_{KL}^{n,p} m^{n,p}, \tag{4.16}$$

where p is the model parameter index corresponding to elastic coefficients in δC^n_{KL}.

For a general VTI medium, there are five symmetric B-matrices, corresponding to each of the independent stiffness parameters in Kelvin notation, as was described in Section 2.2. The model parameter p is related to the matrix indices KL by $1 \to 11$, $2 \to 33$, and so forth. Based on the theory from Jakobsen et al. (2020b), they can be defined as:

$$B^{11} = \begin{bmatrix} 1 & 1 & 0 & 0 & 0 & 0 \\ & 1 & 0 & 0 & 0 & 0 \\ & & 0 & 0 & 0 & 0 \\ & & & 0 & 0 & 0 \\ & & & & 0 & 0 \\ & & & & & 0 \end{bmatrix}, \quad B^{33} = \begin{bmatrix} 0 & 0 & 0 & 0 & 0 & 0 \\ & 0 & 0 & 0 & 0 & 0 \\ & & 1 & 0 & 0 & 0 \\ & & & 0 & 0 & 0 \\ & & & & 0 & 0 \\ & & & & & 0 \end{bmatrix}, \quad B^{55} = \begin{bmatrix} 0 & 0 & 0 & 0 & 0 & 0 \\ & 0 & 0 & 0 & 0 & 0 \\ & & 0 & 0 & 0 & 0 \\ & & & 2 & 0 & 0 \\ & & & & 2 & 0 \\ & & & & & 0 \end{bmatrix}$$

$$B^{66} = \begin{bmatrix} 0 & -2 & 0 & 0 & 0 & 0 \\ & 0 & 0 & 0 & 0 & 0 \\ & & 0 & 0 & 0 & 0 \\ & & & 0 & 0 & 0 \\ & & & & 0 & 0 \\ & & & & & 2 \end{bmatrix}, \qquad B^{13} = \begin{bmatrix} 0 & 0 & 1 & 0 & 0 & 0 \\ & 0 & 1 & 0 & 0 & 0 \\ & & 0 & 0 & 0 & 0 \\ & & & 0 & 0 & 0 \\ & & & & 0 & 0 \\ & & & & & 0 \end{bmatrix}.$$

If the reference elastic stiffness tensor, $C^{(0)}_{KL}$, is non-zero, the Voigt stiffness perturbations, ΔC^n_{KL}, can be normalised in each grid block n by (Jakobsen et al., 2020b)

$$m^{n,p} = \frac{\left(C^n_{KL} - C^{(0)}_{KL}\right)}{C^{(0)}_{KL}}, \tag{4.17}$$

where $\Delta C^n_{KL} = C^n_{KL} - C^{(0)}_{KL}$.

The notation change of $K, L \to p = 1, \ldots, 21$ applies for a general anisotropic elastic stiffness tensor. This means that a combination of K, L is substituted with the model parameter index p, for a given symmetry of the medium. In this work, there are four independent (non-zero) stiffness perturbation parameters as the medium is 2D VTI. Consequently, the four (arbitrary) model parameter indices p can be substituted on the following form: $KL = 11 \to p = 1$, $KL = 33 \to p = 2$, $KL = 55 \to p = 3$, and $KL = 13 \to p = 4$. It should be noted that these parameter indices p could have been selected in another fashion, as they are arbitrary.

The normalisation above, in Eq. (4.17), is an advantage of FWI, ensuring that the model parameters are of approximately the same size (Jakobsen et al., 2020b). Thus, lowering the contrast between the multiple parameters.

Following Jakobsen and Ursin (2015) and Jakobsen et al. (2020b), the model parameters are found using the regularised least-squares solution. Inserting Eq. (4.16) into Eq. (4.15), yields

$$\delta u_j^r = \sum_{n=1}^{N} \sum_{p=1}^{21} M_{jK}^{rn} B_{KL}^{n,p} \varepsilon_L^n m^{n,p} \delta v, \tag{4.18}$$

where $B^{n,p}$ denotes the corresponding B-matrix of model parameter p in grid block n. However, the B-matrix is constant and does not depend on the grid block n, leading to $B_{KL}^{p} = B_{KL}^{n,p}$.

A sensitivity matrix, $\mathbf{J}$, can be defined to represent the tensors in Eq. (4.18). Consequently, the sensitivity matrix in component notation is given as (Jakobsen and Ursin, 2015)

$$J_j^{rn,p} \equiv M_{jK}^{rn} B_{KL}^{p} \varepsilon_L^n \delta v, \tag{4.19}$$

where Einstein's summation convention (Einstein, 1916) is used.

A more precise name for the sensitivity matrix in Eq. (4.19) is sensitivity elements, as it contains more dimensions (indices) than a matrix. In the following expressions, the sensitivity elements are rearranged into a sensitivity matrix, $\mathbf{J}$.

Eq. (4.18) can, by utilising the sensitivity matrix defined in Eq. (4.19), be written as

$$\delta u_j^r = \sum_{p=1}^{21} J_j^{rn,p} m^{n,p}. \tag{4.20}$$

To reduce the number of lower indices, a combination counter α can be introduced by ${}_j^r \rightarrow \alpha$, and runs from 1 to $3N_r$. The introduction of α simplifies Eq. (4.20), and the resulting expression is shown in Eq. (4.21).

$$\delta u_\alpha = \sum_{p=1}^{21} J^{\alpha n,p} m^{n,p}. \tag{4.21}$$

The updated sensitivity matrix, corresponding to Eq. (4.21), is then given by

$$J^{\alpha n,p} = M_K^{\alpha n} B_{KL}^{p} \varepsilon_L^n \delta v. \tag{4.22}$$

To achieve a more compact notation, Eqs. (4.21) and (4.22) can be written symbolically without the indices α, n. Finally, a discretised expression for the scattered wavefield, $\delta\mathbf{u}^{(i)}$, of each iteration, i, in vector form is reached (Jakobsen et al., 2020b) and presented in Eq. (4.23).

$$\delta\mathbf{u}^{(i)} = \sum_{p=1}^{21} \mathbf{J}^{(i,p)}\delta\mathbf{m}^{(i+1,p)}, \tag{4.23}$$

where

$$\mathbf{J}^{(i,p)} = \mathbf{M}^{(i)}\mathbf{B}^{(p)}\boldsymbol{\varepsilon}^{(i)}\delta v. \tag{4.24}$$

Here, $\delta\mathbf{m}^{(i+1,p)} = \mathbf{m}^{(i+1,p)} - \mathbf{m}^{(i,p)}$ is the inverted (normalised) perturbation of parameter p in iteration i.

The dimensions of the vectors and matrices are as follows (Jakobsen et al., 2020b): $\dim\left(\delta\mathbf{u}^{(i)}\right) = N_d \times 1$, $\dim\left(\mathbf{J}^{(i,p)}\right) = N_d \times N$, and $\dim\left(\delta\mathbf{m}^{(i+1,p)}\right) = N \times 1$. For data vectors, $\delta\mathbf{u}^{(i)}$, with more than one source, the total number of points in the data vector is $N_d = 3N_rN_s$, where N_s is the number of sources. Each data point is given by a super-index (combination counter), calculated by Eq. (4.25).

$$\alpha = (i-1)N_rN_s + (s-1)N_r + r, \tag{4.25}$$

where the indices i, s, r denotes the spatial, source and receiver number, respectively.

The elastic stiffness tensor for a 3D VTI medium was discussed in Section 2.2, and given explicitly in Eq. (2.5). Consequently, there are four independent Voigt stiffness parameters in a 2D VTI medium. For each iteration, the data residual wavefield, sensitivity matrix, and model perturbation in Eq. (4.23) is given by (Jakobsen et al., 2020b)

$$\delta\mathbf{u}^{(i)} = \mathbf{J}^{(i)}\delta\mathbf{m}^{(i+1)}, \tag{4.26}$$

where

$$\mathbf{J}^{(i)} = \left[\mathbf{J}^{(i,1)}, \mathbf{J}^{(i,2)}, \mathbf{J}^{(i,3)}, \mathbf{J}^{(i,4)}\right], \tag{4.27}$$

and

$$\delta\mathbf{m}^{(i+1)} = \left[\delta\mathbf{m}^{(i+1,1)}, \delta\mathbf{m}^{(i+1,2)}, \delta\mathbf{m}^{(i+1,3)}, \delta\mathbf{m}^{(i+1,4)}\right]^T. \tag{4.28}$$

Each of the normalised stiffness perturbation parameters ΔC_{11}, ΔC_{33}, ΔC_{55}, and ΔC_{13}, correspond to the model parameters $\delta\mathbf{m}^{(i+1,1)}$, $\delta\mathbf{m}^{(i+1,2)}$, $\delta\mathbf{m}^{(i+1,3)}$, and $\delta\mathbf{m}^{(i+1,3)}$ in Eq. (4.28). The model perturbation vector, $\delta\mathbf{m}^{(i+1)}$, contains a total of $4N$ values, where the stiffness perturbation parameters are organised one after the other.

4.2.3 Regularised Least-Squares Solution

Given the vectors in Eqs. (4.26) - (4.28), a solution to the least-squares problem can be found. The objective function in Eq. (4.5) can be rewritten with the iteration number i as (Jakobsen and Ursin, 2015; Jakobsen and Wu, 2018; Jakobsen et al., 2020b)

$$E(\delta\mathbf{m}^{(i+1)}) = \left\|\delta\mathbf{u}^{(i)}_{\text{obs}} - \mathbf{J}^{(i)}\delta\mathbf{m}^{(i+1)}\right\|^2 + \left(\lambda^{(i)}\right)^2 \left\|\delta\mathbf{m}^{(i+1)}\right\|^2, \tag{4.29}$$

where $\|\|$ denote the L2-norm (length of vector in Euclidean space), and the regularisation parameter, $\lambda^{(i)}$, is further discussed in Section 4.2.4.

A solution for the model vector, $\delta\mathbf{m}^{(i+1)}$, that minimises Eq. (4.29) exists by Eq. (4.6). The expression for updating the model, $\mathbf{m}$, is then given by (Virieux and Operto, 2009; Menke, 2012; Zhdanov, 2015; Jakobsen and Ursin, 2015; Jakobsen et al., 2020b)

$$\mathbf{m}^{(i+1)} = \mathbf{m}^{(i)} + \left[\mathbf{H}^{(i)} + (\lambda^{(i)})^2\mathbf{I}_N\right]^{-1}\mathbf{G}^{(i)}, \tag{4.30}$$

where $\mathbf{I}_N$ is the $N \times N$ identity matrix and $\lambda^{(i)}$ is the regularisation parameter in each iteration. For the first iteration $i = 0$, the initial model (guess), $\mathbf{m}^{(0)}$, is used.

The gradient vector, $\mathbf{G}^{(i)}$, in Eq. (4.30) is given by (Jakobsen and Ursin, 2015; Jakobsen et al., 2020b)

$$\mathbf{G}^{(i)} = \Re\left[(\mathbf{J}^{(i)})^{\dagger}\delta\mathbf{u}^{(i)}\right], \tag{4.31}$$

and the Hessian matrix, $\mathbf{H}^{(i)}$, in Eq. (4.30) is given by (Pratt et al., 1998; Pan et al., 2017; Jakobsen et al., 2020b)

$$\mathbf{H}^{(i)} = \Re\left[(\mathbf{J}^{(i)})^{\dagger}\mathbf{J}^{(i)}\right], \tag{4.32}$$

where $\Re$ denotes the real values of the matrix, and † indicates the Hermitian transpose, which is also referred to as the conjugate transpose.

In each iteration, the updated data residual, $\delta\mathbf{u}^{(i)}$, is given by (Jakobsen and Ursin, 2015; Jakobsen et al., 2020b)

$$\delta\mathbf{u}^{(i)} = \delta\mathbf{u}^{\text{obs}} - \mathbf{J}^{(i)}\mathbf{m}^{(i)}, \tag{4.33}$$

where the synthetic (observed) data, with noise, is given by

$$\delta\mathbf{u}^{\text{obs}} = \mathbf{J}^{\text{true}}\mathbf{m}^{\text{true}} + \boldsymbol{\eta}\ . \tag{4.34}$$

In synthetic experiments, Eq. (4.34) is used to calculate the “observed” synthetic data. For noiseless experiments, the observed data is equal to the predicted data, and these data are calculated by $\mathbf{J}^{\text{true}}\mathbf{m}^{\text{true}}$. Similarly, for noisy synthetic data, there is a contribution of noise in addition to the predicted data. The concept of noisy data was explained in Section 3.4. The theory described in this section can also be used on real data. In the case of real data, both the true model and noise contribution is assumed to be unknown. Real data is represented in the time-domain, while the expressions above are for observed synthetic data, which is in the frequency-domain.

Eq. (4.18) yields the scattered wavefield in each receiver position for one or more sources. Based on the theory in Chapter 3, the seismic source pulse contains more than one frequency. Thus, it is useful to calculate the wavefield sequentially for a set of frequencies (Pratt, 1999). Consequently, the resulting model, $\mathbf{m}$, from the previous frequency, can be used as a starting model for the next frequency. This model is usually closer to the true model, and leads to better inversion results.

When the model, $\mathbf{m}^{(i)}$, in Eq. (4.33) converges to the true model, $\mathbf{m}^{\text{true}}$, the data residuals, $\delta\mathbf{u}^{(i)}$, converges to zero. To validate the convergence of the inversion process, residual data error, ϵ_d, and model error, ϵ_m, are introduced. The residual data error is based on the observed data, $\delta\mathbf{u}^{\text{obs}}$, in Eq. (4.33), while the model error is calculated based on the true model, $\mathbf{m}_{\text{true}}$ (Jakobsen et al., 2020b). Thus, the residual data error is given by

$$\epsilon_d^{(i)} = \frac{||\delta\mathbf{u}^{\text{obs}} - \mathbf{J}^{(i)}\mathbf{m}^{(i)}||}{||\delta\mathbf{u}^{\text{obs}}||}, \tag{4.35}$$

and the model error is given by (Jakobsen et al., 2020b)

$$\epsilon_m^{(i)} = \frac{||\mathbf{m}_{\text{true}} - \mathbf{m}^{(i)}||}{||\mathbf{m}_{\text{true}}||}, \tag{4.36}$$

where $\mathbf{m}^{(i)}$ is the current model, calculated by Eq. (4.30).

The general steps of the inversion scheme, Eqs. (4.30) - (4.36), need to stop when the inversion is considered successful. Normally, the inversion will stop when a chosen tolerance (stopping-criteria) η_0 is met, which in theory means when the data error is lower than the tolerance, $\epsilon_d^{(i)} \leq \eta_0$ (Jakobsen et al., 2020b). This criteria is in accordance to Morozov's discrepancy principle described in Section 4.2.4. The tolerance can be selected arbitrarily, and should be chosen to be as low as possible (Jakobsen et al., 2020b). In the presence of noise, the tolerance is equal to the noise-level defined in Eq. (3.33). The reason for this is that the residual data error will not reach a lower level due to noise.

The main procedure of the DBI inversion scheme, Eqs. (4.30) - (4.36), that was used in this work is presented in Algorithm 2, below Section 4.2.4. It is assumed that an isotropic background stiffness tensor $\mathbf{C}^{(0)}$ is known, to normalise the model parameters in Eq. (4.17). Each frequency used in this inversion scheme, corresponds to the frequencies given in Sections 3.4. In Algorithm 2, the frequency is given as angular frequency, ω, in the outer loop. The minimum frequency used in this work, is 3 Hz, corresponding to an angular frequency of 6π rad/s. For each frequency, observed data, $\delta\mathbf{u}^{\text{obs}}$, is computed, and inversion is performed to find the best fitting model vector, $\mathbf{m}$, of this frequency. Then, this process is repeated for the next frequency, using the resulting model from the last frequency. It should be noted that a different regularisation scheme may be used, as well as a different method of finding the optimum starting regularisation, λ.

4.2.4 Regularisation Parameter

The generalised inverse solution in Eq. (4.4) can become unstable when its values are singular (Aster et al., 2018). It should be noted that a matrix with singular elements is not invertible. The Tikhonov regularisation method, as described in Section 4.1 is used to combat this, and is represented by the regularisation parameter, λ, in Eqs. (4.29) and (4.30). Regularising the least-squares problem with a dynamic regularisation parameter, $\lambda^{(i)}$, is also utilised to reduce the effects of random noise (Jakobsen and Ursin, 2015).

Choosing a too small regularisation, λ, parameter can build unwanted structures, that must be removed by additional iterations (Farquharson and Oldenburg, 2004). The iterative procedure should be ended when the residual data error reaches the set noise level, η_0, by the discrepancy principle (Constable et al., 1987; Jakobsen and Wu, 2018; Jakobsen et al., 2020b).

There exist numerous methods for finding and updating the optimal regularisation parameter (Jakobsen and Ursin, 2015), e.g. the L-curve method (Hansen, 2001), cooling-scheme (Farquharson and Oldenburg, 2004; Jakobsen and Ursin, 2015), and the self-adaptive scheme (Ciric and Qin, 1997; Jakobsen et al., 2020b).

When the residual data error, $\epsilon_d^{(i)}$, in Eq (4.35) decreases, the regularisation parameter should simultaneously decrease (Jakobsen and Tveit, 2018). This can be referred to as a cooling scheme, as the parameter is “cooled” (decreased) in each iteration i. By combining the discrepancy principle mentioned above, with a cooling scheme for updating the regularisation parameter λ (Farquharson and Oldenburg, 2004), the regularisation parameter is given by (Hesford and Chew, 2010; Jakobsen and Ursin, 2015)

$$\lambda^{(i+1)} = a\lambda^{(i)}, \tag{4.37}$$

where the constant a can be arbitrarily defined as $0.5 \leq a \leq 0.9$. Selecting this constant is crucial in regularisation problems, as a too high value slows the inversion process.

The self-adaptive scheme is an extension of the cooling scheme in Eq. (4.37), to make it probable that a global minimum is found (Jakobsen et al., 2020b). It is based on the Levenberg-Marquardt method for regularising the non-linear least-squares problem (Ciric and Qin, 1997; Aster et al., 2018). As long as the data error is decreasing, the given cooling scheme in Eq. (4.37) is used. However, if the data error does not decrease, one must reset the model and increase the regularisation parameter (Jakobsen et al., 2020b) by

$$\lambda^{(i+1)} = b\lambda^{(i)}, \tag{4.38}$$

where b is a constant larger than one (e.g. 1.4).

For simple problems, the starting regularisation parameter can be chosen as $\lambda^{(0)} = 0.001$. However, a more precise starting value is defined by (Ciric and Qin, 1997; Lavarello and Oelze, 2009; Jakobsen et al., 2020b)

$$\lambda^{(0)} = 10\text{mean}(\text{diag}(\mathbf{H}^{(0)})), \tag{4.39}$$

where *mean* is the mean value of the elements, *diag* is the diagonal, and $\mathbf{H}^{(0)}$ is the Hessian matrix given in Eq. (4.32).

One issue of the self-adaptive regularisation scheme, is that the starting value of the regularisation parameter, $\lambda^{(0)}$, can be selected to be too small (Farquharson and Oldenburg, 2004). The arbitrary value of 10, is then used to increase the starting regularisation parameter (e.g. Jakobsen et al., 2020b).

In this work, the self-adaptive scheme, in Eqs. (4.37) and 4.38, is used to ensure a more stable convergence for the DBI inversion.

Algorithm 2: Algorithm for the implementation of the DBI inversion method in an anisotropic elastic media, with references to relevant expressions. The critical scheme for the regularisation parameter, λ, is the self-adaptive method, as described in Section 4.2.4, with constants $a = 0.5$ and $b = 1.4$. In the context of the numerical results below, $\omega_{\min} = 6\pi$, and $\omega_{\max} = 20\pi$. This algorithm is mainly inspired by Jakobsen et al. (2020b).

```
Setting up the model grid, with sources, receivers, and positions.
Define model based on initial model, $\mathbf{m}^{(i)} = \mathbf{m}^{(0)}$, often $\mathbf{m}^{(0)} = \mathbf{0}$.
for $\omega = \omega_{min}$ to $\omega_{min}$ do
    Compute reference Green's tensors, $\mathbf{M}^{(0)}$ and $\mathbf{\Gamma}^{(0)}$, as described in Appendix B.
    Compute reference strain tensor, $\boldsymbol{\varepsilon}^{(0)}$, by Eqs. (2.2) and (3.2).
    Compute scattering potential, $\mathbf{V}$, from Eq. (3.24), based on the model, $\mathbf{m}$.
    Calculate exact solution of $\mathbf{M}$ and $\boldsymbol{\varepsilon}$, by Eqs. (4.14) and (3.30).
    Calculate sensitivity matrices, $\mathbf{J}^{(0,p)}$, in Eq. (4.24), by $\mathbf{M}$, $\mathbf{B}^{(p)}$, and $\boldsymbol{\varepsilon}$.
    Compute observed data, $\delta\mathbf{u}^{\text{obs}}$, by Eq. (4.34), and the true model.
    Define iteration number $i = 0$.
    Set data errors $\epsilon_d = 1$, $\epsilon_d' = 1$, and tolerance $\eta_0 = 10^{-5}$ or $\eta_0 = 10^{-2}$.
    while $\epsilon_d > \eta_0$ do
        Update iteration number $i = i + 1$.
        Update strain tensor, $\boldsymbol{\varepsilon}^{(i)}$, and Green's tensor, $\mathbf{M}^{(i)}$, by Eqs. (4.12) and (4.13).
        Update sensitivity matrices, $\mathbf{J}^{(i,p)}$, by $\mathbf{M}^{(i)}$, $\mathbf{B}^{(p)}$, and $\boldsymbol{\varepsilon}^{(i)}$.
        Compute gradient vector, $\mathbf{G}^{(i)}$, and Hessian matrix, $\mathbf{H}^{(i)}$, in Eqs. (4.31) and
         (4.32), respectively.
        if $i = 1$ then
            Set initial regularisation parameter, $\lambda^{(i)}$, by Eq. (4.39).
        end
        Calculate updated model, $\mathbf{m}^{(i+1)}$, by Eq. (4.30).
        Calculate data error and model error, in Eqs. (4.35) and (4.36), for $\mathbf{m}^{(i+1)}$.
        if $\epsilon_d < \epsilon_d'$ then
            Decrease regularisation parameter by Eq. (4.37).
            Set $\epsilon_d = \epsilon_d'$ and $\mathbf{m}^{(i)} = \mathbf{m}^{(i+1)}$.
        else
            Increase regularisation parameter by Eq. (4.38), and set $\mathbf{m}^{(i+1)} = \mathbf{m}^{(i)}$.
        end
    end
end
```

4.3 Numerical Results and Discussion

The goal in this section is to analyse the performance of the DBI inversion method for estimating the stiffness perturbation in fractured media. The inversion scheme, explained in Section 4.2.3 and Algorithm 2, has been implemented by an extension of Matlab programs from Jakobsen et al. (2020b). The following frequencies were used in the sequential inversion for frequency: 3 Hz, 5 Hz, 7.5 Hz, and 10 Hz. See Section 2.4 for more details on the models used. The synthetic data is set up to be the same as in Chapter 3, for the two cases: (i) noiseless (clean) data, and (ii) noisy data with an SNR of 40 dB corresponding to a noise-level of 1% (10^{-2}).

The stiffness perturbations that are used in these results have been normalised per Eq. (4.17), to ensure they are somewhat similar in magnitude. The model vector, $\mathbf{m}$, contains the four independent (normalised) stiffness perturbations, for each grid cell n. It should be noted that for these computations, there are a total of 4100 parameters ($4N$) in the model vector, $\mathbf{m}$.

The inversion is based on the generalised Tikhonov regularisation in Eq. (4.29), by updating the model in Eq. 4.30. The tolerance, η_0, is set to 10^{-5} for clean (noiseless) data, while it is set to 10^{-2} for noisy data (40 dB SNR). The inversion process is stopped when this tolerance is reached, according to Morozov's discrepancy principle as mentioned above. The regularisation scheme is based on the self-adaptive approach (Ciric and Qin, 1997; Jakobsen et al., 2020b), discussed in Section 4.2.4. Different constants for "cooling" and "heating" were investigated, and the following constants gave the best results: $a = 0.5$ and $b = 1.4$.

The computation times and model errors of the respective models are summarised in Table 4.1. Note that computation time refers to time spent performing both modelling and DBI inversion for all frequencies.

Table 4.1: Comparison of the final model error ϵ_m [unit], and computation time τ_{CPU} [min], for the DBI stiffness-inversion results. For the noiseless results (5000 dB SNR), the tolerance was 10^{-5}, while for the noisy results (40 dB SNR) it was 10^{-2}.

Model	Noise	ϵ_m	τ_{CPU}[1]
Syncline	no	0.155	592
	yes	0.355	419
Anticline	no	0.198	591
	yes	0.548	345

---

[1] Computation time based on the following processor (CPU) and memory: Intel i5-8250U 1.6GHz - 1.8GHz, 8GB RAM.

4.3.1 Syncline Model

The syncline model was defined in Section 2.4.1, and the corresponding stiffness perturbation model was displayed in Section 3.4.1. There are 1025 grid blocks, in a grid of dimension 41x25. A total of 41 sources and receivers are placed at the surface ($z = 0$ m), for the numerical experiments. The configuration of these sources and receivers were shown in Fig. 3.3.

The DBI inversion results for the syncline model, for C_{11} and C_{33}, are shown in Figs. 4.1a and 4.1b, respectively, and are close to the true model in Figs. 3.4a and 3.4b. As the change in the C_{11} parameter is minimal, the inversion result is mainly shown for completeness. For the C_{33} parameter, however, the model has been recovered well. The layering and complex features of the true model, are represented well due to the higher contrast, as seen in Figs. 4.1b and 4.1d. C_{33} is arguably the most important parameter in the case of horizontal fractures. Figs. 4.1c and 4.1d show the inversion results for the C_{55} and C_{13} parameters, respectively. Both these inverted (normalised) stiffness perturbations fit well with their respective true models. The absolute error of the inversion results is shown in Fig. 4.2. Overall, the absolute error of the individual stiffness parameters is quite low. It is safe to say that the anisotropic DBI inversion for the syncline model corresponding to noiseless data is successful, by evaluating Figs. 4.1 and 4.2. The "stairs-feature" of the C_{33} and C_{13} parameters, shown in Figs. 4.2b and 4.2d, is clearly difficult in inversion.

In Fig. 4.3, the performance of the inversion in terms of error and regularisation is displayed. Fig. 4.4 shows the final inverted model vector compared with the true and starting model vectors. The final model error in Fig. 4.3 reaches an acceptable level, based on the complexity of the model, and has a stable convergence, which is reasonable for clean data. The residual data error decreases and to the tolerance (noise-level). Fig. 4.4 show that the inversion for this model is somewhat tricky, as there are many rapid changes of stiffness. Nevertheless, the inverted model vector provides an excellent fit to the true model vector. Total computation time was 592 minutes, and the final model error was 0.155 (15.5%).

The corresponding DBI inversion results of the noisy data of 40 dB SNR, are shown in Fig. 4.5. Fig. 4.5a show that the minimum change in the C_{11} parameter is not visible, and there are a few areas of wrong perturbation along the sides of the model. However, the C_{33} parameter in Fig. 4.5b is noticeably better than for the C_{11}, in Fig. 4.5a. The parameters of C_{55} and C_{13} are shown in Figs. 4.5c and 4.5d, respectively. For the C_{55} parameter, the first layer and the syncline feature is visible. Similarly for the C_{13} parameter, the syncline is apparent, but the lower layer is slightly wrong in comparison with the true model in Fig. 3.4d. Absolute error of the inverted stiffness parameters are shown in Fig. 4.6. The C_{13} parameters in Fig. 4.6d, specifically, has a considerably higher absolute error than the other parameters. This result is consistent with results from similar experiments, indicating the difficulty in inverting for the C_{13} stiffness (e.g. Tsvankin, 2012; Jakobsen et al., 2017).

Similarly to above, the inversion performance is given in Fig. 4.7, while Fig. 4.8 show the fit of the inverted model vector versus the true model. Judging the performance of the DBI inversion for the noisy data in Fig. 4.7, it is evident that the noise introduces some problems. The residual data error decreases monotonically to the noise-level (tolerance) of 10^{-2}, while the model error reaches a fairly high level, compared to the noiseless inversion of Fig. 4.3. In Fig. 4.6, absolute error estimates of the inversion results are displayed. The main contribution to the high model error, as seen in Fig. 4.6d, is due to the C_{13} parameter, which is consistent with Lee et al. (2010) and Kamath and Tsvankin (2016). For the other stiffness parameters, the results are considerably better. Total computation time was 419 minutes, and the final model error was 0.355 (35.5%). Due to the stopping criteria (tolerance) being lower, in the case of noisy data, the computation time is shorter.

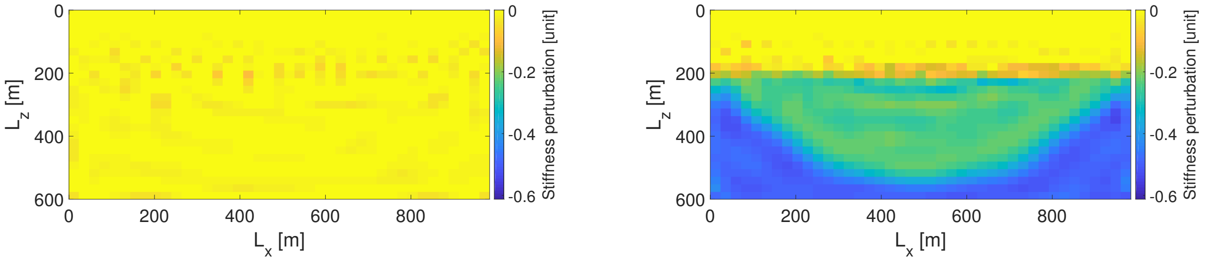

(a) ΔC_{11} (b) ΔC_{33}

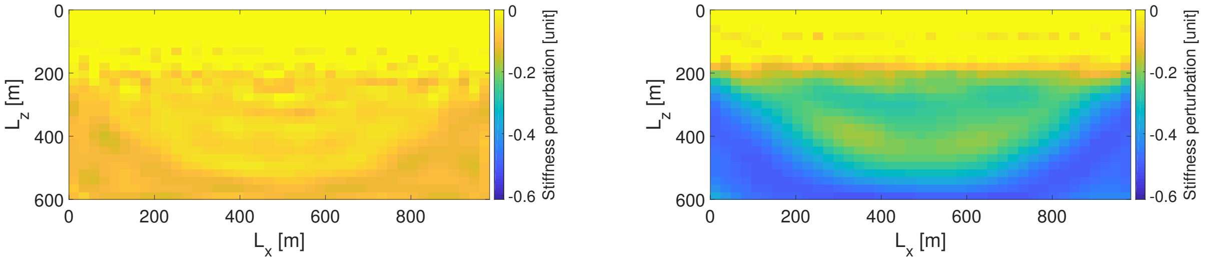

(c) ΔC_{55} (d) ΔC_{13}

Figure 4.1: DBI inversion results for normalised stiffness perturbation in the syncline model. The data used was noiseless, and the colour map is the same for all parameters.

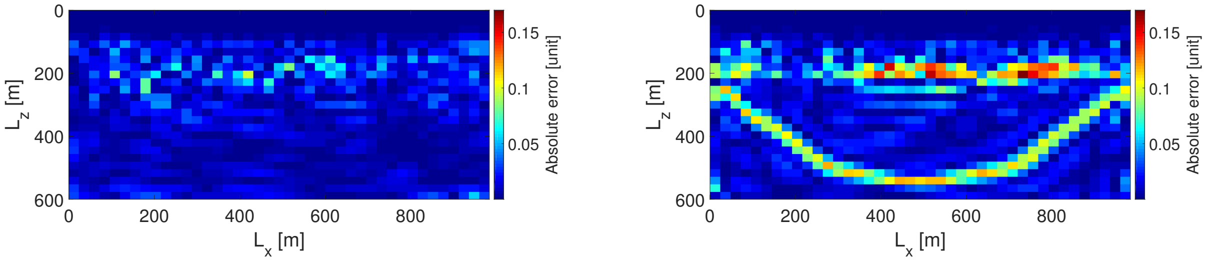

(a) ΔC_{11} (b) ΔC_{33}

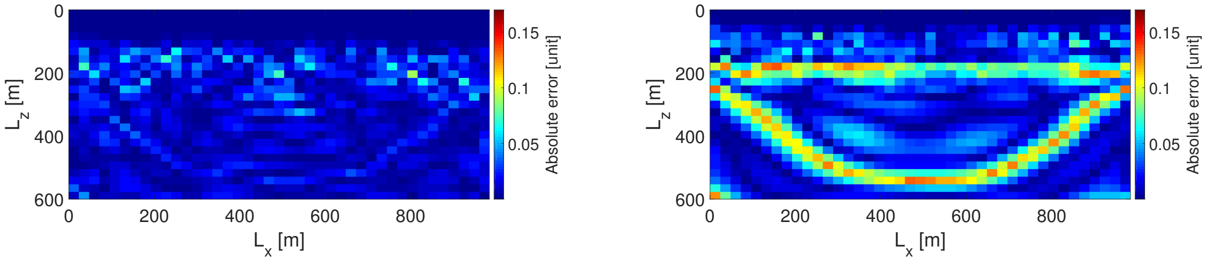

(c) ΔC_{55} (d) ΔC_{13}

Figure 4.2: Absolute error of the inverted normalised stiffness perturbation in the syncline model, for the noiseless data. The colour map for absolute error is the same for all parameters.

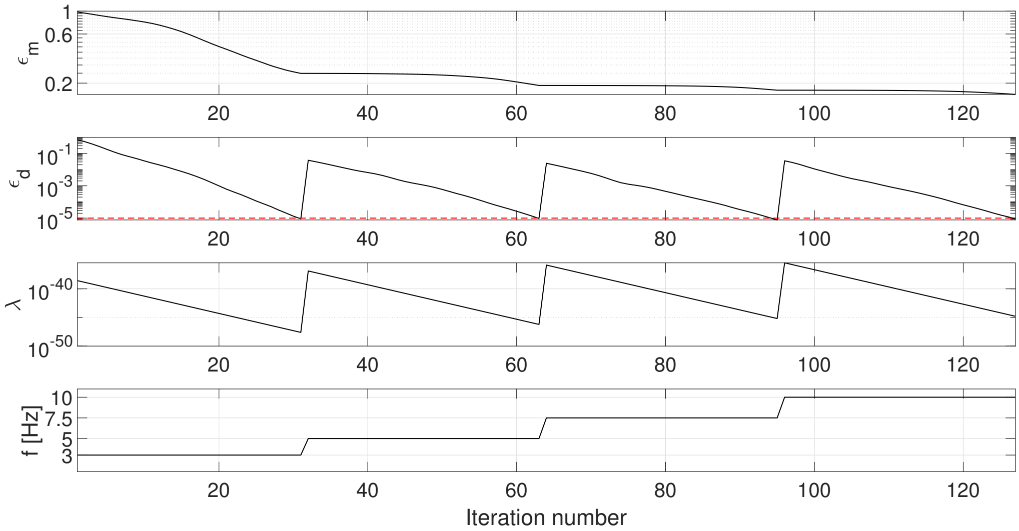

Figure 4.3: Performance of the DBI inversion for stiffness perturbation in the syncline model, for the noiseless data. Model error (ϵ_m) and residual data error (ϵ_d) depend on the iteration number. The equations for data and model error are given in Eqs. (4.35) and (4.36). The data error converges to the noise-level (red dashed line). The last two plots show the regularisation parameter (λ) and the frequency (f), respectively.

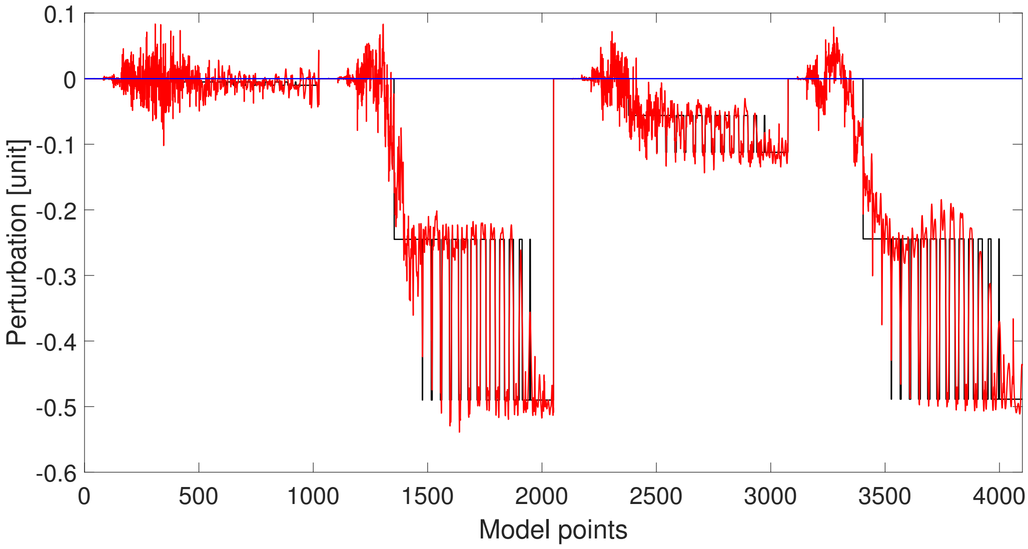

Figure 4.4: Model vector of the DBI inversion result for stiffness perturbation in the syncline model, for the noiseless data. The starting model is shown as a blue line, the true model as a black line, and the inversion results as a red line.

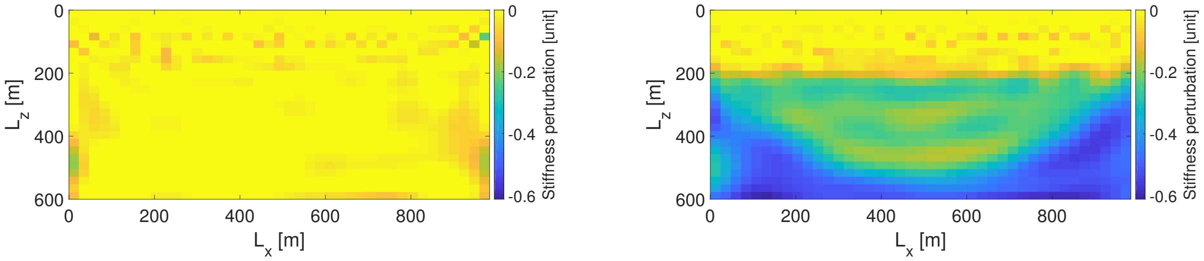

(a) ΔC_{11} **(b)** ΔC_{33}

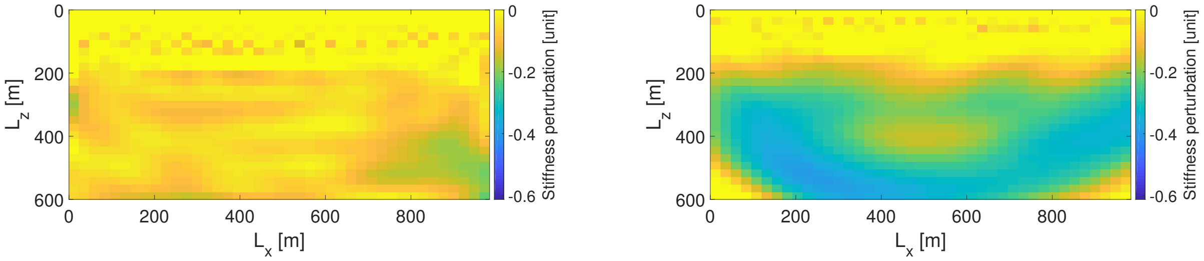

(c) ΔC_{55} **(d)** ΔC_{13}

Figure 4.5: DBI inversion result for the normalised stiffness perturbation in the syncline model, for the noisy data with an SNR of 40 dB. The colour map is the same for all parameters.

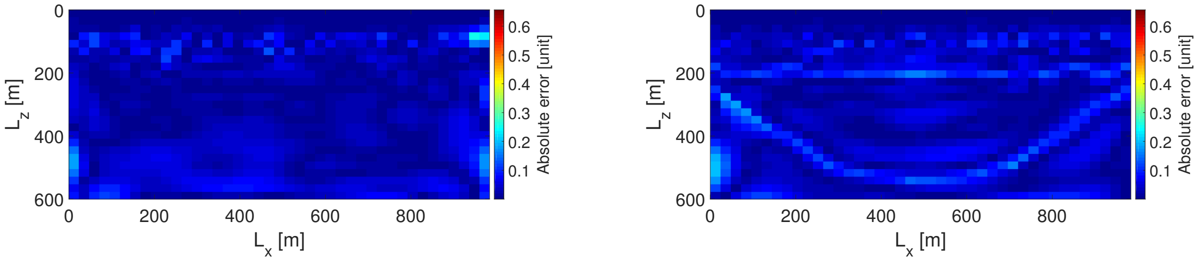

(a) ΔC_{11} **(b)** ΔC_{33}

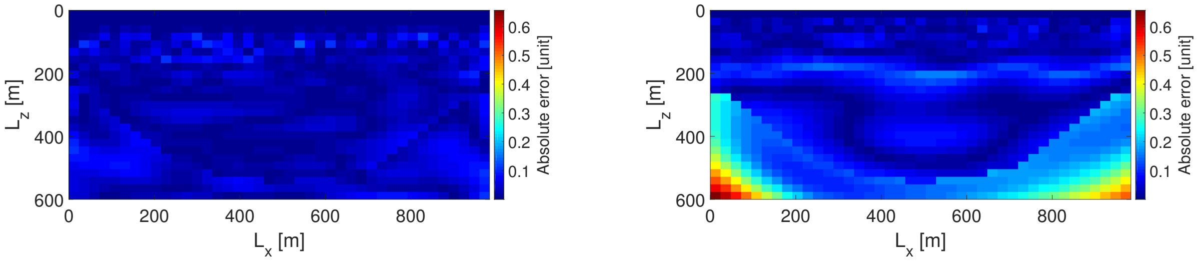

(c) ΔC_{55} **(d)** ΔC_{13}

Figure 4.6: Absolute error of the inverted normalised stiffness perturbation in the syncline model, for the noisy data of 40 dB SNR. The colour map for absolute error is the same for all parameters.

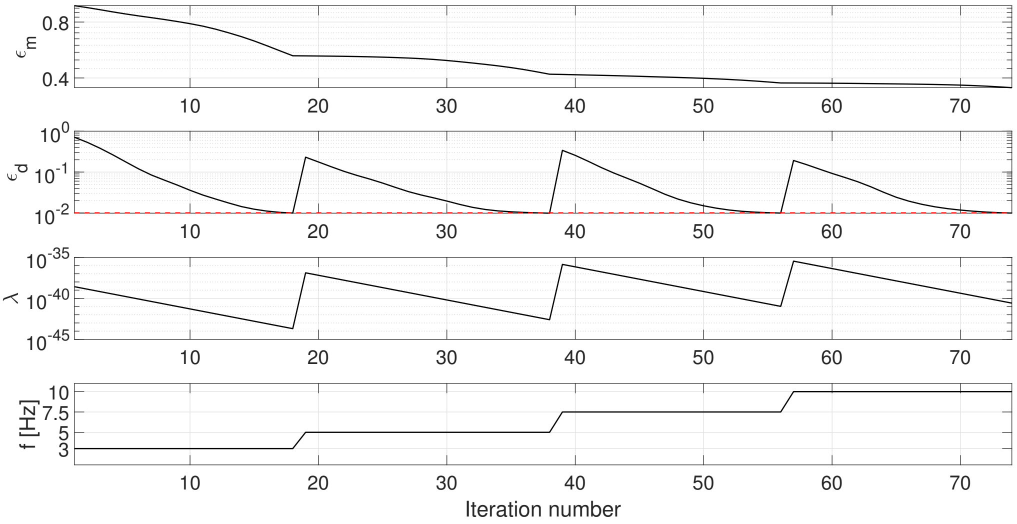

Figure 4.7: Performance of the DBI inversion for stiffness perturbation in the syncline model, for noisy data of 40 dB SNR. Model error (ϵ_m) and residual data error (ϵ_d) depend on the iteration number. The data error converges to the noise-level (red dashed line). The last two plots show the regularisation parameter (λ) and the frequency (f), respectively.

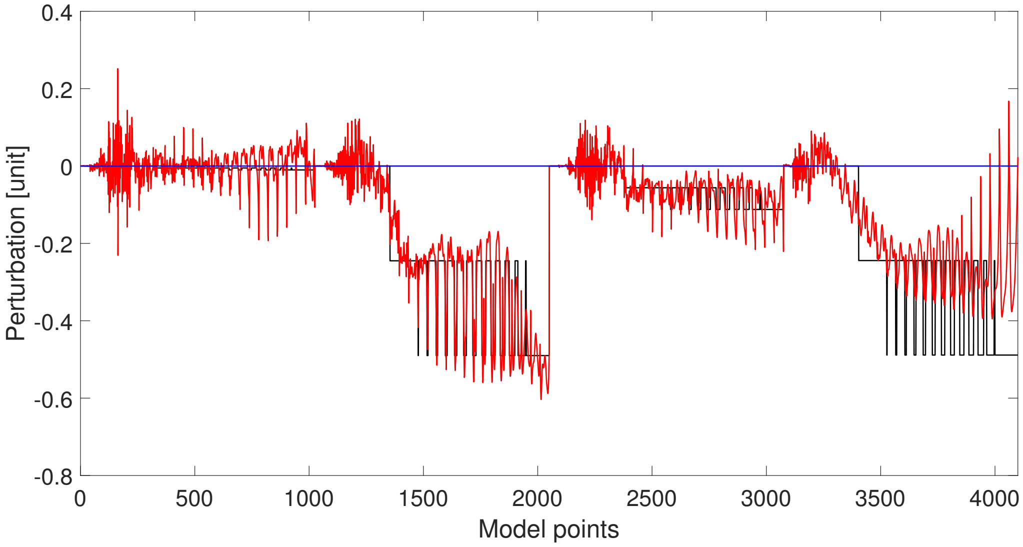

Figure 4.8: Model vector of the DBI inversion result for the stiffness perturbation in the syncline model, for noisy data of 40 dB SNR. The starting model is shown as a blue line, the true model as a black line, and the inversion results as a red line.

4.3.2 Anticline Model

The anticline model that is used for DBI inversion in this section is based on the stiffness perturbation model defined in Section 3.4.2. Stiffness perturbations have been normalised, as per Eq. (4.17), and correspond to the fracture density model referenced in Section 2.4.2. In this model, there are a total of 1107 grid blocks on a grid with dimensions 41x27. Sources and receivers are placed at the surface, and the configuration is given in Fig. 3.7. The number of sources is 11, while the number of receivers is 41 (the same as in modelling). There are a total of 4428 parameters in the model vector (i.e. $4N$).

Fig. 4.9 show the final DBI inversion result for the anticline model. The data is clean (noiseless), and was computed for the maximum frequency of 10 Hz. The inversion results in Fig. 4.9a and 4.9b, are successful in terms of retaining the main features of the true models in Section 3.4.2. Specifically, in Fig. 4.9b, for the C_{33} parameter, the anticline layer (in blue) is distinct and recognisable. The absolute error of the inversion results are displayed in Fig. 4.10, where some erroneous points in the upper layer for all parameters can be seen. These inaccuracies are the result of the low ratio between data points and model values. The C_{55} and C_{13} parameters in Figs. 4.9c and 4.9d, respectively, show good inversion results. For the C_{55} parameter, the features around the anticline layer (middle) are a little blurry. Finally, the C_{13} parameter has inaccurate values below the anticline layer and particularly in the corners, as seen in Fig. 4.10d. These figures are discussed further, with a comparison to the fracture-based inversion results, in Chapter 6.

In Fig. 4.11, the performance of the inversion in terms of error and regularisation is displayed, showing a reasonably successful inversion. The residual data error decreases monotonically, for each frequency, to the noise-level (tolerance) of 10^{-5}. The model error reaches a reasonably low level, and the inversion process is stable. Fig. 4.12 shows the final inverted model vector compared with the true and starting model vectors. The issues in the parameters are apparent throughout the model vector, as there are fluctuations around the true model. In particular, the erroneous points in the C_{13} parameter can be seen to the right in the model vector (beyond point no. 4000). The total computation time was 591 minutes, and the final model error was 0.198 (19.8%) for these results. The model error, in the anticline model, is acceptable for a multi-parameter FWI.

The final DBI inversion results for the anticline model are displayed in Fig. 4.13, for data containing noise with an SNR of 40 dB. It is evident that noise causes inaccuracies in the DBI inversion. Erroneous points are visible when looking at the absolute error of the different stiffness parameters in Fig. 4.14, especially in the C_{13} parameter below 200 m depth. Similarly to the noiseless results, the C_{11} and C_{33} parameters seem to provide good matches to the true models in Section 2.4.2. These two parameters, in particular, are considerably worse along the edges compared to the rest of the model. The inversion results for the C_{55} and C_{13} parameters are inaccurate, and the most prominent feature of the model is "lost". Specifically, for the C_{55} parameter, it is not easy to make out a single layer. These results are further discussed, and compared the noiseless inversion results, in Chapter 6.

The performance of the DBI inversion for the noisy data is shown in Fig. 4.15. The inversion is worse than previous examples. Even though the residual data error decreases monotonically to the noise-level (tolerance) of 10^{-2}, the final model error is on the high side (almost 60%) even for multi-parameter FWI. In the model vector of Fig. 4.16, the erroneous values in the C_{13} parameter can be seen to the right (beyond model point no. 3700) as these values diverge from the correct values. As mentioned before, in Section 4.3.1, the inversion is difficult for the C_{13} parameter, such that the high error is not surprising. The total computation time was 345 minutes, and the final model error was 0.548 (54.8%) for these results.

In the case of noisy data for the anticline model, the DBI inversion breaks down and does not succeed in resolving all the parameters. Another contribution to the overall inaccurate results, for the anticline model, is that fewer sources, compared to in the syncline model, were used to lower the computational cost. Using a large number of sources increases the number of data points in the data vector, thus resulting in a better match to a large number of parameters in the model.

The erroneous C_{13} parameter is a substantial contribution to the high model error in the anticline model for the noisy data. In Fig. 4.14d, the two lower layers for C_{13} have extremely high absolute error compared to the other parameters. Lee et al. (2010) found that the C_{13} parameter is generally difficult to resolve in anisotropic inversion. Tsvankin (2012) and Kamath and Tsvankin (2016) propose that this problem is due to the trade-off between the P-wave signature of C_{55} and C_{13}. Which may explain the high degree of error in these numerical results.

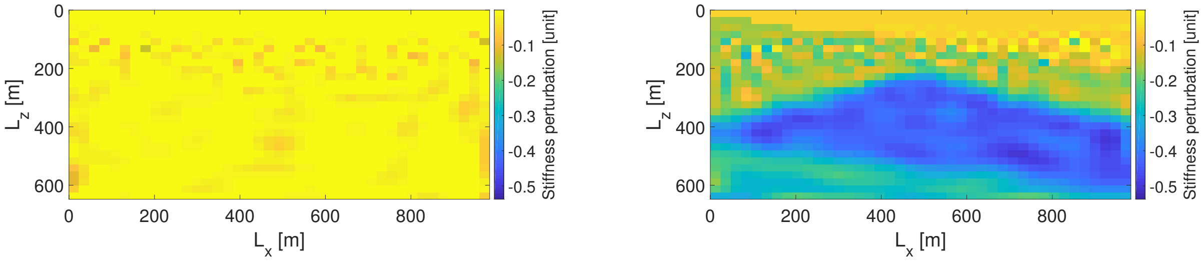

(a) ΔC_{11} **(b)** ΔC_{33}

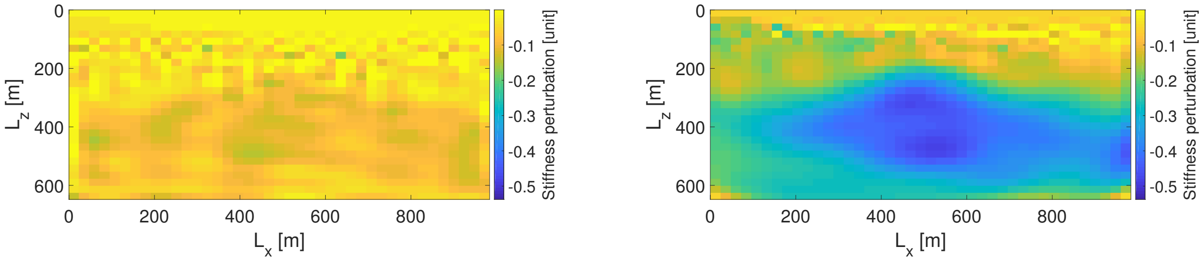

(c) ΔC_{55} **(d)** ΔC_{13}

Figure 4.9: DBI inversion result for the normalised stiffness perturbation in the anticline model, for the noiseless data. The colour map is the same for all parameters.

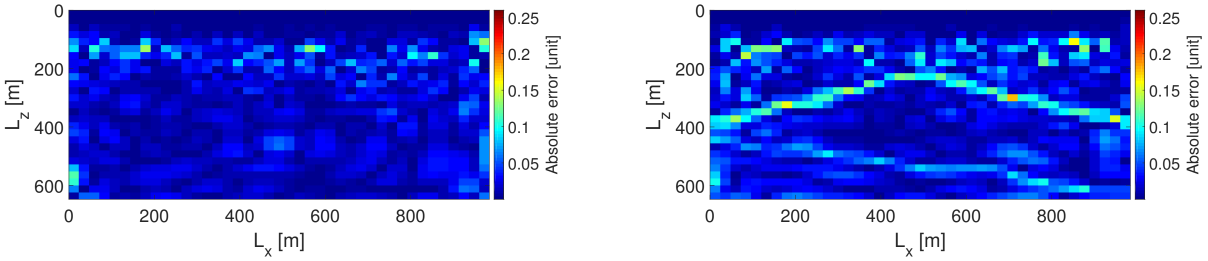

(a) ΔC_{11} **(b)** ΔC_{33}

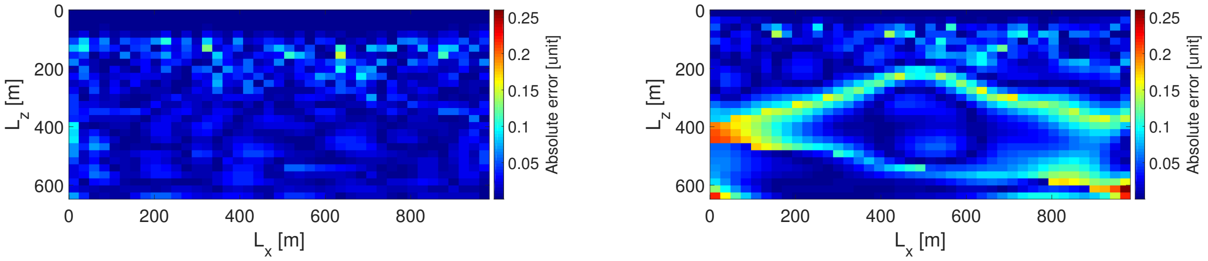

(c) ΔC_{55} **(d)** ΔC_{13}

Figure 4.10: Absolute error of the inverted normalised stiffness perturbation in the anticline model, for the noiseless data. The colour map for absolute error is the same for all parameters.

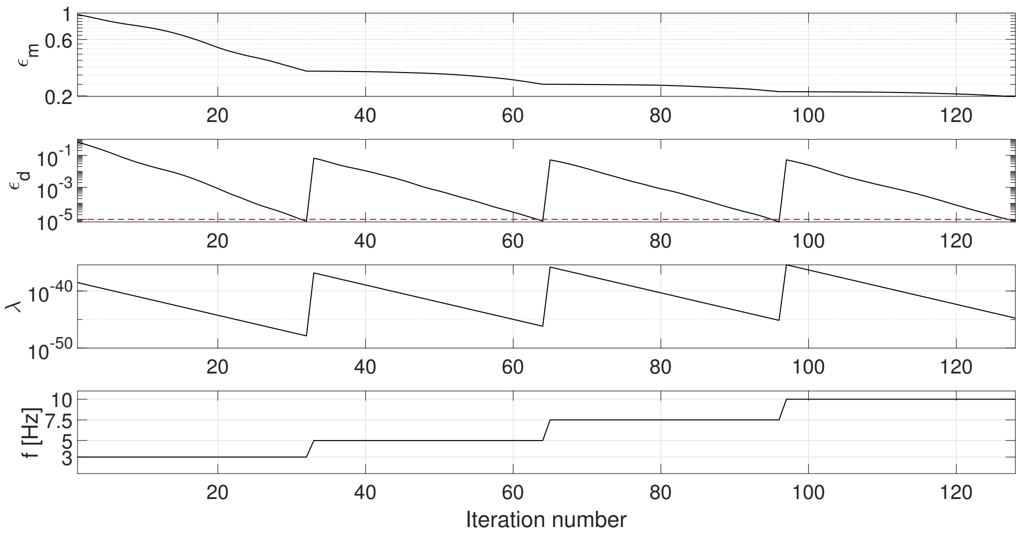

Figure 4.11: Performance of the DBI inversion for stiffness perturbation in the anticline model, for the noiseless data. Model error (ϵ_m) and residual data error (ϵ_d) depend on the iteration number. The equations for data and model error are given in Eqs. (4.35) and (4.36). The data error converges to the noise-level (red dashed line). The last two plots show regularisation parameter (λ) and frequency (f), respectively.

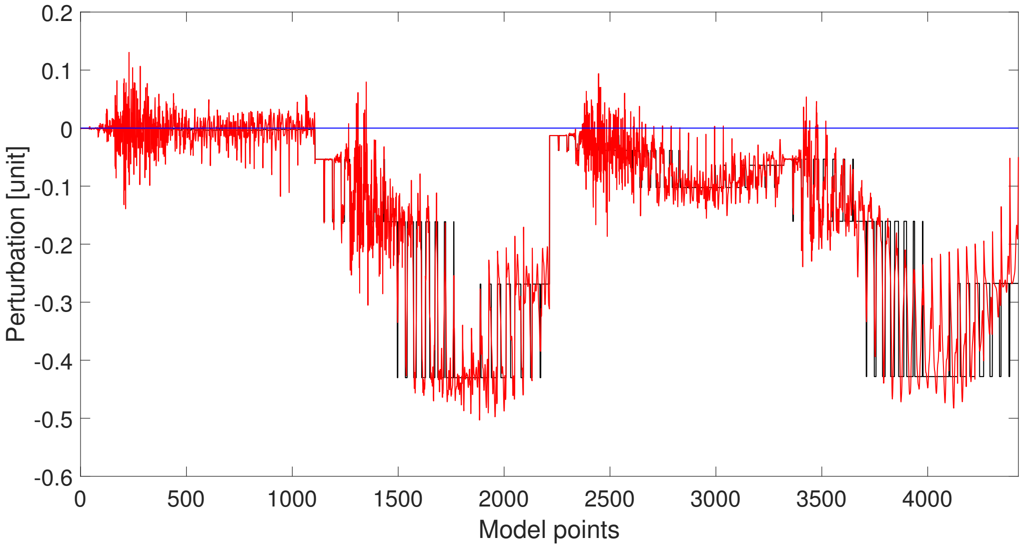

Figure 4.12: Model parameters of the DBI inversion result for the normalised stiffness perturbation in the anticline model, for the noiseless data. The starting model is shown as a blue line, the true model as a black line, and the inversion results as a red line.

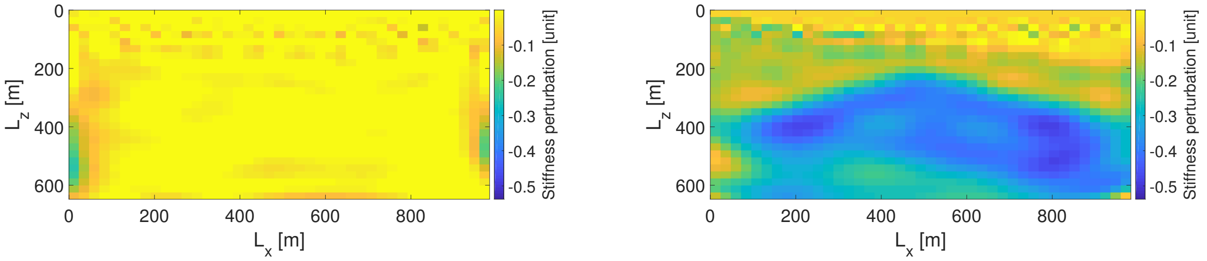

(a) ΔC_{11} **(b)** ΔC_{33}

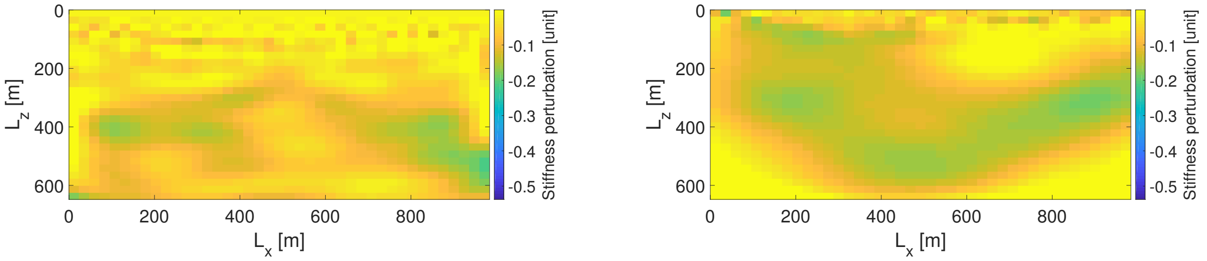

(c) ΔC_{55} **(d)** ΔC_{13}

Figure 4.13: DBI inversion result for the normalised stiffness perturbation in the anticline model, for the noisy data with an SNR of 40 dB. The colour map is the same for all parameters.

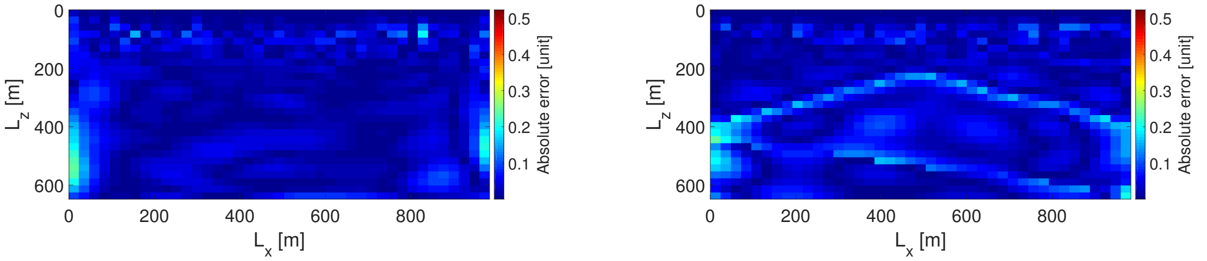

(a) ΔC_{11} **(b)** ΔC_{33}

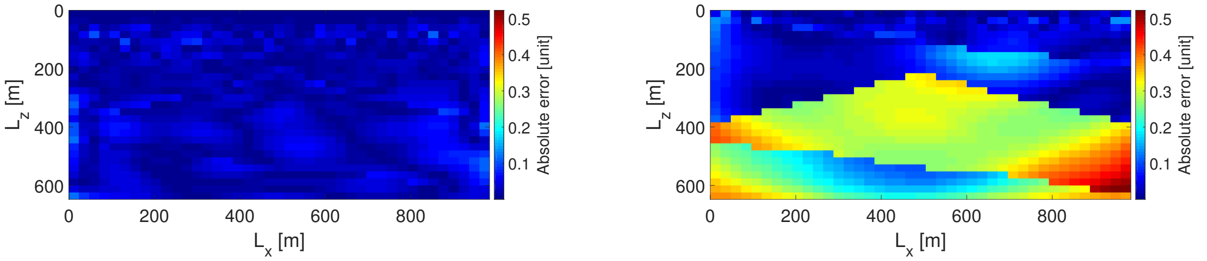

(c) ΔC_{55} **(d)** ΔC_{13}

Figure 4.14: Absolute error of the inverted normalised stiffness perturbation in the anticline model, for the noisy data of 40 dB SNR. The colour map for absolute error is the same for all parameters.

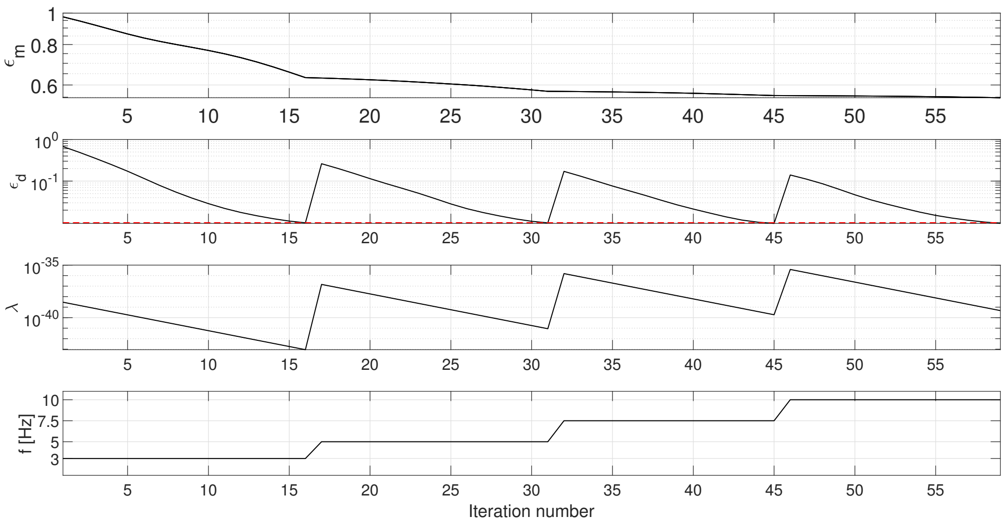

Figure 4.15: Performance of the DBI inversion for stiffness perturbation in the anticline model, for data with noise of 40 dB SNR. Model error (ϵ_m) and residual data error (ϵ_d) depend on the iteration number. The data error converges to the noise-level (red dashed line). The last two plots show regularisation parameter (λ) and frequency (f), respectively.

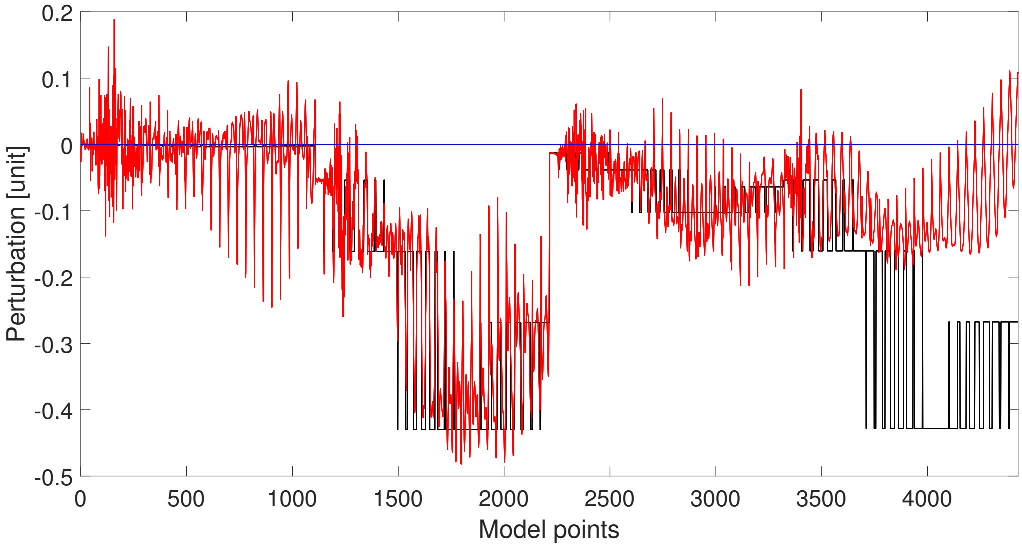

Figure 4.16: Model parameters of the DBI inversion result for the stiffness perturbation in the anticline model, for data with noise of 40 dB SNR. The starting model is shown as a blue line, the true model as a black line, and the inversion results as a red line.

Chapter 5

Waveform Inversion for Fracture Parameters

Waveform inversion for fracture parameters is done for the full solution to a Lippmann-Schwinger integral-equation, combined with the DBI inversion method. First, the reason behind the importance of inverting for fractures is explained. Then, the equations and methods used to represent fractures, model fracture-induced anisotropic media, and invert for fracture parameters are summarised. Lastly, numerical results are presented for the two models referenced in previous chapters.

5.1 Introduction

The primary objective of this chapter is to extend the pioneering work by Jakobsen et al. (2003a), Bansal and Sen (2010), and Pilskog et al. (2015), on seismic inversion for fractures. Jakobsen et al. (2003a) represented fractures in a porous medium by the t-matrix for a single inclusion. Bansal and Sen (2010) implemented an inversion scheme for fractures based on the ray-Born approximation. Pilskog et al. (2015) extended the inversion for fractures to FWI using the t-matrix.

Combining seismic and rock physics models, fracture parameters can be inverted for directly (Pilskog et al., 2015). Fracture parameters only have a small range of plausible values, and the parameters have a direct geological interpretation (Pilskog et al., 2015). The fracture parameter in the context of this thesis, is the fracture density (e.g. Hudson, 1980; Schoenberg and Douma, 1988; Jakobsen et al., 2003a; Sayers, 2009; Bansal and Sen, 2010; Pilskog et al., 2015).

Small-scale heterogeneities such as cracks, fractures and inclusions, can be modelled using integral-equation methods (Carcione et al., 2002; Krebes, 2004). The integral-equation method used in this work is based on the full integral solution of the Lippmann-Schwinger equation (Jakobsen et al., 2020b).

In this chapter, he DBI-method for non-linear inversion in Jakobsen et al. (2020b), is used to extend the fracture-based inversion in Bansal and Sen (2010) and Pilskog et al. (2015). Fracture density constitutes only one model parameter, making it suitable for non-linear inversion (Pilskog et al., 2015).

5.2 DBI Inversion for Fracture Density

Fractures can be represented by a stiffness perturbation, as seen in Section 2.3.3, with the t-matrix for a single inclusion. If only the first-order correction is accounted for, the expressions for stiffness perturbation can be given as in Eqs. (2.9) and (2.13). Only one phase/type of isolated, horizontal fractures is assumed in this implementation, which results in the t-matrix of Eq. (2.11). This t-matrix, $\mathbf{t}$, is constant for all grid blocks $\mathbf{x}$, and can be calculated with the Green's tensor in Appendix A. Fracture density, $\epsilon(\mathbf{x})$, was defined in terms of the porosity of a fracture in Eq. (2.16). Consequently, the relationship between stiffness perturbation and fracture density is given by

$$\Delta\mathbf{C}(\mathbf{x}) = \mathbf{t}\epsilon(\mathbf{x}), \tag{5.1}$$

which corresponds to Eqs. (2.17) and (2.24) in Section 2.3.3. Note that the volume contribution $\frac{4\pi}{3}\alpha_c$ was dropped in order to write the relation on a compact form.

In Chapter 3, a solution to the elastodynamic wave equation in Eq. (3.1), was found to be integral-equations of the Lippmann-Schwinger type (see Section 3.2). The resulting scattered wavefield, $\delta\mathbf{u}$, in Eq. (3.16) can be written in subscript notation (Jakobsen et al., 2003a; Pilskog et al., 2015), and expressed by a decomposition of the stiffness tensor in Eq. (4.18). The decomposition of the stiffness perturbation, $\Delta\mathbf{C}(\mathbf{x})$, is given in Eq. (4.16), where the B-matrix, $\mathbf{B}$, and model parameter vector, $m(\mathbf{x})$, was used. For a model vector containing normalised stiffness perturbations, calculated in Eq. (4.17), the stiffness perturbation is given by

$$\Delta\mathbf{C}(\mathbf{x}) = \mathbf{B}m(\mathbf{x}). \tag{5.2}$$

In fracture density inversion, there is only one parameter in the model vector, such that $m(\mathbf{x}) \equiv \epsilon(\mathbf{x})$. Comparing Eqs. (5.1) and (5.2), it is clear that the stiffness perturbation, $\Delta\mathbf{C}(\mathbf{x})$, can be expressed in the same way as in Chapter 2, and the non-linear inversion scheme used in Chapter 4 is valid. The sensitivity matrix in Eq. (4.24) of Section 4.2.2, can be rewritten with the t-matrix as in Eq. (5.1), instead of the B-matrix. The resulting scattered wavefield depending on fracture density (as the model) is given in Eq. (5.3), with iteration number i.

$$\delta\mathbf{u}^{(i)} = \mathbf{M}^{(i)}\mathbf{t}\boldsymbol{\varepsilon}^{(i)}\mathbf{m}^{(i)}\delta v, \tag{5.3}$$

where $\boldsymbol{\varepsilon}^{(i)}$ denotes the strain tensor and $\mathbf{m}^{(i)}$ denotes the model, which in this case is the fracture density.

Employing the same non-linear inversion scheme as in Section 4.2.2, Eq. (5.3) can be represented by a sensitivity matrix similar to that in Eq. (4.24) by:

$$\mathbf{J}^{(i)} = \mathbf{M}^{(i)}\mathbf{t}\boldsymbol{\varepsilon}^{(i)}\delta v, \tag{5.4}$$

where the Green's tensor, $\mathbf{M}^{(i)}$, and strain tensor, $\boldsymbol{\varepsilon}^{(i)}$, are updated according to Eqs. (4.12) and (4.14), respectively.

Thus, the updated scattered wavefield in each iteration is given by

$$\delta\mathbf{u}^{(i)} = \mathbf{J}^{(i)}\delta\mathbf{m}^{(i+1)}, \tag{5.5}$$

which is equivalent to Eq. (4.23).

The model perturbation is given by $\delta\mathbf{m}^{(i+1)} = \mathbf{m}^{(i+1)} - \mathbf{m}^{(i)}$, where $\mathbf{m}^{(i+1)}$ is the inverted fracture density calculated in Eq. (4.30).

Interested readers should note that the theory presented above can be used to model other effects, such as seismic attenuation and poroelastic effects (Jakobsen et al., 2003b; Pilskog et al., 2015).

Ultimately, the DBI inversion scheme explained in Section 4.2.3 can be used to invert for fracture density. This implementation follow Algorithm 2 closely, although the t-matrix, $\mathbf{t}$, is used instead of the B-matrix, $\mathbf{B}$.

In the numerical results presented below, Section 5.3, the rock under consideration will be fully saturated with gas. The t-matrix described above can be used to represent such saturated fractures, which was discussed in Section 2.3.4.

5.3 Numerical Results and Discussion

The fracture density models that were described in Chapter 2 forms the basis for the inversion in this section. The DBI inversion is performed for fracture density, as was discussed in Section 5.2. The t-matrix, $\mathbf{t}$, is used for the relationship between fracture density, ϵ, and stiffness perturbation, $\delta\mathbf{C}$. Modelling is done according to the details provided in Section 3.4. The inversion in this chapter is based on the DBI scheme presented in Section 4.2.3, and on Algorithm 2. For the sequential inversion concerning frequency, the four frequencies used are: 3 Hz, 5 Hz, 7.5 Hz, and 10 Hz.

The regularisation scheme to be used in this section is based on the self-adaptive approach (Ciric and Qin, 1997; Jakobsen et al., 2020b), discussed in Section 4.2.4. Constants for "cooling" and "heating", in Eqs. (4.37) and (4.38), were set to $a = 0.5$ and $b = 1.4$, respectively. A tolerance of 10^{-5} is used for the noiseless data. While for the noisy data, the tolerance is 10^{-2}, corresponding to an SNR of 40 dB. Most variables and parameters are kept the same as in the inversion in Chapter 4, to be able to compare the methods in Chapter 6. Description of differences in variables and parameters will be given where applicable.

The computation times and model errors of the respective models are summarised in Table 5.1. Note that computation time refers to time spent performing both modelling and DBI inversion for all frequencies.

Table 5.1: Comparison of the final model error ϵ_m [unit], and computation time τ_{CPU} [min], for the DBI fracture-inversion results. For the noiseless results (5000 dB SNR), the tolerance was 10^{-5}, while for the noisy results (40 dB SNR) it was 10^{-2}.

Model	Noise	ϵ_m	τ_{CPU}[1]
Syncline	no	0.106	379
	yes	0.133	225
Anticline	no	0.095	448
	yes	0.119	221

---

[1] Computation time based on the following processor (CPU) and memory: Intel i5-8250U 1.6 GHz - 1.8 GHz, 8 GB RAM.

5.3.1 Syncline Model

In this section, fracture density inversion is executed for the syncline model described in section 2.4.1. The modelling aspect was presented in Section 3.4.1, where the levels of noise were described. The total number of grid blocks is 1025, and the dimension of the grid is 41x25. Similar to numerical results, in Section 4.3.1, 41 sources and 41 receivers are used to provide the best illumination. The number of model parameters that need to be inverted is equal to the number of grid blocks.

The fracture density DBI inversion result for the syncline model is shown in Fig. 5.1a. It should be noted that the colour map is the same as in the true model. The absolute error is presented in Fig. 5.1b, where most of the grid blocks have an (absolute) error below 0.02. The inversion is successful as it provides a remarkably close match to the true model in Fig. 2.5. The most erroneous points are at the trough of the syncline, towards the middle of the model (below $z = 450$ m, between $x = 250$ m and $x = 750$ m). There is a clear distinction between the layers, and the syncline feature is evident.

Stiffness perturbations are displayed in Fig. 5.2, corresponding to the inverted fracture density model in Fig. 5.1a. Comparing the inverted stiffness perturbations to the true models in Fig. 3.4, it is clear that all parameters have been inverted correctly. The main syncline feature is clear and visible in all the parameters, although it is quite weak in the C_{11} parameter. The C_{33} and C_{13} parameters have the most significant change for an increased fracture density, as was discussed in Section 4.3.1. The inversion process, concerning the different iterations, is shown in Fig. 5.3, while the model vector is displayed presented in Fig. 5.4. The model- and data-error, in Fig. 5.3, show the stable convergence of the DBI inversion method. The regularisation parameter is decreasing simultaneously with the data error. Inversion for the highest frequencies (5 Hz, 7.5 Hz, 10 Hz) contribute little to decrease the model error further. Although the model error is decreasing monotonically, one would expect the inversion for the last frequencies to have more impact. Finally, the model vector presented in Fig. 5.4 show a precise match between the inverted and correct model parameters. The total computation time for the inversion in case of noiseless data was 379 minutes, while the final model error was 0.106 (10.6%).

Similarly to Section 3.4.1, noise is added to the synthetic data to verify the inversion in a more realistic case. The fracture density inversion result for the syncline model in the case of noisy data, with an SNR of 40 dB, is shown in Fig. 5.5a. The computed absolute error of the inverted fracture density is displayed in Fig. 5.5b. Compared to the noiseless result in Fig. 5.1a, it is overall acceptable but slightly worse. The corners, as well as the syncline feature, show more prominent erroneous grid points, as seen in Fig. 5.5b. From the absolute error measurement, it is obvious that the noisy data somewhat hampers the inversion method. Although assessing the results above, the DBI inversion for fractures appear rather resistant to noise effects.

The stiffness perturbations of the C_{11} and C_{33} parameters are shown in Figs. 5.6a and 5.6b, respectively. In the presence of noise, the changes between the syncline layer and the layer below is still barely visible in the C_{11} parameter. For the C_{33} parameter, the contrast between the layers is visible. Overall the results of these parameters exhibit accurate matches to the true syncline models in Section 3.4.1. Figs. 5.6c and 5.6d show the C_{55} and C_{13} parameters, respectively. Overall, both these stiffness parameters have been recovered by inversion, and they are very close to the noiseless results.

Furthermore, Fig. 5.7 display the DBI inversion performance, while Fig. 5.8 show the model vector. The data error successfully converges to the noise-level of 10^{-2}, while the model error decreases monotonically. For the model vector, the inverted result is further away from the true model than in the noiseless case. Most of the difficult areas in the middle of the model, however, have been recovered successfully. Finally, in the case of noisy data, the computation time was 225 minutes, while the final model error was 0.133 (13.3%). Due to the stopping criteria (tolerance) being lower, in the case of noisy data, the computation time is shorter.

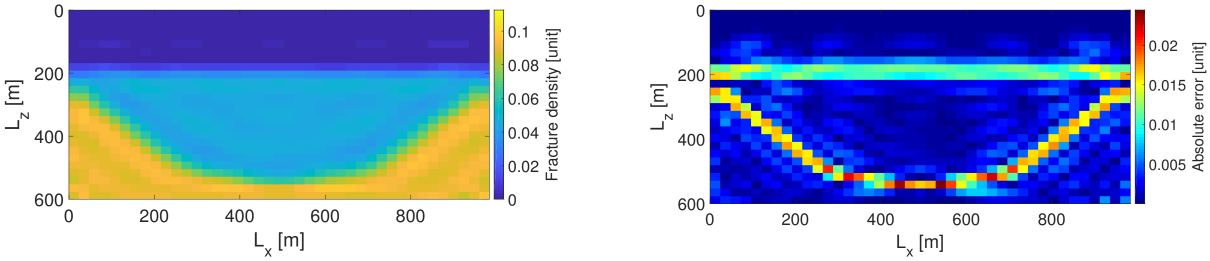

(a) Inverted fracture density

(b) Absolute error

Figure 5.1: DBI inversion result for the syncline model, for the noiseless data.

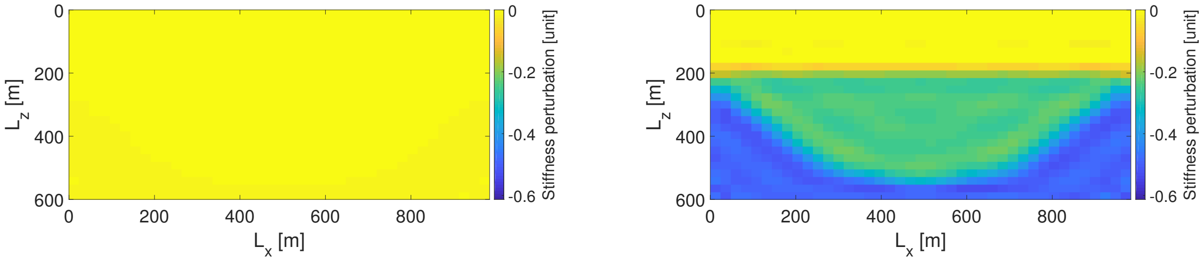

(a) ΔC_{11}

(b) ΔC_{33}

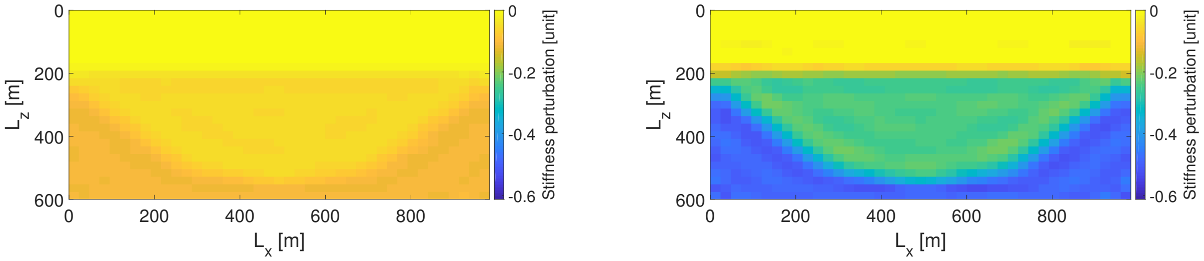

(c) ΔC_{55}

(d) ΔC_{13}

Figure 5.2: The corresponding normalised stiffness perturbations of the syncline model, for the noiseless data. The colour map is the same for all parameters.

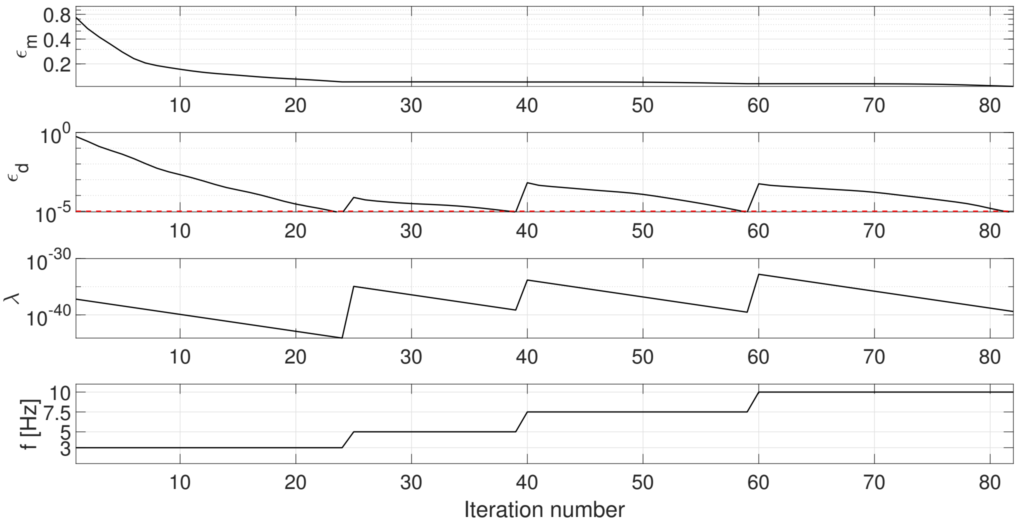

Figure 5.3: Performance of the DBI inversion for stiffness perturbation in the syncline model, for the noiseless data. Model error (ϵ_m) and residual data error (ϵ_d) depend on the iteration number. The equations for data and model error are given in Eqs. (4.35) and (4.36). The data error converges to the noise-level (red dashed line). The last two plots show regularisation parameter (λ) and frequency (f), respectively.

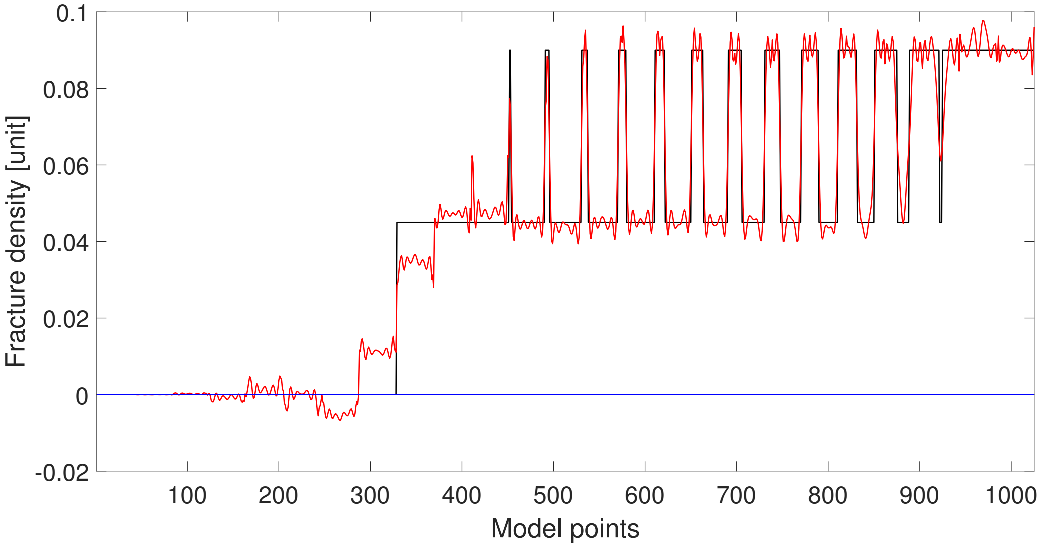

Figure 5.4: Model parameters of the DBI inversion result for the normalised stiffness perturbation in the syncline model, for the noiseless data. The starting model is shown as a blue line, the true model as a black line, and the inversion results as a red line.

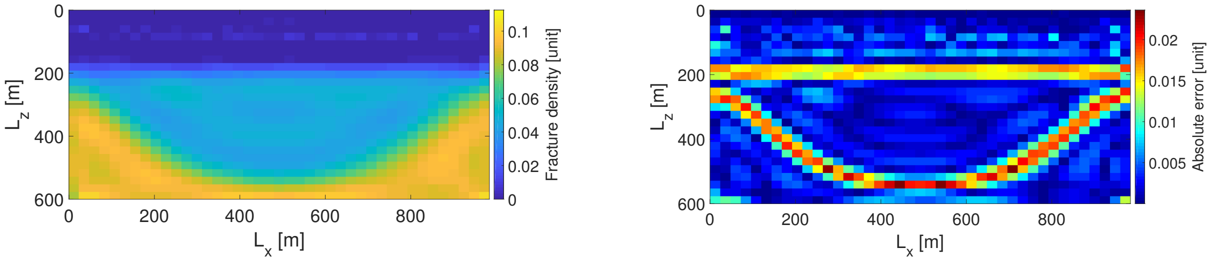

(a) Inverted fracture density **(b)** Absolute error

Figure 5.5: DBI inversion result for the syncline model, with inverted fractured density (left) and absolute error (right). The data is noisy with an SNR of 40dB.

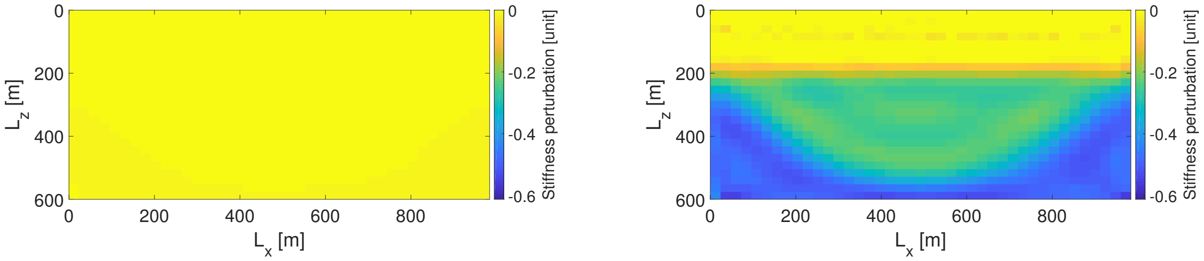

(a) ΔC_{11} **(b)** ΔC_{33}

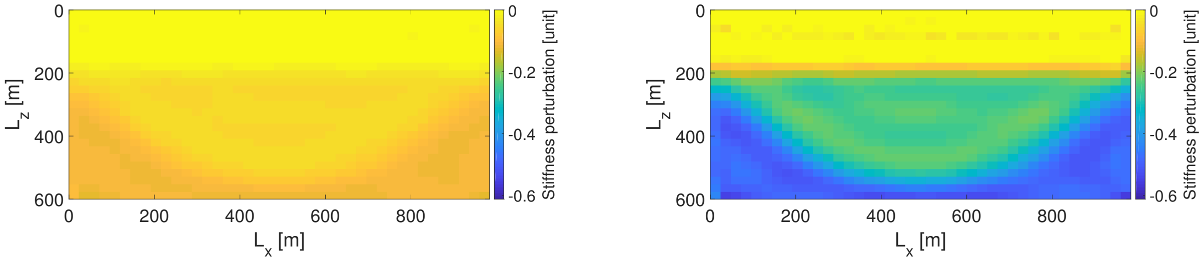

(c) ΔC_{55} **(d)** ΔC_{13}

Figure 5.6: The corresponding normalised stiffness perturbations of the syncline model, for the noisy data with an SNR of 40 dB. The colour map is the same for all parameters.

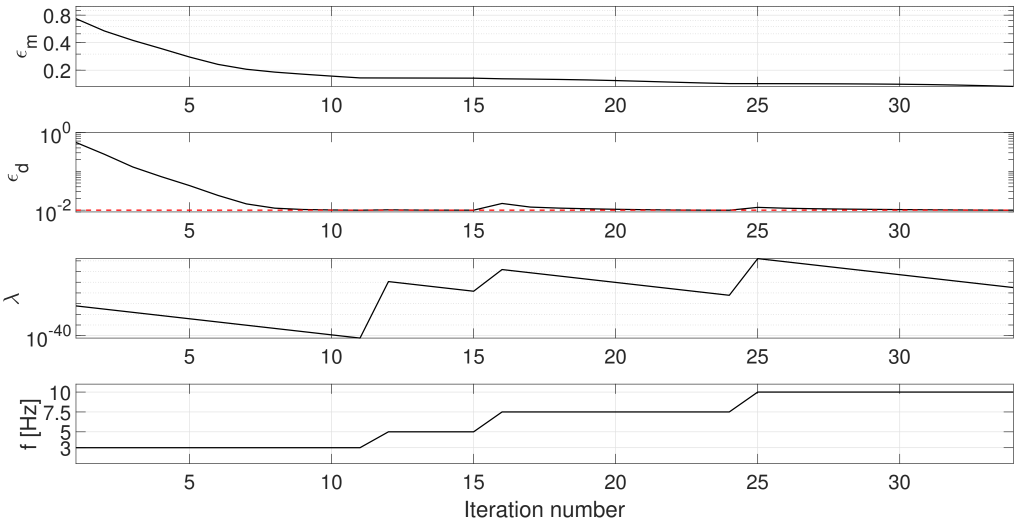

Figure 5.7: Performance of the DBI inversion for stiffness perturbation in the syncline model, for the noisy data with an SNR of 40 dB. Model error (ϵ_m) and residual data error (ϵ_d) depend on the iteration number. The data error converges to the noise-level (red dashed line). The last two plots show regularisation parameter (λ) and frequency (f), respectively.

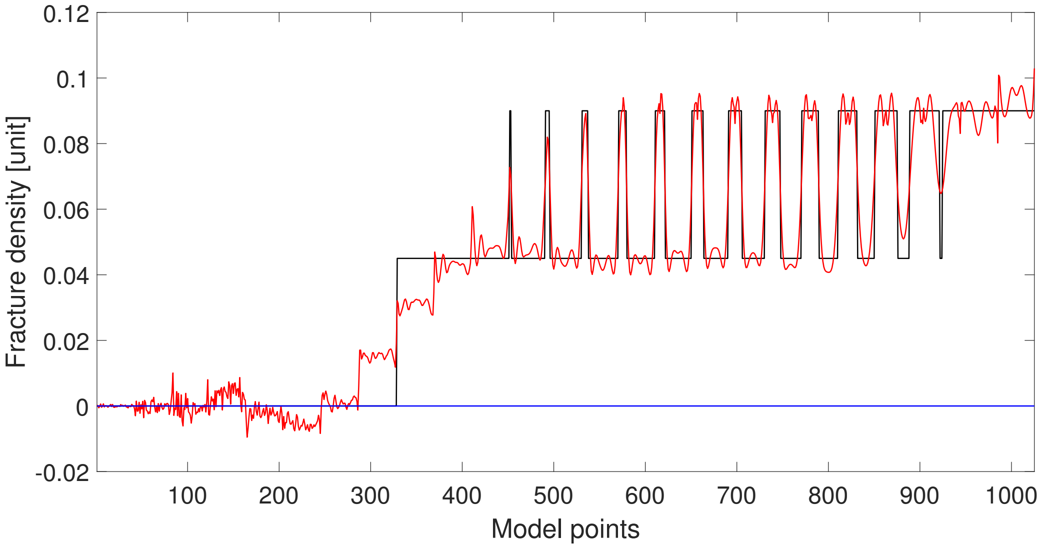

Figure 5.8: Model parameters of the DBI inversion result for the normalised stiffness perturbation in the syncline model, for the noisy data with an SNR of 40 dB. The starting model is shown as a blue line, the true model as a black line, and the inversion results as a red line.

5.3.2 Anticline Model

In this section, the inversion for fracture density in the anticline model case is performed. The anticline model was presented in Section 2.4.2, and the modelling was described in Section 3.4.2. The total number of grid blocks is 1107, and the dimension of the grid is 41x27. It should be noted that the number of sources is 11, while the number of receivers is 41. The reason for the reduction in the number of sources is to reduce the computational cost and was discussed in Section 3.4.2. The number of model parameters that are inverted is equal to the number of grid blocks.

The inverted fracture density model is presented in Fig. 5.9a, with the corresponding absolute error in Fig. 5.9b. By comparing the inverted anticline result to the true model in Fig. 2.7, it is quite obvious that the inversion is successful. The differences and contrasts between the layers are clear, and the anticline layer (in orange) is well retained after inversion. From the absolute error figure, it is evident that most of the grid blocks have absolute errors below 0.01 (1%). The upper layer has been correctly recovered, though some grid blocks in the anticline feature have a higher absolute error than 0.01.

The fracture density model in Fig. 5.9a combined with the t-matrix described in this chapter, yields the normalised stiffness perturbations shown in Fig. 5.10. By comparing these stiffness perturbations to their respective true counterparts, Fig. 3.8, a clear resemblance is seen. Note that the perturbation in C_{11} is minimal, as discussed in Section 2.4.2, and is mainly included for completeness. However, the three other parameters, C_{33}, C_{55}, and C_{13}, are almost identical to the true models in terms of the main (geological) features. The complex features, i.e. the two tilted layers and the anticline, are easy to make out in the stiffness perturbation models in Fig. 5.10.

The model error, data error, regularisation parameter, and frequency of this inversion is presented in Fig. 5.11. The inversion process, as seen in the figure, is very stable, and the model error reaches a quite low level. Each step of inversion for a specific frequency takes almost the same number of iterations. What was observed above can also be seen in Fig. 5.12, where the model vector comparison is displayed. Overall, the inverted fracture density result closely matches the correct fracture density of the anticline model. The total computation time for the inversion in case of noiseless data was 448 minutes, while the final model error was 0.095 (9.5%).

In the case of noisy data, with an SNR of 40 dB, the DBI fracture density inversion result for the anticline model, is shown in Fig. 5.13a. The different layers are still clearly visible, but more erroneous points are present in the corners. The absolute error, in Fig. 5.13b, confirms that there is an overall higher error in the noisy case. The “stairs” feature of the anticline is still quite difficult to recover, although the interface between the layers is visible.

The normalised stiffness perturbations are displayed in Fig. 5.14, which depend on Fig. 5.13a. The differences between these results and the noiseless results in Fig. 5.10, are few. The C_{55} parameter in Fig. 5.14c is notably worse in the upper right corner, mainly due to the low contrast between each layer. The other parameters, especially C_{33} and C_{13}, show a correct reconstruction compared to the true models.

Fig. 5.15 show the performance of the DBI inversion for fracture density in the anticline model. The convergence of the data error is quite fast in the noisy inversion, as the tolerance (noise-level) is set to 10^{-2}. However, the model error still reaches a very acceptable level (around 0.1). In Fig. 5.16, the inverted model vector is compared to both the starting and true models. The inverted fracture density result is very similar to the correct fracture density. There are more deviations than in the noiseless case, but overall most of the problematic points are close to the actual value. Finally, the total computation time for the inversion in case of noiseless data was 221 minutes, while the final model error was 0.119 (11.9%). Due to the stopping criteria (tolerance) being lower, in the case of noisy data, the computation time is shorter.

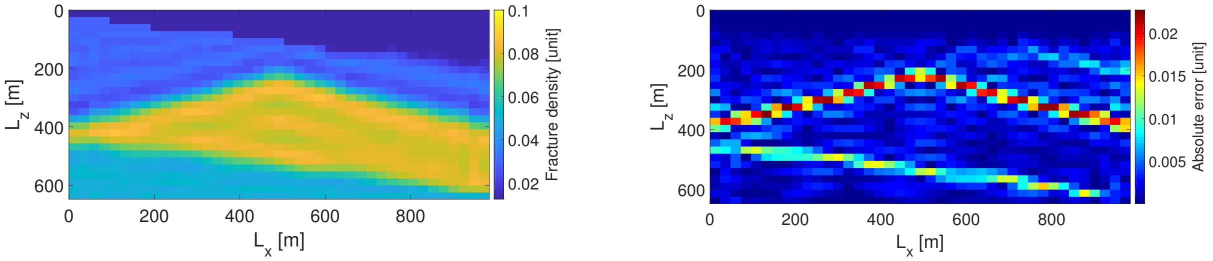

(a) Inverted fracture density **(b)** Absolute error

Figure 5.9: DBI inversion result for the anticline model, with inverted fractured density (left) and absolute error (right). The data is noiseless.

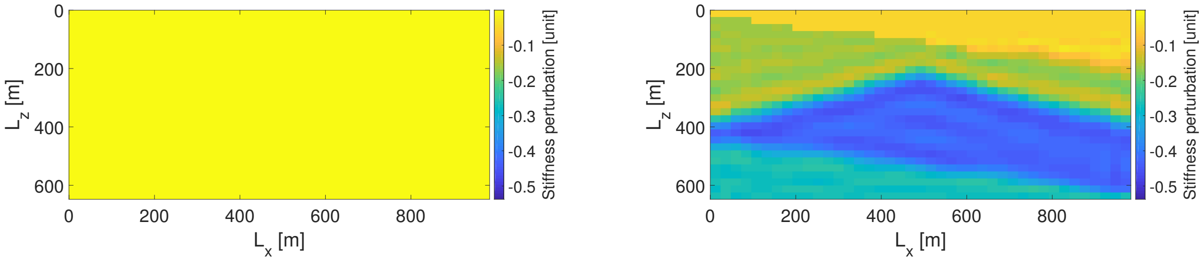

(a) ΔC_{11} **(b)** ΔC_{33}

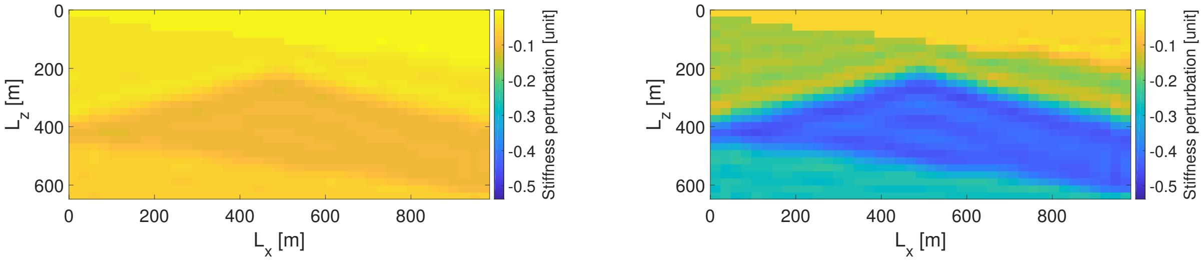

(c) ΔC_{55} **(d)** ΔC_{13}

Figure 5.10: The corresponding normalised stiffness perturbations of the anticline model, for the noiseless data. The colour map is the same for all parameters.

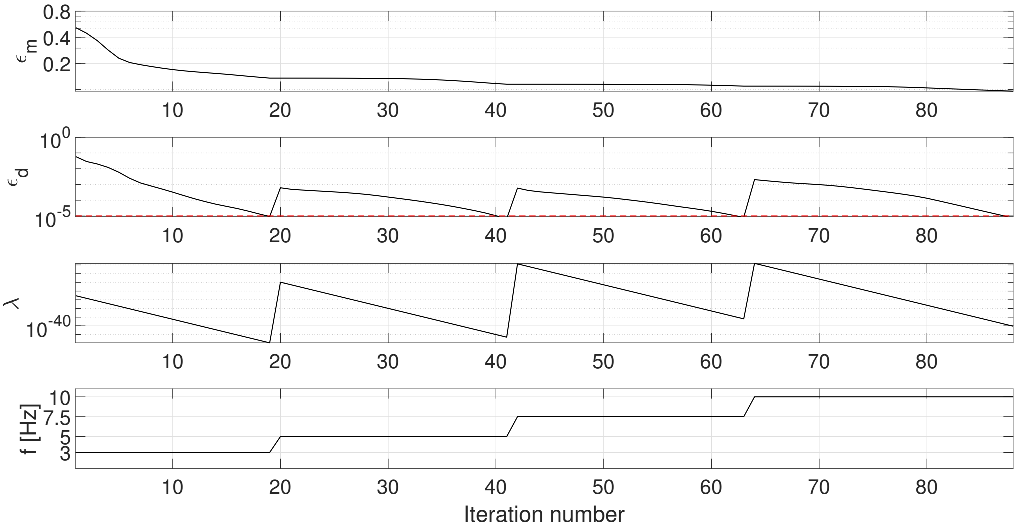

Figure 5.11: Performance of the DBI inversion for stiffness perturbation in the anticline model, for the noiseless data. Model error (ϵ_m) and residual data error (ϵ_d) depend on the iteration number. The equations for data and model error are given in Eqs. (4.35) and (4.36). The data error converges to the noise-level (red dashed line). The last two plots show regularisation parameter (λ) and frequency (f), respectively.

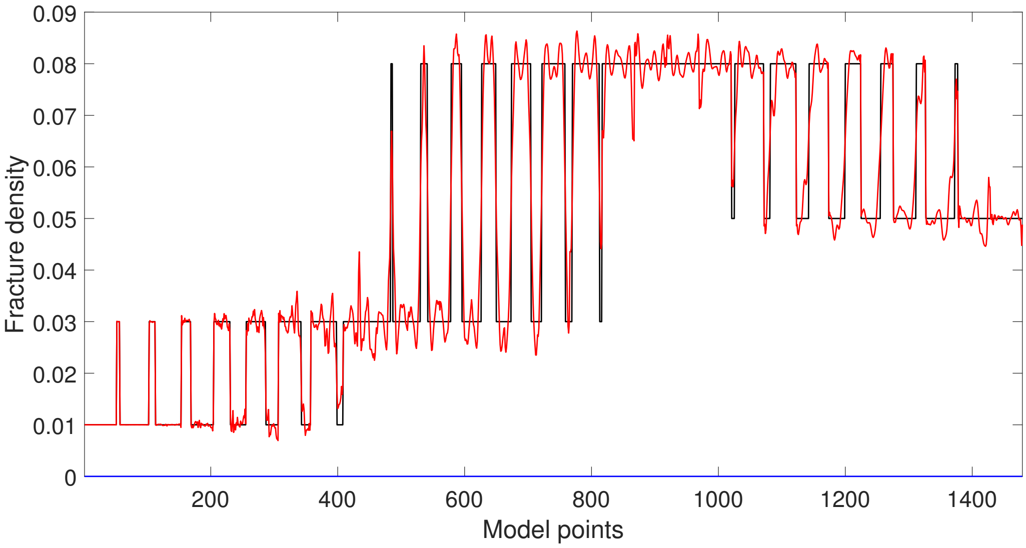

Figure 5.12: Model parameters of the DBI inversion result for the normalised stiffness perturbation in the anticline model, for the noiseless data. The starting model is shown as a blue line, the true model as a black line, and the inversion results as a red line.

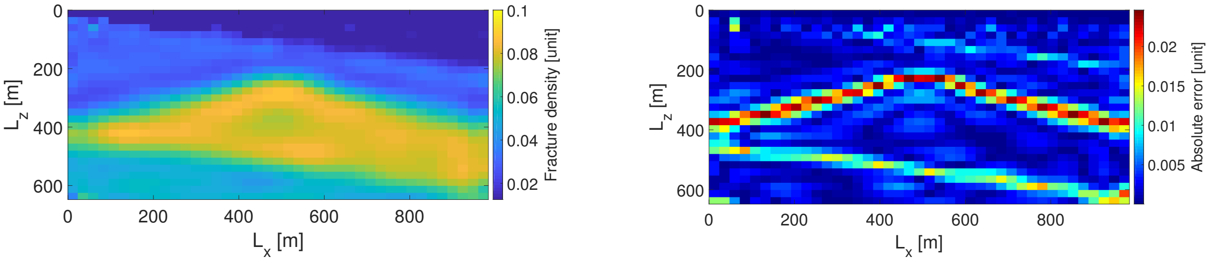

(a) Inverted fracture density **(b)** Absolute error

Figure 5.13: DBI inversion result for the anticline model, with inverted fractured density (left) and absolute error (right). The data is noisy with an SNR 40 dB.

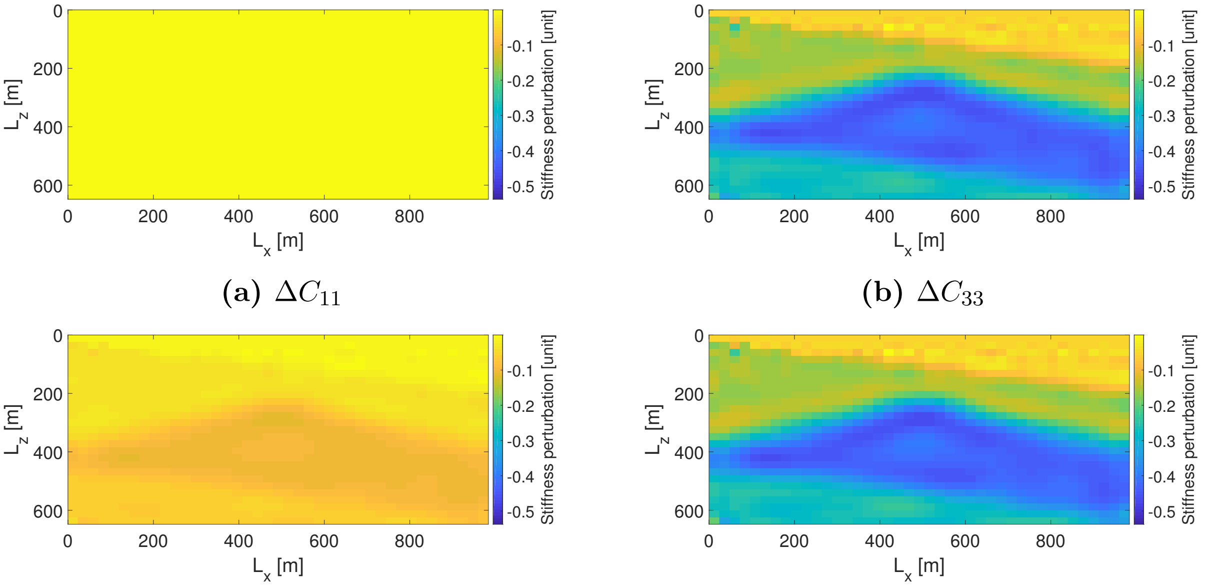

(a) ΔC_{11} **(b)** ΔC_{33}

(c) ΔC_{55} **(d)** ΔC_{13}

Figure 5.14: The corresponding normalised stiffness perturbations of the anticline model, for the noisy data with an SNR of 40 dB. The colour map is the same for all parameters.

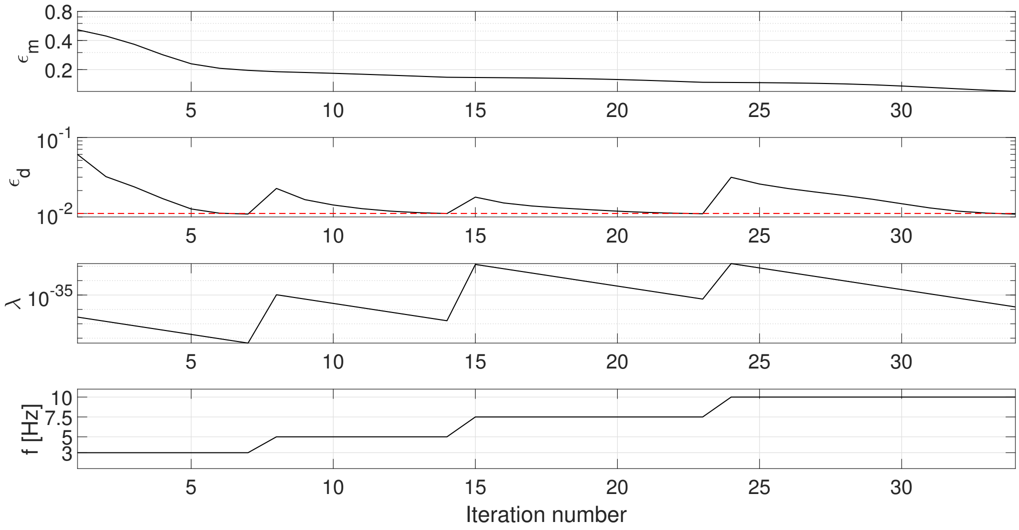

Figure 5.15: Performance of the DBI inversion for stiffness perturbation in the anticline model, for the noisy data of 40 dB SNR. Model error (ϵ_m) and residual data error (ϵ_d) depend on the iteration number. The data error converges to the noise-level (red dashed line). The last two plots show regularisation parameter (λ) and frequency (f), respectively.

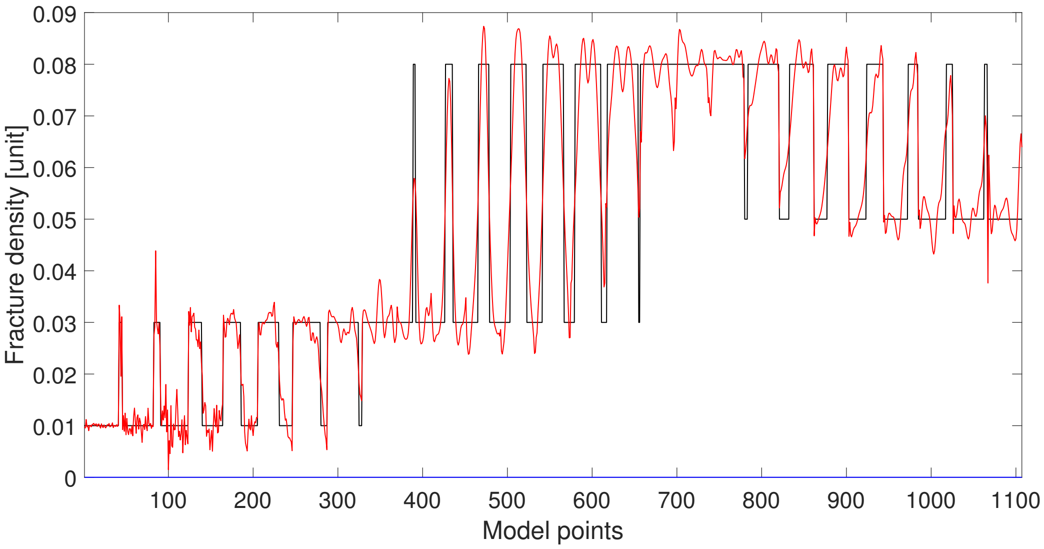

Figure 5.16: Model parameters of the DBI inversion result for the normalised stiffness perturbation in the anticline model, for the noisy data of 40 dB SNR. The starting model is shown as a blue line, the true model as a black line, and the inversion results as a red line.

5.4 Concluding Remarks

In this chapter, the DBI inversion method has successfully been applied to fracture density FWI. Isolated, horizontal fractures were represented by the t-matrix to provide a relationship between fractures and stiffness. The main points of the decomposition of the stiffness perturbation tensor was discussed, relating the B-matrix and t-matrix. Expressions for the scattered wavefield were presented, with an updated sensitivity matrix calculated in each iteration. Overall, the inversion results were promising.

Two distinctive models with different source-configurations have been modelled and inverted for, to analyse the quality of the fracture inversion. In the syncline model results, shown in Figs. 5.1a and 5.5a, and in the anticline model results, shown in Figs. 5.9a and 5.13a, it is evident that the DBI inversion method works well in the fracture density case. A few erroneous values, on the edge of the syncline and anticline models, can be observed in all of the results. However, these inaccuracies were more prominent when noise is present. All the respective stiffness perturbations were well recovered and overall match the true models quite closely. Interestingly, inverting for more than one frequency does not significantly impact the model error, as seen in Figs. 5.3, 5.7, 5.11, and 5.15. Thus, using only one frequency in both modelling and inversion could likely save computational time while still giving acceptable results.

Assessing the above results, the DBI inversion for fractures appear somewhat resistant to noise effects. There were few discrepancies when comparing the results with and without noise. Also, in the presence of more complex features and less sources, the results were still remarkable. Inverting for only parameter, e.g. fracture density, makes the inversion process more stable, and increases the accuracy. However, the quality of fracture-inversion will always depend on the rock physics model, and more specifically on the fracture model.

Chapter 6

Discussion and Conclusion

6.1 Discussion

The main objective of this work was to develop methods for non-linear elastic waveform inversion in the presence of fracture-induced anisotropy. Throughout this thesis, the theoretical background for elastic FWI in anisotropic media has been explained. The elastodynamic wave equation was solved via an equivalent integral-equation of the Lippmann-Schwinger type, as described in Section 3.3. Two methods, stiffness-based and fracture-based respectively, of inverting for stiffness perturbation have been employed with the DBI inversion scheme as described in Section 4.2. Fracture-inversion was extended to non-linear inversion, in Chapter 5. The results indicate that fracture density inversion is superior to stiffness-inversion.

The results for the stiffness-based DBI inversion, in Section 4.3, indicate that the introduction of noise can pose problems. Figs. 4.6 and 4.14 show a substantially higher absolute error in the presence of noise, compared to the noiseless results in Figs. 4.2 and 4.10. For the anticline model of Section 4.3.2, the inaccurate results are also a result of the reduction in the number of sources. The results are consistent with Tsvankin (2012), Kamath and Tsvankin (2016), and Jakobsen et al. (2017), in that inversion for the C_{13} stiffness parameter, as seen in Figs. 4.5d and 4.13d, is challenging. The C_{13} parameter, shown in Figs. 4.6d and 4.14d, is arguably the largest contribution to the high model error described in Table 4.1. The results for the C_{33} parameter, shown in Figs. 4.6b and 4.13b, show a good reconstruction of the true model. Primarily, the C_{33} is less affected by cross-talk and more susceptible to change due to horizontal fractures, as discussed in Section 2.4.1.

The results for the fracture density DBI inversion, as per Section 5.3.1, suggest that this approach is favourable when characterising a fractured reservoir. This is consistent with Bansal and Sen (2010) and Pilskog et al. (2015), that found fracture-based inversion to be highly flexible and efficient. From the stiffness perturbation results in Figs. 5.2, 5.6, 5.10, and 5.14, the main observation is that the results are excellent, independent of both noise-level and model type. The absolute errors of the noisy results, in Figs. 5.5b and 5.13b, are overall low. Both computation time and model error, per Table 5.1, are relatively low compared to the respective stiffness-inversion values in Table 4.1.

Most importantly, the fracture-based inversion seems to perform well in a more realistic case of random noise and less sources, which is consistent with Pilskog et al. (2015). This observation is evident when reviewing Figs. 5.9 and 5.13 for the anticline model. The inversion process is stable, for both noiseless and noisy data, due to the single model parameter (Pilskog et al., 2015). Inverting for a quite low number of frequencies gave good results, which is consistent with Bansal and Sen (2010).

These results agree with prior research by Bansal and Sen (2010) and Pilskog et al. (2015), that inversion for fractures in laterally varying fractured media achieves respectable results. The main difference compared to Bansal and Sen (2010) and Pilskog et al. (2015), is that in this work, the DBI inversion method was applied rather than ray-Born. Solving the non-linear inverse problem, gives a higher computational cost, although the results are more realistic by accounting for multiple scattering. Specifically for this work, Green's tensors are updated to account for the actual medium as opposed to using only the background (reference) Green's tensor as was used in Bansal and Sen (2010) and Pilskog et al. (2015).

The main implication of the stiffness-based inversion results, discussed above, is that the parametrisation of seismic anisotropy is crucial. Jakobsen et al. (2017) argues that the anisotropic FWI has problems with cross-talk effects, as discussed in Section 2.2. Figs. 4.13d and 4.14d clearly show that the C_{13} parameter is incorrectly resolved in the DBI inversion of Section 4.3.2, which is consistent with Kamath and Tsvankin (2016). For the fracture-based inversion, the C_{13} parameter in Fig. 5.14d is considerately better than for the stiffness-based inversion. Practically, this implies that it is better to use fracture-based inversion for reservoirs.

One may argue that the elastic FWI that was used in this thesis, is not strictly FWI since only parts of the wavefield frequency-content is accounted for in the computations. According to Pratt (1999) and Bansal and Sen (2010), however, a few frequencies can sufficiently account for the source wavelet, while providing reasonable results. Therefore, it was considered sufficient to only use a set of four frequencies in this thesis. Based on recent research on anisotropic elastic FWI, the terminology used in this work is consistent (e.g. Zhang et al., 2017; Jakobsen et al., 2020b; Huang et al., 2020a).

Due to the lack of required computational power, the models were reduced in size to overcome memory constraints. Iterative methods, like the Born-Neumann series, could have calculated the full integral-equation solution, in Section 3.3, more efficiently. As the Born-Neumann series has convergence issues (Osnabrugge et al., 2016), recent research has been done on solving the Lippmann-Schwinger scattering series by renormalisation and homotopy methods (see Jakobsen et al., 2020a,c). Besides, as mentioned in Chapter 1, the 3D Green's function, which is more computationally intensive, was used for 2D models. As the modified 3D Green's function was given explicitly in Jakobsen et al. (2020b), this leads to the most straightforward implementation. Additionally, better results could likely have been obtained using a broader model, according to Zhang et al. (2017).

The main limitation of fracture density inversion is the dependence on a good rock physics model (fracture model). Fractures were horizontally aligned, see Section 2.4, which is based on the assumption that the orientation of fractures is known. According to Sayers (2009), fractured reservoirs contain more than one fracture orientation (type), and not accounting for this may lead to misleading results. For the computation of stiffness perturbations in Section 5.3.1, only the first-order correction, as per Section 2.3.3, was used. This approximation is reasonable for fracture densities below 0.1, as stated by Cheng (1993) and Jakobsen et al. (2003a). In principle, a different fracture model and approach, than the t-matrix inclusion model, could have been used in this thesis. The linear-slip theory (Schoenberg, 1980), described in Section 2.3.2, is an example of a fracture model that has been used recently (Zhang et al., 2017).

6.2 Conclusion

By further developing methods for non-linear FWI in elastic anisotropic media, this thesis has shown how two DBI inversion-methods for fractures can be implemented. Information of geological interest and estimation of anisotropic permeability, that is relevant to reservoir characterisation, can be obtained by inverting for fracture parameters rather than stiffness parameters. The integral-equation approach, combined with the elastic FWI for anisotropic media provides a powerful tool for high-resolution seismic imaging.

The results indicate that the fracture-inversion is advantageous compared to stiffness-inversion in fractured media. Four stiffness parameters can be controlled using only one fracture parameter, reducing the complexity of multi-parameter FWI to a single-parameter problem. Consequently, this may lead to lower computational cost and higher accuracy.

The research of this thesis clearly illustrates the importance of seismic anisotropy when it comes to the characterisation of fractures, in addition to an adequate fracture model.

6.3 Future Work

To better understand the implications of these results, future research could address the following:

- Solving Lippmann-Schwinger with Fast Fourier Transform (FFT), as was mentioned by Huang et al. (2020a) and Jakobsen et al. (2020c).
- Using the Gassmann-consistent FWI for fracture parameters, as demonstrated by Jakobsen and Pilskog (2016).
- Applying the theory of this work to an HTI medium with vertical fractures.
- Extending the non-linear inversion theory to permeability tensors (Jakobsen, 2006; Shahraini et al., 2011).

FFT is an algorithm applying a fast method of the well-known discrete Fourier transform. The Lippmann-Schwinger equation in Eq. (3.17), is a convolution in the frequency-domain, which translates to multiplication in the Fourier domain (Jakobsen et al., 2020a). By using the FFT algorithm, memory used can be reduced, and the implementation will be more efficient (Jakobsen et al., 2020c).

By using the anisotropic Gassmann relations, the dry fractured medium could be saturated with any fluid. Additionally, these fractures could be partially saturated with a fluid, based on Jin et al. (2018).

Vertical fractures are more realistic in naturally fractured reservoirs (e.g. Schoenberg and Sayers, 1995; Bakulin et al., 2000), and can be implemented by extending this work to HTI media. Ideally, more than one fracture set should be modelled to represent different shapes and orientations (Sayers, 2009).

The theory of the t-matrix for fractures, in Section 2.3.3, can be applied to permeability tensors similarly to stiffness tensors (Jakobsen, 2006; Shahraini et al., 2011). The effective permeability tensor quantifies the materials ability for fluid to flow (Guéguen and Palciauskas, 1994; Mavko et al., 2009). Permeability is related to both pores and fractures, as connected inclusions increase permeability.

Appendices

A Rock Physics G-tensor

The G-tensor of phase r, $\mathbf{G}^{(r)}$, can be written as (Torquato and Haslach Jr, 2002; Jakobsen and Johansen, 2005)

$$\mathbf{G}^{(r)} = -\mathbf{S}^{(r)} : \mathbf{S}^{(0)}, \tag{A.1}$$

where $\mathbf{S}^{(r)}$ is the compliance tensor of the ellipsoid (Eshelby, 1957), and $\mathbf{S}^{(0)}$ is the reference compliance tensor given by $\mathbf{S}^{(0)} = \left(\mathbf{C}^{(0)}\right)^{-1}$.

For an isotropic matrix with spherical inclusions of aspect ratio α_c and a vertical symmetry axis, the elliptic integral can be evaluated analytically (Jakobsen and Johansen, 2005).

Assuming only one phase of inclusions ($r \equiv 1$), the components of the compliance tensor, S_{IJ}, are given by (Torquato and Haslach Jr, 2002; Jakobsen and Johansen, 2005)

$$S_{11} = S_{22} = \frac{3}{8(1-\nu)} \frac{\alpha_c^2}{\alpha_c^2 - 1} + \frac{1}{4(1-\nu)} \left[1 - 2\nu - \frac{9}{4(\alpha_c^2 - 1)} \right] q \,, \tag{A.2}$$

$$S_{33} = \frac{1}{2(1-\nu)} \left\{ 1 - 2\nu + \frac{3\alpha_c^2 - 1}{\alpha_c^2 - 1} - \left[1 - 2\nu + \frac{3\alpha_c^2 - 1}{\alpha_c^2 - 1} \right] q \right\} \,, \tag{A.3}$$

$$S_{12} = S_{21} = \frac{1}{4(1-\nu)} \left\{ \frac{\alpha_c^2}{2(\alpha_c^2 - 1)} - \left[1 - 2\nu + \frac{3}{4(\alpha_c^2 - 1)} \right] q \right\} \,, \tag{A.4}$$

$$S_{13} = S_{23} = \frac{1}{2(1-\nu)} \left\{ \frac{-\alpha_c^2}{\alpha_c^2 - 1} + \frac{1}{2} \left[\frac{3\alpha_c^2}{\alpha_c^2 - 1} - (1 - 2\nu) \right] q \right\} \,, \tag{A.5}$$

$$S_{31} = S_{32} = \frac{1}{2(1-\nu)} \left\{ 2\nu - 1 - \frac{1}{\alpha_c^2 - 1} + \left[1 - 2\nu + \frac{3}{2(\alpha_c^2 - 1)} \right] q \right\} \,, \tag{A.6}$$

$$S_{66} = \frac{1}{4(1-\nu)} \left\{ \frac{\alpha_c^2}{2(\alpha_c^2 - 1)} + \left[1 - 2\nu - \frac{3}{4(\alpha_c^2 - 1)} \right] q \right\} \,, \tag{A.7}$$

$$S_{44} = S_{55} = \frac{1}{4(1-\nu)} \left\{ 1 - 2\nu - \frac{\alpha_c^2 + 1}{\alpha_c^2 - 1} - \frac{1}{2} \left[1 - 2\nu - \frac{3(\alpha_c^2 + 1)}{\alpha_c^2 - 1} \right] q \right\} \,, \tag{A.8}$$

where ν is Poisson's ratio and q is a constant. Poisson's ratio is given by (Mavko et al., 2009)

$$\nu = \frac{3\kappa - 2\mu}{2(3\kappa + \mu)} \,, \tag{A.9}$$

where $\mu = \frac{C_{44}^{(0)}}{2}$ and $\kappa = C_{11}^{(0)} - \frac{4}{3}\mu$.

The constant q, in Eqs. (A.2) - (A.8), is given by (Jakobsen and Johansen, 2005)

$$q = \frac{\alpha_c}{(1 - \alpha_c)^{\frac{3}{2}}} \left[\cos^{-1}\alpha_c - \alpha_c (1 - \alpha_c^2)^{\frac{1}{2}} \right] \,, \tag{A.10}$$

when $\alpha_c \leq 1$.

In this thesis, the condition of aspect ratio being lower than one will always be satisfied. This is due to inclusions being cracks/fractures, with an aspect ratio commonly in the range $0.001 \leq \alpha_c \leq 0.05$. The compliance tensor, S_{IJ}, in this case, can be written as (Mavko et al., 2009):

$$S = \begin{bmatrix} S_{11} & S_{12} & S_{13} & 0 & 0 & 0 \\ S_{12} & S_{11} & S_{13} & 0 & 0 & 0 \\ S_{31} & S_{31} & S_{33} & 0 & 0 & 0 \\ 0 & 0 & 0 & 2S_{44} & 0 & 0 \\ 0 & 0 & 0 & 0 & 2S_{44} & 0 \\ 0 & 0 & 0 & 0 & 0 & 2S_{66} \end{bmatrix} , \tag{A.11}$$

where the Kelvin notation for compliance is used. The strain Green's tensor can then be calculated with Eq. (A.1).

The equations above can be simplified for spheres (spherical pores), where $\alpha_c = 1$ and $q = \frac{2}{3}$. In consequence, the compliance tensor can be written as (Jakobsen and Johansen, 2005)

$$S_{ijkl} = \frac{5\nu - 1}{15(1-\nu)}\delta_{ij}\delta_{kl} + \frac{4-5\nu}{15(1-\nu)}\left(\delta_{ik}\delta_{jl} + \delta_{il}\delta_{jk}\right) , \tag{A.12}$$

where the Kronecker-delta δ_{kl} is defined as

$$\delta_{kl} = \left\{ \begin{matrix} 0, \text{ if } k \neq l \\ 1, \text{ if } k = l \end{matrix} \right\} . \tag{A.13}$$

Flat, compliant Hudson cracks are defined with $\alpha_c \to 0$ and $q \to 0$. The only non-zero compliance tensors are given by (Jakobsen and Johansen, 2005)

$$S_{33} = 1 , \tag{A.14}$$

$$S_{31} = S_{32} = \frac{\nu}{1-\nu} , \tag{A.15}$$

and

$$S_{55} = S_{44} = \frac{1}{2} . \tag{A.16}$$

B Reference Green's Function and Derivatives

B.1 Leading-term Green's Function

The exact Green's function, **G**, for a homogeneous and isotropic medium, can be represented by a ray series of three terms (Jakobsen et al., 2020b). This ray series has two parts, one for P-waves and one for S-waves. The far-field approximation for P- and S-waves will be used in this thesis, as it is the most relevant (Snieder, 2002). This approximation can be seen as a high frequency approximation (Červený, 2005), expressed by the zero-order term (Eisner and Pšenčík, 1996; Madariaga, 2007; Jakobsen et al., 2020b). Also, the far-field approximation works well when compared to the exact Green's function (Eisner and Pšenčík, 1996).

By considering a Green's function between a source, $\mathbf{x_s}$, and a receiver, $\mathbf{x_r}$, the Green's function can be represented by the contribution from both P- and S-waves. Consequently, the homogeneous isotropic Green's function can be written as (Eisner and Pšenčík, 1996; Snieder, 2002; Červený, 2005; Madariaga, 2007; Jakobsen et al., 2020b):

$$G_{kl}(r,\omega) = G^P_{kl}(r,\omega) + G^S_{kl}(r,\omega) \ , \tag{B.1}$$

where

$$G^P_{kl}(r,\omega) \sim \frac{A(r)}{r}\left(N_k N_l + \frac{\alpha}{\mathrm{i}\omega r} e_{Jk} e_{Jl}\right) \ , \tag{B.2}$$

and

$$G^S_{kl}(r,\omega) \sim \frac{B(r)}{r}\left(e_{Jk} e_{Jl} + \frac{\beta}{\mathrm{i}\omega r} N_k N_l\right) \ . \tag{B.3}$$

In Eqs. (B.2) and (B.3), α and β are P- and S-wave velocities, r is the source-receiver distance, **N** is the normal unit vector and vectors e_{Jk} and e_{Jl} are projections of a unit vector (Eisner and Pšenčík, 1996). Lower-case indices run from 1 to 3, upper-case indices run from 1 to 2. The Einstein summation rule (Einstein, 1916) is applied. The normal-vector can be defined as

$$N_i = \frac{n_i}{r}, \tag{B.4}$$

where $r = \|\mathbf{n}\|$ and $\mathbf{n} = \mathbf{x_r} - \mathbf{x_s}$.

The terms $A(r)$ and $B(r)$, in Eqs. (B.2) and (B.3), are defined as

$$A(r) = \frac{\exp(\mathrm{i}\omega r/\alpha)}{4\pi\rho\alpha^2} \ , \tag{B.5}$$

and

$$B(r) = \frac{\exp(\mathrm{i}\omega r/\beta)}{4\pi\rho\beta^2} \ . \tag{B.6}$$

B.2 First-Order Spatial Derivatives of Green's Function

P-wave

By focusing on the P-wave part, G^P_{kl}, Eq. (B.2) can be rewritten as (Jakobsen et al., 2020b):

$$G^P_{kl}(r,\omega) \sim \frac{A(r)}{r^2}\left[a\delta_{kl} + \frac{x_k x_l}{r}\left(1-\frac{a}{r}\right)\right] , \tag{B.7}$$

where

$$a = \alpha/\mathrm{i}\omega , \tag{B.8}$$

and the Kronecker delta, δ_{kl}, is given in Eq. (A.13).

To find the first derivative of the P-wave Green's function, G^P_{kl}, the following notation is introduced to simplify Eq. (B.7):

$$X(r) = A(r) , \qquad Y_{kl}(r) = a\delta_{kl} + \frac{x_k x_l}{r}\left(1-\frac{a}{r}\right) , \qquad Z(r) = r^2 . \tag{B.9}$$

This simplifies Eq. (B.7) to

$$G^P_{kl} = \frac{XY_{kl}}{Z} , \tag{B.10}$$

where G^P_{kl} depend on radial distance, r, and angular frequency, ω.

The first spatial derivative of G^P_{kl}, can be obtained from Eq. (B.10) by differentiation:

$$G^P_{kl,i} = \frac{\left(X_{,i}Y_{kl} + XY_{kl,i}\right)Z - XY_{kl}Z_{,i}}{Z^2} , \tag{B.11}$$

where the comma notation for derivatives is defined by $G_{kl,i} = \frac{\partial}{\partial x_i}G_{kl}$.

The first spatial derivatives of X, Y_{kl} and Z are given by:

$$X_{,i} = A_{,i} = A\frac{\mathrm{i}\omega x_i}{\alpha r} = \frac{A}{a}\frac{x_i}{r} , \tag{B.12}$$

$$Y_{kl,i} = \frac{\delta_{ik}x_l + \delta_{il}x_k}{r}\left(1-\frac{a}{r}\right) - \frac{x_k x_l x_i}{r^3}\left(1-2\frac{a}{r}\right) , \tag{B.13}$$

$$Z_{,i} = 2x_i . \tag{B.14}$$

By Madariaga (2007), the expression in Eq. (B.11) can be written as:

$$G^P_{kl,i}(r,\omega) = \frac{\mathrm{i}\omega}{4\pi r\rho\alpha^3}\mathcal{P}_{kli}\exp(\mathrm{i}\omega r/\alpha) , \tag{B.15}$$

where the P-wave coefficient, $\mathcal{P}$, is defined as $\mathcal{P}_{kli} \equiv n_k n_l n_i$ (Madariaga, 2007). The normal unit vector, $\mathbf{n}$, is given in Eq. (B.4).

S-wave

For the S-wave part, G^S_{kl}, Eq. (B.3) can be simplified to

$$G^S_{kl}(r,\omega) \sim \frac{B(r)}{r}\left[\delta_{kl} + \frac{x_k x_l}{r^2}\left(\frac{2b}{r} - 1\right)\right] , \tag{B.16}$$

where

$$b = \beta/\mathrm{i}\omega . \tag{B.17}$$

Introducing the following notation for the S-wave part:

$$V(r) = B(r) , \qquad W_{kl}(r) = \delta_{kl} + \frac{x_k x_l}{r^2}\left(\frac{2b}{r} - 1\right) , \qquad U(r) = r . \tag{B.18}$$

Equation (B.16) can then be rewritten as

$$G^S_{kl} = \frac{VW_{kl}}{U} . \tag{B.19}$$

The derivative of Eq. (B.19) is then

$$G^S_{kl,i} = \frac{\left(V_{,i}W_{kl} + VW_{kl,i}\right)U - VW_{kl}U_{,i}}{U^2} \tag{B.20}$$

The first spatial derivatives of V, W_{kl} and U are given by:

$$V_{,i} = B_{,i} = B\frac{\mathrm{i}\omega x_i}{\beta r} = \frac{B}{b}\frac{x_i}{r} , \tag{B.21}$$

$$W_{kl,i} = \frac{\delta_{ik}x_l + \delta_{il}x_k}{r^2}\left(\frac{2b}{r} - 1\right) - 2\frac{x_k x_l x_i}{r^4}\left(\frac{3b}{r} - 1\right) , \tag{B.22}$$

$$U_{,i} = \frac{x_i}{r} . \tag{B.23}$$

Similarly to Eq. (B.15), an expression for the S-wave part in Eq. (B.20) can be written as

$$G^S_{kl,i}(r,\omega) = \frac{\mathrm{i}\omega}{4\pi r\rho\beta^3}\mathcal{S}_{kli}\exp(\mathrm{i}\omega r/\alpha) , \tag{B.24}$$

where the S-wave coefficient, $\mathcal{S}$, is defined as $\mathcal{S}_{kli} \equiv \delta_{kl}n_i - n_k n_l n_i$ (Madariaga, 2007). The normal unit vector, $\mathbf{n}$, is given in Eq. (B.4).

M-tensor

The third-rank Green's function can be referred to as the M-tensor and depends on the first spatial derivate of the Green's function. From Eq. (B.1), this Green's function can be expressed as

$$G_{kl,i}(r,\omega) = G^P_{kl,i}(r,\omega) + G^S_{kl,i}(r,\omega) \ , \tag{B.25}$$

where $G^P_{kl,i}(r,\omega)$ and $G^S_{kl,i}(r,\omega)$ can be calculated with Eqs. (B.15) and (B.24), respectively.

The M-tensor in Eq. (3.15) can then be expressed as (Jakobsen et al., 2020b)

$$M_{kli}(r,\omega) = -\frac{1}{2}\left[G_{kl,i}(r,\omega) + G_{ki,l}(r,\omega)\right] \ . \tag{B.26}$$

B.3 Second-Order Spatial Derivatives of Green's Function

P-wave

Continuing from the previous section, an expression for the second derivative of Green's function, G_{kl}, can be derived. Considering the P-wave part of the second spatial derivate of G^P_{kl} again. The derivative of Eq. (B.11) is given by

$$\begin{aligned} G^P_{kl,ij} = & \frac{X_{,ij}Y_{kl} + XY_{kl,ij} + X_{,i}Y_{kl,j} + X_{,j}Y_{kl,i}}{Z} \\ & - \frac{Z_{,ij}XY_{kl} + X_{,i}Z_{,j}Y_{kl} + Y_{kl,i}Z_{,j}X + X_{,j}Z_{,i}Y_{kl} + Y_{kl,j}Z_{,i}X}{Z^2} + 2\frac{Z_{,i}Z_{,j}XY_{kl}}{Z^3} \ . \end{aligned} \tag{B.27}$$

The second spatial derivatives of X, Y_{kl} and Z in Eq. (B.9) are given by Eqs. (B.28) - (B.30).

$$X_{,ij} = A_{,ij} = A\left[\frac{\mathrm{i}\omega}{\alpha r}\left(\delta_{ij} - \frac{x_i x_j}{r^2}\right) - \frac{\omega^2 x_i x_j}{\alpha^2 r^2}\right] = \frac{A}{a}\left[\frac{1}{r}\left(\delta_{ij} - \frac{x_i x_j}{r^2}\right) + \frac{x_i x_j}{a r^2}\right] \ , \tag{B.28}$$

$$\begin{aligned} Y_{kl,ij} = & \frac{\delta_{ik}\delta_{jl} + \delta_{il}\delta_{jk}}{r}\left(1 - \frac{a}{r}\right) \\ & - \frac{\delta_{ik}x_l x_j + \delta_{il}x_j x_k + \delta_{jk}x_l x_i + \delta_{jl}x_k x_i + \delta_{ij}x_k x_l}{r^3}\left(1 - 2\frac{a}{r}\right) + \frac{x_k x_l x_i x_j}{r^5}\left(3 - 8\frac{a}{r}\right) \ , \end{aligned} \tag{B.29}$$

$$Z_{,ij} = 2\delta_{ij} \ . \tag{B.30}$$

S-wave

For the S-wave part, G^P_{kl}, the derivative of Eq. (B.20) is given by

$$
\begin{aligned}
G^S_{kl,ij} = & \frac{V_{,ij}W_{kl} + VW_{kl,ij} + V_{,i}W_{kl,j} + V_{,j}W_{kl,i}}{U} \\
& - \frac{U_{,ij}VW_{kl} + V_{,i}U_{,j}W_{kl} + U_{,j}W_{kl,i}V + V_{,j}U_{,i}W_{kl} + W_{kl,j}U_{,i}V}{U^2} + 2\frac{U_{,i}U_{,j}VW_{kl}}{U^3} \ .
\end{aligned}
\tag{B.31}
$$

The second spatial derivatives of V, W_{kl} and U in Eq. (B.18) are given Eqs. (B.32) - (B.34).

$$
V_{,ij} = B_{,ij} = B\left[\frac{\mathrm{i}\omega}{\beta r}\left(\delta_{ij} - \frac{x_i x_j}{r^2}\right) - \frac{\omega^2 x_i x_j}{\beta^2 r^2}\right] = \frac{B}{b}\left[\frac{1}{r}\left(\delta_{ij} - \frac{x_i x_j}{r^2}\right) + \frac{x_i x_j}{b r^2}\right] \ , \tag{B.32}
$$

$$
\begin{aligned}
W_{kl,ij} = & \frac{\delta_{ik}\delta_{jl} + \delta_{il}\delta_{jk}}{r^2}\left(\frac{2b}{r} - 1\right) \\
& - 2\frac{\delta_{ik}x_l x_j + \delta_{il}x_j x_k + \delta_{jk}x_l x_i + \delta_{jl}x_k x_i + \delta_{ij}x_k x_l}{r^4}\left(\frac{3b}{r} - 1\right) + \frac{2x_k x_l x_i x_j}{r^6}\left(\frac{15b}{r} - 4\right) \ ,
\end{aligned}
\tag{B.33}
$$

$$
U_{,ij} = \frac{1}{r}\left(\delta_{ij} - \frac{x_i x_j}{r^2}\right) \ . \tag{B.34}
$$

Γ-tensor

The fourth-rank Green's function can be referred to as the Γ-tensor and depends on the second spatial derivate of the Green's function. From Eq. (B.25), this Green's function can be expressed as

$$
G_{kl,ij}(r,\omega) = G^P_{kl,ij}(r,\omega) + G^S_{kl,ij}(r,\omega) \ . \tag{B.35}
$$

The Γ-tensor in Eq. (3.18), can then be calculated by using Eq. (B.35).

References

Abubakar, A., Pan, G., Li, M., Zhang, L., Habashy, T., and van den Berg, P. (2011). Three-dimensional seismic full-waveform inversion using the finite-difference contrast source inversion method: 3D seismic full-waveform inversion. *Geophysical Prospecting*, 59:874–888. (Cited on page 3.)

Ali, A. and Jakobsen, M. (2011a). On the accuracy of Rüger's approximation for reflection coefficients in HTI media: implications for the determination of fracture density and orientation from seismic AVAZ data. *Journal of Geophysics and Engineering*, 8(2):372–393. (Cited on pages 1, 11, 12, and 21.)

Ali, A. and Jakobsen, M. (2011b). Seismic characterization of reservoirs with multiple fracture sets using velocity and attenuation anisotropy data. *Journal of Applied Geophysics*, 75(3):590–602. (Cited on pages 1 and 14.)

Ali, A., Shahraini, A., and Jakobsen, M. (2011). Improved characterization of fault zones by quantitative integration of seismic and production data. *Journal of Geophysics and Engineering*, 8(2):259–274. (Cited on page 11.)

Alkhalifah, T. and Choi, Y. (2012). Taming waveform inversion non-linearity through phase unwrapping of the model and objective functions. *Geophysical Journal International*, 191(3):1171–1178. Publisher: Blackwell Publishing Ltd Oxford, UK. (Cited on page 3.)

Aster, R. C., Borchers, B., and Thurber, C. H. (2018). *Parameter estimation and inverse problems*. Elsevier. (Cited on pages 47, 48, 49, 57, and 58.)

Auld, B. A. (1990). *Acoustic Fields and Waves in Solids*. Kriege, Malabar, Fla, 2nd ed. edition. (Cited on pages 7, 8, 10, 33, and 34.)

Avseth, P., Mukerji, T., and Mavko, G. (2010). *Quantitative seismic interpretation: Applying rock physics tools to reduce interpretation risk*. Cambridge university press. (Cited on page 18.)

Bakulin, A., Grechka, V., and Tsvankin, I. (2000). Estimation of fracture parameters from reflection seismic data—Part I: HTI model due to a single fracture set. *GEOPHYSICS*, 65(6):1788–1802. (Cited on pages 12, 13, and 94.)

Bansal, R. and Sen, M. K. (2010). Ray-Born inversion for fracture parameters. *Geophysical Journal International*, 180(3):1274–1288. (Cited on pages 1, 3, 4, 12, 13, 21, 28, 73, 74, and 92.)

Batzle, M. L. and Simmons, G. (1976). Microfractures in rocks from two geothermal areas. *Earth and Planetary Science Letters*, 30(1):71–93. (Cited on page 1.)

Berryman, J. G. (1999). Origin of Gassmann's equations. *GEOPHYSICS*, 64(5):1627–1629. (Cited on page 17.)

Bleistein, N., Cohen, J. K., Stockwell Jr, J. W., and Berryman, J. (2001). Mathematics of Multidimensional Seismic Imaging, Migration, and Inversion. Interdisciplinary Applied Mathematics, Vol 13. *Appl. Mech. Rev.*, 54(5):B94–B96. (Cited on page 28.)

Bredesen, K., Jensen, E. H., Johansen, T. A., and Avseth, P. (2015). Quantitative seismic interpretation using inverse rock physics modelling. *Petroleum Geoscience*, 21(4):271–284. (Cited on page 16.)

Brown, R. J. and Korringa, J. (1975). On the dependence of the elastic properties of a porous rock on the compressibility of the pore fluid. *Geophysics*, 40(4):608–616. (Cited on pages 9, 13, 16, and 17.)

Carcione, J. M., Herman, G. C., and ten Kroode, A. P. E. (2002). Seismic modeling. *GEOPHYSICS*, 67(4):1304–1325. (Cited on pages 27, 28, and 74.)

Cheng, C. H. (1993). Crack models for a transversely isotropic medium. *Journal of Geophysical Research: Solid Earth*, 98(B1):675–684. (Cited on pages 15, 20, and 93.)

Chew, W. and Wang, Y. (1990). Reconstruction of two-dimensional permittivity distribution using the distorted Born iterative method. *IEEE Transactions on Medical Imaging*, 9(2):218–225. (Cited on page 50.)

Chew, W. C., Tong, M. S., and Hu, B. (2008). Integral equation methods for electromagnetic and elastic waves. *Synthesis Lectures on Computational Electromagnetics*, 3(1):1–241. Publisher: Morgan & Claypool Publishers. (Cited on page 28.)

Ciric, I. and Qin, Y. (1997). Self-adaptive selection of the regularization parameter for electromagnetic imaging. *IEEE Transactions on Magnetics*, 33(2):1556–1559. (Cited on pages 57, 58, 60, and 76.)

Constable, S. C., Parker, R. L., and Constable, C. G. (1987). Occam's inversion: A practical algorithm for generating smooth models from electromagnetic sounding data. *GEOPHYSICS*, 52(3):289–300. (Cited on pages 47 and 57.)

Dellinger, J., Vasicek, D., and Sondergeld, C. (1998). Kelvin Notation for Stabilizing Elastic-Constant Inversion. *Revue de l'Institut Français du Pétrole*, 53(5):709–719. (Cited on pages 8 and 10.)

Einstein, A. (1916). The foundation of the general theory of relativity. *Annalen der Physik*, 49(7):769–822. Publisher: Dover New York. (Cited on pages 36, 53, and 99.)

Eisner, L. and Pšenčík, I. (1996). Computation of additional components of the first-order ray approximation in isotropic media. *pure and applied geophysics*, 148(1-2):227–253. (Cited on page 99.)

Eshelby, J. D. (1957). The determination of the elastic field of an ellipsoidal inclusion, and related problems. *Proceedings of the Royal Society of London. Series A. Mathematical and Physical Sciences*, 241(1226):376–396. (Cited on pages 15, 34, and 97.)

Farquharson, C. G. and Oldenburg, D. W. (2004). A comparison of automatic techniques for estimating the regularization parameter in non-linear inverse problems. *Geophysical Journal International*, 156(3):411–425. (Cited on pages 57 and 58.)

Gassmann, F. (1951). Elastic waves through a packing of spheres. *Geophysics*, 16(4):673–685. Publisher: Society of Exploration Geophysicists. (Cited on pages 9 and 16.)

Gibson, R. L. and Ben-Menahem, A. (1991). Elastic wave scattering by anisotropic obstacles: application to fractured volumes. *Journal of Geophysical Research: Solid Earth*, 96(B12):19905–19924. (Cited on page 2.)

Grechka, V. (2005). Penny-shaped fractures revisited. *Stud. Geophys. Geod.*, page 17. (Cited on page 12.)

Gubbins, D. (2004). *Time series analysis and inverse theory for geophysicists*. Cambridge University Press. (Cited on pages 48 and 49.)

Gubernatis, J. E., Domany, E., and Krumhansl, J. A. (1977). Formal aspects of the theory of the scattering of ultrasound by flaws in elastic materials. *Journal of Applied Physics*, 48(7):2804–2811. (Cited on page 29.)

Guéguen, Y. and Palciauskas, V. (1994). *Introduction to the Physics of Rocks*. Princeton University Press. (Cited on pages 7, 8, 9, 10, 11, 12, 13, 16, 19, and 94.)

Hadamard, J. (1952). *Lectures on Cauchy's problem in linear partial differential equations*. Dover Publications, New York. (Cited on page 48.)

Hansen, P. C. (1994). REGULARIZATION TOOLS: A Matlab package for analysis and solution of discrete ill-posed problems. *Numerical Algorithms*, 6(1):1–35. (Cited on page 48.)

Hansen, P. C. (2001). The L-curve and its use in the numerical treatment of inverse problems. In *Computational Inverse Problems in Electrocardiology*, page 24. WIT Press. (Cited on page 57.)

Hesford, A. J. and Chew, W. C. (2010). Fast inverse scattering solutions using the distorted Born iterative method and the multilevel fast multipole algorithm. *The Journal of the Acoustical Society of America*, 128(2):679–690. (Cited on pages 50 and 57.)

Hornby, B. E., Schwartz, L. M., and Hudson, J. A. (1994). Anisotropic effective-medium modeling of the elastic properties of shales. *Geophysics*, 59(10):1570–1583. (Cited on page 11.)

Huang, X., Eikrem, K. S., Nævdal, G., and Jakobsen, M. (2020a). Bayesian Full Waveform Inversion In Anisotropic Elastic Media Using The Iterated Extended Kalman Filter. *Geophysics*. in press. (Cited on pages 11, 38, 50, 51, 93, and 94.)

Huang, X., Jakobsen, M., Naevdal, G., and Eikrem, K. (2020b). Target-oriented inversion of time-lapse seismic waveform data. *Communications in Computational Physics*, 28(1):249–275. (Cited on pages 2 and 28.)

Hudson, J. A. (1980). Overall properties of a cracked solid. *Mathematical Proceedings of the Cambridge Philosophical Society*, 88(2):371–384. (Cited on pages 12, 13, 19, and 73.)

Hudson, J. A. (1981). Wave speeds and attenuation of elastic waves in material containing cracks. *Geophysical Journal International*, 64(1):133–150. (Cited on pages 12, 13, and 15.)

Hudson, J. A. and Heritage, J. R. (1981). The use of the Born approximation in seismic scattering problems. *Geophysical Journal International*, 66(1):221–240. (Cited on page 28.)

Ikelle, L. and Amundsen, L. (2005). Introduction to petroleum seismology: Society of Exploration Geophysicists. *Tulsa, Oklahoma*. (Cited on pages ix, 1, 9, 10, 24, 27, 28, and 37.)

Jakobsen, M. (2004). The interacting inclusion model of wave-induced fluid flow: Inclusion model of wave-induced fluid flow. *Geophysical Journal International*, 158(3):1168–1176. (Cited on page 15.)

Jakobsen, M. (2006). The effective permeability of fractured reservoirs and composite porous media. In *SEG Technical Program Expanded Abstracts 2006*, pages 1747–1751. Society of Exploration Geophysicists. (Cited on page 94.)

Jakobsen, M. (2012). T-matrix approach to seismic forward modelling in the acoustic approximation. *Studia Geophysica et Geodaetica*, 56(1):1–20. (Cited on pages 28, 29, and 37.)

Jakobsen, M., Huang, X., and Wu, R.-S. (2020a). Homotopy analysis of the Lippmann-Schwinger equation for seismic wavefield modeling in strongly scattering media. *Geophysical Journal International*, 222(2):743–753. (Cited on pages 28, 29, 93, and 94.)

Jakobsen, M. and Hudson, J. A. (2003). Visco-Elastic Waves in Rock-Like Composites. *Stud. Geophys. Geod.*, page 34. (Cited on pages 16 and 32.)

Jakobsen, M., Hudson, J. A., and Johansen, T. A. (2003a). T-matrix approach to shale acoustics. *Geophysical Journal International*, 154(2):533–558. (Cited on pages 1, 9, 11, 12, 13, 14, 15, 19, 20, 32, 33, 73, 74, and 93.)

Jakobsen, M. and Johansen, T. A. (2000). Anisotropic approximations for mudrocks: A seismic laboratory study. *GEOPHYSICS*, 65(6):1711–1725. (Cited on page 9.)

Jakobsen, M. and Johansen, T. A. (2005). The effects of drained and undrained loading on visco-elastic waves in rock-like composites. *International Journal of Solids and Structures*, 42(5-6):1597–1611. (Cited on pages 15, 97, and 98.)

Jakobsen, M., Johansen, T. A., and McCann, C. (2003b). The acoustic signature of fluid flow in complex porous media. *Journal of Applied Geophysics*, 54(3-4):219–246. (Cited on pages 11, 14, 16, and 75.)

Jakobsen, M. and Pilskog, I. (2016). Gassmann-consistent Born Inversion for Fracture Density. In *78th EAGE Conference and Exhibition 2016.* (Cited on pages 4, 16, 21, 30, and 94.)

Jakobsen, M., Psencík, I., Iversen, E., and Ursin, B. (2020b). Transition Operator Approach to Seismic Full-Waveform Inversion in Arbitrary Anisotropic Elastic Media. *Commun. Comput. Phys.*, 28(1):297–327. (Cited on pages 1, 2, 3, 8, 10, 11, 28, 29, 30, 31, 32, 33, 34, 36, 37, 38, 39, 49, 50, 51, 52, 53, 54, 55, 56, 57, 58, 59, 60, 74, 76, 93, 99, 100, and 102.)

Jakobsen, M., Pšencık, I., Iversen, E., and Ursin, B. (2017). On the parametrization of seismic anisotropy for ray-Born inversion. *Seismic waves in Complex 3-D Structures*, 27:37–49. (Cited on pages 3, 4, 11, 51, 62, 91, and 92.)

Jakobsen, M. and Tveit, S. (2018). Distorted Born iterative T-matrix method for inversion of CSEM data in anisotropic media. *Geophysical Journal International*, 214(3):1524–1537. (Cited on page 57.)

Jakobsen, M. and Ursin, B. (2015). Full waveform inversion in the frequency domain using direct iterative T-matrix methods. *Journal of Geophysics and Engineering*, 12(3):400–418. (Cited on pages 3, 24, 28, 29, 34, 35, 38, 39, 48, 49, 50, 53, 55, and 57.)

Jakobsen, M. and Wu, R.-S. (2018). Accelerating the T-matrix approach to seismic full-waveform inversion by domain decomposition: Domain decomposition method for T-matrix-based FWI. *Geophysical Prospecting*, 66(6):1039–1059. (Cited on pages 2, 3, 28, 29, 50, 55, and 57.)

Jakobsen, M., Wu, R.-S., and Huang, X. (2020c). Convergent scattering series solution of the inhomogeneous Helmholtz equation via renormalization group and homotopy continuation approaches. *Journal of Computational Physics*, 409. (Cited on pages 28, 29, 93, and 94.)

Jin, Z., Chapman, M., and Papageorgiou, G. (2018). Frequency-dependent anisotropy in a partially saturated fractured rock. *Geophysical Journal International*, 215(3):1985–1998. (Cited on pages 17 and 94.)

Kamath, N. and Tsvankin, I. (2014). Sensitivity analysis for elastic full-waveform inversion in VTI media. In *SEG Technical Program Expanded Abstracts 2014*, pages 1162–1166, Denver, Colorado. Society of Exploration Geophysicists. (Cited on page 3.)

Kamath, N. and Tsvankin, I. (2016). Elastic full-waveform inversion for VTI media: Methodology and sensitivity analysis. *GEOPHYSICS*, 81(2):C53–C68. (Cited on pages 10, 62, 68, 91, and 92.)

Kelly, K., Ward, R., Treitel, S., and Alford, R. (1976). Synthetic seismograms: A finite-difference approach. *Geophysics*, 41(1):2–27. (Cited on page 27.)

Kirchner, A. and Shapiro, S. A. (2001). Fast repeat-modelling of time-lapse seismograms. *Geophysical Prospecting*, 49(5):557–569. (Cited on page 33.)

Kranz, R. L. (1983). Microcracks in rocks: A review. *Tectonophysics*, 100(1-3):449–480. (Cited on page 11.)

Krebes, E. (2004). Seismic forward modeling. *CSEG Recorder*, 30:28–39. (Cited on pages 27, 28, and 74.)

Kuster, G. T. and Toksöz, M. N. (1974). Velocity and attenuation of seismic waves in two-phase media: Part I. Theoretical formulations. *Geophysics*, 39(5):587–606. (Cited on page 12.)

Lavarello, R. and Oelze, M. (2009). Tomographic Reconstruction of Three-Dimensional Volumes Using the Distorted Born Iterative Method. *IEEE Transactions on Medical Imaging*, 28(10):1643–1653. (Cited on page 58.)

Lee, H.-Y., Koo, J. M., Min, D.-J., Kwon, B.-D., and Yoo, H. S. (2010). Frequency-domain elastic full waveform inversion for VTI media: Elastic waveform inversion for VTI media. *Geophysical Journal International*, 183(2):884–904. (Cited on pages 1, 10, 62, and 68.)

Lee, V.-G. (2009). Derivatives of the three-dimensional Green's functions for anisotropic materials. *International Journal of Solids and Structures*, 46(18-19):3471–3479. (Cited on page 34.)

Madariaga, R. (2007). 4.02 Seismic Source Theory. In *Seismic Source Theory*, volume 4. Elsevier. (Cited on pages 2, 29, 32, 99, 100, and 101.)

Malovichko, M., Khokhlov, N., Yavich, N., and Zhdanov, M. (2017). Approximate solutions of acoustic 3D integral equation and their application to seismic modeling and full-waveform inversion. *Journal of Computational Physics*, 346:318–339. (Cited on page 28.)

Mavko, G., Mukerji, T., and Dvorkin, J. (2009). *The rock physics handbook: Tools for seismic analysis of porous media*. Cambridge university press. (Cited on pages 12, 13, 17, 19, 94, 97, and 98.)

Menke, W. (2012). *Geophysical data analysis : discrete inverse theory*. Elsevier/AP, Amsterdam, 3rd edition. (Cited on pages 27, 48, and 55.)

Mensch, T. and Rasolofosaon, P. (1997). Elastic-wave velocities in anisotropic media of arbitrary symmetry—generalization of Thomsen's parameters. *Geophysical Journal International*, 128(1):43–64. Publisher: Blackwell Publishing Ltd Oxford, UK. (Cited on page 11.)

Nishizawa, O. (1982). Seismic velocity anisotropy in a medium containing oriented cracks. *Journal of Physics of the Earth*, 30(4):331–347. (Cited on page 13.)

Osnabrugge, G., Leedumrongwatthanakun, S., and Vellekoop, I. M. (2016). A convergent Born series for solving the inhomogeneous Helmholtz equation in arbitrarily large media. *Journal of Computational Physics*, 322:113–124. (Cited on pages 28, 29, and 93.)

Ozmen, N. (2014). *Ultrasound Imaging Methods for Breast Cancer Detection*. PhD thesis, Technische Universiteit Delft, Delft. (Cited on page 37.)

Ozmen, N., Dapp, R., Zapf, M., Gemmeke, H., Ruiter, N. V., and van Dongen, K. W. A. (2015). Comparing different ultrasound imaging methods for breast cancer detection. *IEEE Transactions on Ultrasonics, Ferroelectrics, and Frequency Control*, 62(4):637–646. (Cited on page 37.)

Pan, W., Innanen, K. A., and Liao, W. (2017). Accelerating Hessian-free Gauss-Newton full-waveform inversion via l-BFGS preconditioned conjugate-gradient algorithm. *GEOPHYSICS*, 82(2):R49–R64. (Cited on page 55.)

Pilskog, I., López, M., and Jakobsen, M. (2015). T-matrix FWI for Fracture Parameters. (Cited on pages 1, 3, 4, 13, 14, 15, 16, 24, 73, 74, 75, and 92.)

Ponte Castañeda, P. and Willis, J. (1995). The effect of spatial distribution on the effective behavior of composite materials and cracked media. *Journal of the Mechanics and Physics of Solids*, 43(12):1919–1951. (Cited on page 15.)

Pratt, G., Shin, C., and Hicks, G. (1998). Gauss-Newton and full Newton methods in frequency-space seismic waveform inversion. *Geophysical Journal International*, 133(2):341–362. (Cited on pages 49 and 55.)

Pratt, R. G. (1999). Seismic waveform inversion in the frequency domain, Part 1: Theory and verification in a physical scale model. *Geophysics*, 64(3):888–901. (Cited on pages 3, 47, 56, and 92.)

Pujol, J. (2003). *Elastic wave propagation and generation in seismology*. Cambridge University Press. (Cited on page 33.)

Richter, M. (2016). *Inverse problems: Basics, theory and applications in geophysics*. Birkhäuser. (Cited on page 49.)

Ricker, N. (1953). THE FORM AND LAWS OF PROPAGATION OF SEISMIC WAVELETS. *GEOPHYSICS*, 18(1):10–40. (Cited on page 37.)

Royer, D. and Dieulesaint, E. (1999). *Elastic waves in solids I: Free and guided propagation*. Springer Science & Business Media. (Cited on page 2.)

Saad, Y. (2003). *Iterative methods for sparse linear systems*, volume 82. siam. (Cited on page 37.)

Saad, Y. and Schultz, M. H. (1986). GMRES: A generalized minimal residual algorithm for solving nonsymmetric linear systems. *SIAM Journal on scientific and statistical computing*, 7(3):856–869. Publisher: SIAM. (Cited on page 37.)

Sayers, C. M. (1994). P-wave propagation in weakly anisotropic media. *Geophysical Journal International*, 116(3):799–805. Publisher: Blackwell Publishing Ltd Oxford, UK. (Cited on page 9.)

Sayers, C. M. (2009). Seismic characterization of reservoirs containing multiple fracture sets. *Geophysical Prospecting*, 57(2):187–192. (Cited on pages 9, 11, 13, 14, 73, 93, and 94.)

Schleicher, J., Tygel, M., Ursin, B., and Bleistein, N. (2001). The Kirchhoff–Helmholtz integral for anisotropic elastic media. *Wave Motion*, 34(4):353–364. (Cited on page 29.)

Schoenberg, M. (1980). Elastic wave behavior across linear slip interfaces. *The Journal of the Acoustical Society of America*, 68(5):1516–1521. (Cited on page 93.)

Schoenberg, M. and Douma, J. (1988). Elastic wave propagation in media with parallel fractures and aligned cracks. *Geophysical Prospecting*, 36(6):571–590. (Cited on pages 12, 13, and 73.)

Schoenberg, M. and Sayers, C. M. (1995). Seismic anisotropy of fractured rock. *Geophysics*, 60(1):204–211. (Cited on pages 9 and 94.)

Schuster, G. T. (2017). *Seismic inversion*. Society of Exploration Geophysicists. (Not cited.)

Shahraini, A., Ali, A., and Jakobsen, M. (2011). Characterization of fractured reservoirs using a consistent stiffness-permeability model: focus on the effects of fracture aperture: Characterization of fractured reservoirs. *Geophysical Prospecting*, 59(3):492–505. (Cited on pages ix, 12, 14, 16, and 94.)

Snieder, R. (2002). General Theory of Elastic Wave Scattering. In *Scattering*, pages 528–542. Elsevier. (Cited on pages 2, 7, 8, 27, 28, 29, 30, 31, 33, and 99.)

Strassen, V. (1969). Gaussian elimination is not optimal. *Numerische mathematik*, 13(4):354–356. (Cited on page 37.)

Sævik, P. N., Berre, I., Jakobsen, M., and Lien, M. (2013). A 3D Computational Study of Effective Medium Methods Applied to Fractured Media. *Transport in Porous Media*, 100(1):115–142. (Cited on pages 1 and 11.)

Tarantola, A. (2005). *Inverse Problem Theory and Methods for Model Parameter Estimation*. Society for Industrial and Applied Mathematics. (Cited on pages 5, 48, and 49.)

Thomsen, L. (1986). Weak elastic anisotropy. *Geophysics*, 51(10):1954–1966. (Cited on pages 9 and 11.)

Torquato, S. and Haslach Jr, H. (2002). Random heterogeneous materials: microstructure and macroscopic properties. *Appl. Mech. Rev.*, 55(4):B62–B63. (Cited on page 97.)

Tsvankin, I. (2012). *Seismic signatures and analysis of reflection data in anisotropic media*. Society of Exploration Geophysicists. (Cited on pages 62, 68, and 91.)

Ursin, B. and Tygel, M. (1997). Reciprocal volume and surface scattering integrals for anisotropic elastic media. *Wave Motion*, 26(1):31–42. (Cited on page 28.)

Van der Vorst, H. A. (1992). Bi-CGSTAB: A fast and smoothly converging variant of Bi-CG for the solution of nonsymmetric linear systems. *SIAM Journal on scientific and Statistical Computing*, 13(2):631–644. Publisher: SIAM. (Cited on page 37.)

Virieux, J. and Operto, S. (2009). An overview of full-waveform inversion in exploration geophysics. *GEOPHYSICS*, 74(6):WCC1–WCC26. (Cited on pages 3 and 55.)

Wang, Y. (2015). The Ricker wavelet and the Lambert W function. *Geophysical Journal International*, 200(1):111–115. (Cited on page 37.)

Weglein, A. B., Araújo, F. V., Carvalho, P. M., Stolt, R. H., Matson, K. H., Coates, R. T., Corrigan, D., Foster, D. J., Shaw, S. A., and Zhang, H. (2003). Inverse scattering series and seismic exploration. *Inverse Problems*, 19(6):R27–R83. (Cited on pages 2 and 50.)

Wood, A. (1955). *A Textbook of Sound: Being an Account of the Physics of Vibrations with Special Reference to Recent Theoretical and Technical Developments*. G. Bell. (Cited on page 17.)

Zhang, Z., Alkhalifah, T., Oh, J.-W., and Tsvankin, I. (2017). Estimation of fracture parameters using elastic full-waveform inversion. In *SEG Technical Program Expanded Abstracts 2017*, pages 3272–3276, Houston, Texas. Society of Exploration Geophysicists. (Cited on pages 1, 3, 9, 40, and 93.)

Zhang, Z.-D. and Alkhalifah, T. (2019). Regularized elastic full-waveform inversion using deep learning. *GEOPHYSICS*, 84(5):R741–R751. (Cited on page 11.)

Zhdanov, M. S. (2015). *Inverse theory and applications in geophysics*, volume 36. Elsevier, 2nd edition. (Cited on pages 47, 48, 49, and 55.)

Červený, V. (2005). *Seismic ray theory*. Cambridge university press. (Cited on pages 4, 28, 29, 30, 31, 33, and 99.)

Červený, V. and Coppoli, A. (1992). Ray born synthetic seismograms for complex structures containing scatterers. *Journal of seismic exploration*, 1:191–206. (Cited on page 28.)